Performance analysis of conventional and next-generation artificial geodetic radar reflectors

K. Patel

Technische Universiteit Delft

TU Delft Delft University of Technology

Challenge the future

Performance analysis of conventional and next-generation artificial geodetic radar reflectors

by

K. Patel

in partial fulfillment of the requirements for the degree of

Master of Science
in Applied Earth Sciences

at the Delft University of Technology,
to be defended publicly on (Tuesday, November 3, 2020 at 13:00.)

Supervisor:	Prof. dr. ir. R.F. (Ramon) Hanssen	
Thesis committee:	Dr. ir. F. J. (Freek) van Leijen,	TU Delft
	Dr. ir. H. (Hans) van der Marel,	TU Delft
	Prof. ir. P. (Peter) Hoogeboom,	TU Delft

An electronic version of this thesis is available at http://repository.tudelft.nl/.

Delft University of Technology

Preface

For an MSc. student, a master thesis holds tremendous significance as it marks the transition from the classes to professional environment; from learning the theory to its applications; from committing to external structures of works to designing their own structures and deadlines; from learning the lessons presented to them to learning to draw out their own lessons. This requires a commitment to a project that challenges them to add value, to try out different ways of working and perhaps more importantly - making mistakes and learning from them.

I was fortunate to find such an opportunity through an advanced research field like InSAR, where I carried out this project as a part of my master thesis under the guidance of Prof.dr.ir. R.F. (Ramon) Hanssen, Dr.ir. F.J. (Freek) van Leijen and Dr.ir. H. (Hans) van der Marel.

I would like to take the opportunity to thank Prof.dr.ir. R.F. (Ramon) Hanssen for introducing me to the topic and for taking the time and effort to guide me through the challenges. Working under him for the past few months was a valuable experience. I would also like to thank Dr.ir. F.J. (Freek) van Leijen and Dr.ir. H. (Hans) van der Marel for their constant supervision, for their valuable feedback but most of all for their unwavering patience which gave me a valuable opportunity to learn from my mistakes. Their comments were crucial in compiling this report. I hope this project adds value in some way to the ongoing efforts of space geodesy at TU Delft.

I would also like to thank Dr.ir. H. (Hans) van der Marel for access to his scenic backyard to act as the site for experiments. I would like to thank all the members of the radar research group who selflessly provided help in the installation of the corner reflectors on that rainy afternoon.

This report describes the work carried out a part of the TU Delft's contribution in the framework of WP3300 of the ESRIN contract "Multiple Frequency Radar Compact Transponder (MUTE)", between the European Space Agency and the main contractor Space Engineering, Rome, Italy (No.40001090040/13/I-IW). The consortium additionally included Airbus, TRE Altimira, Progressive Systems with Space Engineering leading the consortium and TU Delft offering the site-maintenance and processing support. I would like to thank the community involved in such efforts that make these studies possible. We acknowledge the use of imagery from the ESA and AIRBUS for Sentinel-1 and TerraSAR-X respectively.

I am deeply grateful to the student community at the GRS faculty of TU Delft, Snellius student board, my friends here in Delft and in the office 1.33.1 for the company they have provided during my stay in the Netherlands. I am also lucky to have had a pleasure of working with people at KNMI, in particular Bas Mijling, Ronald van der A and Tim Vlemmix. I wish to express my appreciation for their constant support and help. I also wish to thank my friends with whom I have lived for the past year: Theodore, Martin and Anita for their encouragement and the indispensable company provided by Olivia and Vinesh at the Royal library in Den Haag. In particular, I would like to thank Anita, to whom I dedicate this thesis, for the discussions we have had that sparked much needed inspiration from time to time.

To the reader, I hope you find this report to be clear and to your satisfaction.

K. Patel
Delft, June 2020

List of abbreviations

DEM - Digital Elevation Model

RCS - Radar Cross Section

PSI - Persistent Scatterer Interferometry

PS - Persistent Scatterers

DS - Distributed Scatterers

PSC - Persistent Scatterer Candidates

PSP - Potential Persistent Scatterer

AR - Artificial Reflectors

RT - Radar Transponders

CR - Corner Reflectos

NAP - Normaal Amsterdams Peil

DBF - Double-backflip corner reflectors

ECR - Electronic Corner Reflectors

MLE - Maximum Likelihood Estimation

IGRS - Integrated Geodetic Reference Station

Summary

Recent advances in interferometric synthetic aperture radar have increased the scope of its applications to areas that were beyond its purview of investigation due to decorrelation effects. The development of Persistent Scatterer Interferometry allows interferometric analysis over select coherent points identified in a stack of SAR images which can be utilized to determine deformation characteristics (along with the estimation of atmospheric signal delay and topographic height) over generally decorrelated areas. Subsequent use of corner reflectors allowed the introduction of coherent scatterers to areas where they do not occur naturally (such as vegetation-covered landscapes) and provides a measure of control over a network of such PS points. However, the use of these reflectors is beset with the following challenges: one set up for ascending and descending tracks, collection of debris in its apex, bulky size, unknown phase errors introduced by settlement under self-weight, etc. Based on the experiment carried out with several reflector devices at Wassenaar, The Netherlands, here we show that specific next-generation artificial reflectors can address some of the challenges posed by conventional corner reflectors while allowing the integration of measurements from several deformation monitoring techniques.

As part of the experiment, an actual 7 ± 0.05 mm vertical movement imparted deliberately to radar transponder MUTE-1 is estimated within 0.01 to 0.69 mm deviation while the actual line of sight motion and radar cross section change realized as a result of imparting deliberate tilt to DBFm device is estimated from SAR results within 0.47 mm and 1.7 dBm^2 respectively. This **demonstrates the ability to capture motions from SAR images by deploying these devices** resulting from either a natural geodetic cause or due to deliberate changes carried out for application-specific purposes.

The vertical displacement results for MUTE-2 radar transponders (obtained relative to conventional corner reflectors) are validated using a ground survey campaign within one standard deviation error bounds; for the MUTE-1 device, this agreement is obtained after model-adjustment. This demonstrates that it is possible to use radar transponders of second-generation type (i.e. MUTE-2) to act as reliable PS points for InSAR applications. Displacement results in the horizontal direction (East-West projection) from InSAR are in agreement with those recorded from the ground survey within error bounds which suggests that the location WASS01 housing devices MUTE-1 and DBFT, tilts in the western directions (estimates of maximum tilt vary from 0.9 to 1.95 mm) while WASS02 location on which MUTE-2 is installed exhibits an eastward tilt (about 2 mm in magnitude). **Tilt motions observed at two distinct locations** demonstrates that they are not caused by changing water levels in nearby canal (location WASS02 is over 50 m away from water canal) but **results from the susceptibility of concrete foundation design to swelling and shrinkage of soil**.

By analyzing meteorological data in conjunction with SAR results from installed devices, we find that certain heavy snow and significant rainfall events result in the accumulation of excess snow/water in the apex and on the reflection surfaces of the CRs, dampening the amplitude and corrupting the phase results. The **heavy snow events affect the amplitude and phase results of both conventional and double backflip CRs**, while the impact of heavy rain remains limited to the conventional reflector type. This suggests that **the downward-pointing design of DBF CRs drains the water preventing its accumulation in the apex**. The susceptibility of DBF devices to snow is not surprising since some amount of snow and debris is expected to stick to its reflection surface and affect the results.

Prototypes of two different families show a lack of stability in their amplitude and phase response. A significant trend and step in the response due to either device malfunction or temperature sensitivity of the sensor renders the time series of first-generation MUTE (MUTE-1) unstable while lack of stability in double backflip mockup (DBFm) is attributed to its lack of structural stiffness. Comparative stability analysis demonstrates that **next generation reflector devices (MUTE-2, DBFT and DBFX) can be utilized to determine motions in the vertical and horizontal direction and detect changes**

in orientation of the device over a vegetation area with low backscattering characteristics **with sub-millimeter precision**.

We anticipate this study to be a small step towards a more sophisticated ground segment for SAR satellites consisting of reflectors that can adequately provide knowledge about deformation characteristics of the area under investigation. Advancement in radar transponder technology can potentially increase the informational value of SAR products by encoding ancillary non-radar data into the reflected signal, essentially turning each reflector into an autonomous monitoring station, using solar panels as its power source. The possibility of collocating InSAR observations with GNSS measurements using Integrated Geodetic Reference Station or Radar Transponders Autonomous Stations means that deformation can be obtained in an absolute sense for a terrestrial reference frame. Establishing a worldwide network of such stations would mean that absolute deformation can potentially be monitored on a global scale.

Contents

1
Introduction

1.1. Background

The history of determining deformation is closely intertwined with the history of determining the position of points, their relative distances and angles. The origin of land surveying techniques can be traced back to the idea of land measurements among agricultural communities of ancient civilizations and construction of ancient monuments [1]. The advancement of this field has been marked by the advances in the tools and subsequent techniques used to determine these position, their relative distances and angles. The period of Early Renaissance led to the introduction of the plane table, Gunter's chain and theodolite, commencing the era of modern surveying. These devices were eventually replaced with a new generation of devices (such as - laser level, Electronic Distance Measurement (EDM) equipment or total station etc.) that emerged with the advancements in electronics, improving the accuracy and speed of measurements.

Today, the conventional method of determining geodetic ground deformation involves measurements carried out with these devices. The portability of these devices allows survey measurements over a network of predetermined points. Series of measurements over such points are performed in a single campaign. Depending on the time period of interest and network design, additional campaigns are carried out to record evolution of these measurements with time. Measurement time series thus obtained over such a network is used to estimate the deformation parameters and their precision. The determination of deformation for monitoring applications is limited in space – providing deformation values for the local area under investigation for the campaign, and in time – only deformation between the campaign periods can be determined. The approach also depends on a-priori knowledge and is practically constrained by the physical nature of benchmarks [2].

Advancements in satellites technology has had tremendous impact on remote sensing applications by vastly increasing the spatial scope of observations. The technique of airborne radar interferometry started emerging in the 1980s, producing the first interferograms. Initially these studies were aimed at topopgraphy estimation [3] and by early 1990s, studies by [4, 5] were able to demonstrate the use of differential interferometry from satellite radar to estimate deformation fields of Landers earthquake.

These studies established the Interferometric Synthetic Aperture Radar (InSAR) as a viable geodetic technique. The basic principle of this technique involves determining the changes in the line of sight distances using radar images of earth obtained through satellites. Changes in line of sight distances between the surface and the imaging platform could be translated to deformations due to an uplift or subsidence of the ground with sub-centimetre accuracy [2]. The rise in InSAR techniques from satellite observations is able to address some of the challenges encountered by the conventional survey approaches to determine deformation. It increases the spatial scope of the area of observations that can be analysed and provides a randomly distributed set of benchmarks [2].

The initial techniques developed for InSAR were designed for contiguous observations – which relied on relatively strong coherence between the images [2]. Thus the initial approach was limited to areas that fit the conditions of the desired radar reflectance – desert landscapes and urban areas. This pushed the field of satellite geodesy towards increasing the scope of its applications to other kinds of land types, since many regions of the world that did not sufficiently fit the contiguous observation characteristics were not suitable for analysis with the initial InSAR approach.

The study by [6] was pivotal in establishing a modified approach – Persistent Scatterer Interferometry (PSI) which allowed deformation analysis of non-contiguous areas with satellite. This approach relied on identifying a set of persistent scatterers (PS) over a stack of multiple radar images that have a strong reflectance and are able to maintain their relatively strong coherence over time. Additionally, the contribution from topography, atmosphere and deformation is determined using the dependence of each these contributors in space and time. It involves analysis over set of PSs identified in the stack that resembles the network of optimal points of conventional geodetic approaches. However, unlike the conventional geodetic network, the number and locations of these PSs cannot be pre-determined before performing PSI analysis [2]. Thus this approach is said to be opportunistic. Over urban areas which show relatively strong coherence, typically a large number of PS points are identified and thus the need for optimization of location of such points becomes secondary [2].

While the number and locations of the existing PSs over a region cannot be determined beforehand, it is possible to deliberately introduce such points in the areas to be imaged. Using the characteristics of the radar, corner reflectors (abbreviated henceforth as CR) have been designed that reflect the incoming radar pulse towards the receiver and maintains its coherence over time. By placing such CRs beforehand over an area to be imaged it is possible to exert control over the network of points subsequently analyzed by effectively controlling the number and locations of such CRs [7]. These reflectors can also be placed over areas that have no naturally occurring PS as can be the case over areas covered with vegetation.

Such deformation monitoring by introduction of artificial reflectors (ARs) has been carried out with some success. These studies are expanded in more detail in Chapter 2. The physical nature of CR introduces some challenges in its use for deformation monitoring applications such as large size constraints, potential settlement under self-weight, collection of excess rain or snow despite perforations provided for drainage and one setup per ascending or descending pass (see Section 2.6). The InSAR observations are affected by the aforementioned events. Therefore, errors introduced by, e.g. settlement under self-weight of a corner reflector, manifests itself in the measurements as a(n) (unknown) phase error.

The contemporary satellite deformation monitoring field has seen emergence of new types of AR devices that have the potential to increase the value of recorded SAR products in addition to addressing some of the challenges posed by conventional CRs (see Section 2.7). However, the main argument in support for their use is the opportunity to seamlessly collocate the reference points from multiple deformation monitoring techniques. By facilitating this simple step, these devices enable determination of absolute deformation (in terrestrial reference frame with global datum) from relative deformation measurements by datum connection. Study by [7] describes this datum connection procedure and the feasibility of collocating radar transponders (RT) and GPS antenna is demonstrated by a test case in IJmuiden. The structural design of the newly developed double backflip (DBF) CRs [8, 9] has provisions for installing GNSS antenna unobtrusively with CR reflection surfaces. Besides GPS, these new generation devices can incorporate reference points for levelling, total station, LiDAR, gravimetry and laser altimetry. The possibility of integrating data from multiple measurement techniques makes the DBF type of CR device a potential Integrated Geodetic Reference Station (IGRS). Integrating data from diverse measurement techniques that observe with varying spatial scale, frequency and geometry can provide additional information about ground movement that can assist a more accurate interpretation of the results. Like conventional CRs, each of the other reflector types have their own advantages and disadvantages. This study focuses on the comparison of performance of conventional CRs, new generation DBF CRs and two types of RTs called electronic corner reflector (ECR) and MUTE RT to test their stability for deformation monitering applications. The following section sets this aim of the study in the form of research questions that will be investigated in the upcoming chapters.

1.2. Research questions

This study is aimed towards measurement and comparison of reflectors and their ability to perform as PSs. A comparison of performance between CRs and RTs is provided in this study, and possible factors affecting their performance are investigated in more detail.

The main research question of this study is:

How can the environmental and instrumental factors that affect the performance of radar transponders and double backflip corner reflectors as artificial point scatterers be quantified?

Atmospheric conditions (through accumulation of excess rainwater/snow) affect the performance of a corner reflector as a PS. It is expected that radar transponders are also prone to atmospheric conditions, but in a different way. Due to the electronics involved, a dependency on temperature may play a role.

This question is further subdivided into the following sub-research questions which are answered in subsequent chapters of this thesis.

1. How can the response of installed PS devices be defined and estimated from the satellite images?
   (a) Which methods can be used to extract signal and clutter radar cross section (RCS) from satellite images?
   (b) How do the different methods perform in estimating reflectance response?
   (c) Do the different devices at the test site show stability in its RCS and phase response?
2. How do the results from ground survey compare with those from InSAR across different platforms?
   (a) Are the ”artificial” deformations that are introduced deliberately, detected in the result? What is the error associated with this value?
   (b) Is there an agreement between displacements observed from satellite techniques and ground level surveys carried out at the test site?
3. What is the relation between the RCS and phase errors and different factors that influence the device response?
   (a) What is the influence of meteorological factors, device malfunctioning and temperature on the RCS and phase results of PS points?
   (b) How do the phase variances obtained from RCS compare with those obtained from measurements?

1.3. Thesis outline

The research questions proposed in the previous section about the performance characteristics of different types of ARs are investigated on the basis of the experiment carried out at the Wassenaar test site. Findings regarding the nature of AR devices is attained using measurements from this site by extracting relevant parameters from SAR observations, validating these observations with ground truth and considering the influence of external factors on the performance parameters of AR devices. The following chapters in this report follow this line of inquiry.

Chapter 2 traces the evolution of techniques that provides context for the devices used in the current experiment that form the central focus of this thesis. It begins with a description of typical spaceborne RADAR system. Next the technique of interferometry developed for such system is introduced in the context of ground deformation application. Discussion of the limitations of this technique is provided along with the subsequent emergence of PSI technique as a response to those limitations. This is followed by a section on CRs to gain control over geodetic network of points. The current challenges posed by the nature of CRs are presented along with the potential of new alternative ARs such as RTs and DBF CRs in addressing those concerns. Finally, a brief review of some of the studies that have been carried out prior to this experiments are provided.

The exact setup and the conditions of the experiment are covered in the first half of Chapter 3. The site location is briefly described followed by the setup of the experiments carried out at this site. The installation procedure of different types of ARs employed in the current experiment is provided in chronological order along with their timeline of operation. The latter half of this Chapter describes the ground survey campaign carried out during the course of the experiment. These measurements comprises the ground truth against which the InSAR results are validated.

The performance assessment of different ARs is carried out for amplitude and phase results in Chapter 4 and Chapter 5 respectively.

The assessment of amplitude response in Chapter 4 is carried out in terms of RCS. The importance of this parameter along with its definition is stated first followed by a methodology section that explains the different approaches employed to extract signal and clutter parameters from stack of SAR images. Signal observed from multiple approaches is then tested against the theoretical RCS levels to select an approach to be used for further analysis. The influence of external factors on the RCS signal performance is presented by taking into account meteorological factors, influence of temperature, device malfunction and deliberate tilt imparted to the device DBFm. The stability of RCS response of different devices is then quantified and compared against each other. Finally, using a representative signal and clutter value for each PS point, an a-priori phase variance is approximated.

The assessment of phase response in Chapter 5 is carried out for vertical double-differences expressed in millimeters. These vertical double-differences for device pair containing device MUTE-1 are utilized to test the InSAR estimate of movement imparted to this device deliberately against the motion determined from ground truth. The overall deformation signal measured from InSAR is compared against the signal determined from ground survey campaign to validate the phase results from all MUTE RTs on the site. The effect of external factors on the phase response is considered by taking into account the influence of temperature, device malfunction and deliberate tilt in DBFm. The phase stability of different ARs are compared against each other where the influence of meteorological factors on the performance of CRs is demonstrated. Finally, the precision of InSAR measurements is compared against the a-priori approximation derived from representative signal and clutter estimate to determine if precision can be approximated with a good accuracy using the adopted approach of extracting signal and clutter in this study.

Chapter 6 covers the conclusions drawn from the results provided in this report by answering the research questions proposed in this study. Findings regarding the assessment of amplitude and phase behavior of different ARs, their comparisons with ground survey results and the influence of external factors is provided. This is followed by some recommendations for future studies in the field.

Supplementary details are provided as three separate appendices. Appendix A explains the geometry of DBF CRs, the alignment strategy adopted for all CRs on the site and the misalignments in the orientation of these devices. Updated data from ground survey campaign is also reported in this chapter which are used to generate the results presented in Chapter 3 and which aid the interpretation of phase results in Chapter 5. Appendix B briefly describes the simulation carried out to determine the expectation values of Rician distributed signal and clutter. Appendix C provides a total overview of all the devices employed at the test site. A list of references is provided at the end mentioning in order the studies citied in this report.

2

Interferometry for deformation applications

Efforts to address standing challenges in application of satellite interferometry has led to an evolution in techniques which subsequently has increased the opportunity to carry out deformation studies over areas which could not be studied previously due to heavy decorrelation. The analysis provided in this study is aimed at aiding this same effort - comparing the performance of AR devices and testing their suitability for their use in satellite interferometry so as to increase the scope of InSAR applications. This chapter gives an overview of satellite interferometry techniques in order to provide context for reflector devices used in the experiments carried out for this study. While InSAR technique can be utilized for a diverse set of applications, this chapter is written with ground deformation application in mind. Furthermore, a few cases using AR devices to monitor deformation are reviewed along with examples of recent studies performed using RT devices. The following paragraph points out the order in which this description is provided.

The first half of this chapter provides an introduction to the basic concepts of satellite interferometry. First, the basic principles of obtaining SAR images are explained in Section 2.1. The following Section 2.2 and Section 2.3 provide an overview of the processing techniques to exploit information of value from such images. Section 2.4 discusses the subsequent development of PSI technique. The second half of the chapter than elaborates on the use of the satellite interferometry techniques for their application in deformation monitoring. Section 2.5 introduces artificial reflectors and describes their role in interferometry with corner reflectors (Section 2.6) and the emergence of the new generation artificial reflectors called radar transponders (Section 2.7). The final Section 2.8 of the chapter reviews some of the key experiments that have been carried out with these artificial reflectors.

2.1. SAR

A typical radar system, used for remote sensing applications, transmits a radar pulse to the target and receives its reflection in order to determine the properties of the target, such as its range, size, surface roughness etc. An imaging radar generates a two dimensional image of the reflected back scatter. Real Aperture Radars (RAR) are imaging radars mounted on air-borne moving platforms facing the ground with a side-looking geometry. The range resolution of such a radar depends on the length of the transmitted pulse while the azimuth resolution is antenna size dependent.

A Synthetic Aperture Radar (SAR) utilizes the movement of the platform over the target region to increase the aperture of the antenna by combining radar echoes from multiple positions using signal processing techniques. Figure 2.1 from [10] illustrates the basic geometry of a typical SAR acquisition from a side looking radar platform of dimensions $L_a \times D_a$ moving with the velocity v_{sc} at height H_{sat} above the surface. The footprint of a single pulse is represented by the shaded region. As a SAR moves over a ground area, it illuminates the target with multiple pluses. By the time the responses from these pulse are received the platform has moved along the track to a new position. Using signal processing techniques, these ordered radar echoes can be combined to generate a synthetic antenna aperture. Using this principle, synthetic apertures larger than the actual physical antenna size can be devised allowing the system to generate high resolution radar imagery.

Records of these responses are stored digitally, along with annotation files containing the travel time records of these pulses. Using "focusing" techniques these acquisitions are integrated to reconstruct scatterers response from a larger synthetic antenna. Several algorithm have been developed for focusing such as chirp compression [11], range-doppler [12], seismic migration [13] etc. The study by [14] provides a comparison of different focusing algorithms. Using such signal processing techniques, SAR images with improved resolution are obtained over a large spatial scale (100 by 100 km^2).

Each pixel of the image, marked by a specific range (across track) and azimuth (along track) coordinate corresponds to a specific area over the ground. Each pixel contains information about the amplitude and phase in the form of a complex phasor. A typical phasor y from such an image - also referred to as "Single look complex" (SLC) image, can be expressed as

$$y = |a|\exp(j\psi), \tag{2.1}$$

where j is the imaginary number, $|a|$ represents the amplitude of the pixel obtained as absolute value of the complex number, and ψ is the observed phase.

The amplitude response is related to RCS which represents the relationship between the transmitted and received radar signals. In the following passage, a formal description of RCS as defined in [15, 16] is provided. As mentioned above SAR is an active radar system that operates by transmitting and receiving radar signals. The relation between the transmitted and received signal for polarimetric radar can be expressed as

$$\begin{pmatrix} E_h^s \\ E_v^s \end{pmatrix} = \frac{e^{jk_oR}}{R} \begin{pmatrix} S_{hh} & S_{vh} \\ S_{hv} & S_{vv} \end{pmatrix} \begin{pmatrix} E_h^i \\ E_v^i \end{pmatrix}, \tag{2.2}$$

where E refers to the electric field vectors for incident waves (represented with superscript i) and scattered waves (superscript s), S represents the elements of scattering matrix which provides a measure of reflectivity of the target in different horizontal and vertical polarizations, k_o is the wavenumber and R refers to the distance between the radar sensor and the target.

The RCS(σ_{pq}) is then defined as

$$\sigma_{pq} = 4\pi |E^i S E^s|^2, \tag{2.3}$$

where S is the scattering matrix expressed in Equation (2.2) and E^i and E^s refer to transmitted and received polarized electric fields. Since the SAR radar systems typically have linear polarization, the following RCS expression for linear polarization is more relevant

$$\sigma_{pq} = 4\pi |S_{E^i E^s}|^2. \tag{2.4}$$

The phase obtained from a single SLC SAR image is influenced by the range between the platform and the target, the atmospheric properties during the imaging epoch introducing delays, the summation of scattering characteristics of elements in the resolution area and additional noise. Thus the observed phase can be represented as a combination of these constituents

$$\psi = \mathrm{W}(\psi_{\text{range}} + \psi_{\text{atmos}} + \psi_{\text{scat}} + \psi_{\text{noise}}), \tag{2.5}$$

where W is the wrapping operator and the subscripts describe the corresponding constituents of observed phase ψ.

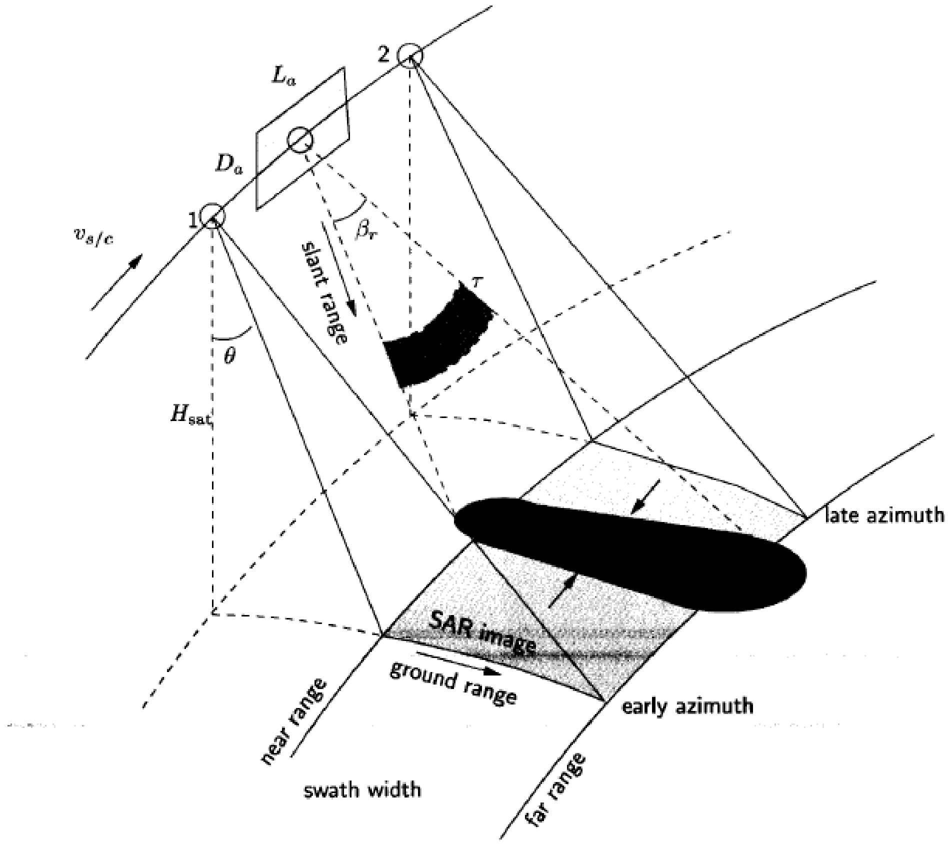

Figure 2.1: Illustration of SAR acquisition geometry from a space based platform travelling at a velocity v_{sc}. The shaded region represents the portion of ground illuminated by a radar pulse. The image extends from near range to far range in across track directions and early azimuth to late azimuth in the along track direction. [Source:[10]]

Phase from a single SAR image depends on these factors which makes it arbitrary. To obtain information of interest such as topography or deformation requires generation of interference pattern using another SAR image. The next section describes how this interference pattern is generated and how components of differential phase are isolated to extract valuable information.

2.2. InSAR

The technique of InSAR is based on the principle of interference between two SAR images. The pattern of interference is generated between two images acquired over a common area at different moments in time. This interference is carried out by complex conjugate multiplication of the two aligned SAR images resulting in a complex image known as an "interferogram". An interferogram provides the phase difference between the two original SAR images which can be utilized to extract information about position or rate of change in position of the target.

If y_1 and y_2 represent the phasors of two aligned SAR images (as expressed in Equation (2.1)), then the interferogram obtained from complex multiplication can be expressed as [10]

$$I_{12} = y_1 y_2^* = |a_1||a_2|\exp(j(\psi_1 - \psi_2)), \tag{2.6}$$

where I_{12} is the interferogram obtained as a product between the SAR master image denoted by y_1 and the complex conjugate of the slave image y_2 (with $.^*$ denoting the complex conjugate). Such an interferogram is said to have been generated by "multiplicative interferometry" where the amplitudes of the SAR master image ($|a_1|$) and slave image ($|a_2|$) are multiplied, while the phase of the master (ψ_1) and slave (ψ_2) are subtracted to give the phase difference or interferometric phase. This phase difference ($\Delta\phi$), similar to Equation (2.5), can also be expressed into its constituents as

$$\Delta\phi_{12} = \mathrm{W}(\psi_1 - \psi_2) = \mathrm{W}(\phi_{\text{range}} + \phi_{\text{atmos}} + \phi_{\text{scat}} + \phi_{\text{noise}}). \tag{2.7}$$

The range component of the interferometric phase (ϕ_{range}) corresponds to the change in phase introduced due to the change in the range line of sight (LOS) distance between the sensor and the target. The aim of this technique is to use this relationship between differential phase and the range component to determine topography or deformation. The range component of the phase difference can be expressed as a combination of flat earth phase (ϕ_{flat}), topography (ϕ_{topo}) and deformation (ϕ_{defo}) phase components, as expressed by the following equation [10, 17, 18]

$$\phi_{\text{range}} = \phi_{\text{flat}} + \phi_{\text{topo}} + \phi_{\text{defo}} = \frac{4\pi}{\lambda}\left(B\sin(\theta - \alpha) - \frac{B_\perp}{R\sin(\theta_{\text{inc}})}H - D_{\text{LOS}}\right), \tag{2.8}$$

here B refers to the interferometric baseline, $B_\perp$ refers to the perpendicular component of the baseline, λ refers to the wavelength of the radar pulse, H is the height of topography relative to the reference surface, D_{LOS} refers to the 3D displacement of the target projected on the radar LOS direction, θ is the look angle, α is the baseline orientation angle and θ_{inc} denotes the incidence angle.

The flat earth phase is the phase contribution from a reference surface (e.g. an ellipsoid). It depends on the difference in the positions of the two SAR acquisitions. This effect is present even in the absence of topography [5] and introduces a trend in the interferogram [17]. Based on far-field approximation (i.e. assuming parallel travel paths for the two acquisitions) [5] the flat earth contribution can be calculated (first term in the right hand side of Equation (2.8)) and removed from the interferogram given satellite orbits and reference ellipsoid parameters. The removal of this contribution - called "flattening" of interferogram - leads to the range component that depends on the contribution due to topography and deformation relative to the reference ellipsoid.

For deformation studies, the topographic component needs to be removed in addition to the removal of flat earth component. The topographic component from the flattened interferogram can be removed either using a Digital Elevation Model (DEM) or another interferogram obtained using short baseline. These corrections result in an interferogram that contains information about the deformation between the acquisition epochs along with residual errors arising from imperfections in the corrections applied. These errors are introduced due to the imperfections in DEM or topographic maps obtained from short temporal baseline interferogram (resulting in ”residual topographic phase” in the corrected interferogram) and due to the errors in the orbit information (resulting in residual component ϕ_{orbit} in the corrected interferogram).

The contribution from the atmosphere (ϕ_{atmos}) introduces a delay in phase difference. This contribution is a combination of effects from turbulent mixing and vertical stratification in the troposphere and changes in free electron density in the ionosphere. For a more detailed description the reader is referred to [10, 19–21].

The scattering component of the phase difference (ϕ_{scat}) relates to the change in scattering properties of the surface between the satellite passes. These changes in scattering properties can be due to the changes in the physical or electrical properties of the surface. The signal obtained from a single pixel of a SAR image relates to the superimposed response from the individual elements within the resolution area on the ground. Thus the scattering component of phase (ψ_{scat}) from each SLC image depends on the distribution and physical properties of these elements. Depending upon the nature of the target, these properties can be dynamic and may change with time rapidly. For instance, particular type of vegetation may grow significantly within a few days or an urban landscape might change due to human activities. Since the satellite acquisition times vary from days to months (depending upon the sensor), these physical changes in the surface will contribute to the change in phase from these acquisitions (ϕ_{scat}).

The noise component of the phase difference (ϕ_{noise}) is caused by the noise introduced either as system noise, processing noise or combination of both. A more detailed description of these phase components can be found in [18].

To isolate the range component from the observed phase difference requires that the contribution from all other components is minimal. Thus, in order to detect deformation of the scattering ground surface, the conditions should be such that the dominant change in phase corresponds to the change in position of the surface and not due to change in the properties of the surface or due to the change in the image geometry of acquisitions. The atmospheric signal can be ignored in case of an adequately large deformation signal. In order to prevent the loss of coherence due to the change in scattering properties – also called “temporal decorrelation” - only the regions of the surface with high coherence values are used for InSAR analysis. To prevent the loss of coherence due to image geometry acquisition – or “geometric decorrelation” - spectral filtering has to be performed which relies on detecting frequency shifts in the reflectivity spectrum [22]. Various algorithms have been developed to generate interferograms and carry out these operations to extract deformation. The following section describes some common steps involved in a typical InSAR processing algorithm.

2.3. InSAR processing chain

The generation of interferograms involves several steps, in order to carry out alignment adjustments, corrections and filtering. This section gives a brief overview of the key steps required in a typical InSAR processing chain as elaborated in [18].

2.3.1. Coregistration and Resampling

The SLC master and slave images need to be aligned with each other, so that the pixels of overlapping images correspond to the same resolution area of the surface. A single offset between the master and slave image is computed based on the precise orbit information for satellite tracks during the acquisitions. This is referred to as the “coarse orbit coregistration” step. The “fine coregistration” step is then carried out by computing the range and azimuth offset of each pixel using cross correlation of amplitudes of the SLC images. After the computation of these shifts the slave image is then interpolated to the pixel positions of the master image in the “resampling” step. A more detailed explanation of this step can be found in [23–25].

2.3.2. Oversampling

The interferogram is generated as a complex conjugate product of the master and slave SLC images. Such a product in the time domain is equivalent to a convolution in the frequency domain. Such convolution results in the doubling of the original spectra in the resulting interferogram. Since the sampling frequency of the interferogram is same as that of the original SLC images, aliasing effects are introduced [10]. This effect can be prevented by oversampling the master and slave SLC images by zero padding their spectra in the frequency domain to double the number of samples. Study by [26] demonstrates improvements due to oversampling applied to the spectra from the European Remote Sensing (ERS) sensor and discusses this topic more detail.

2.3.3. Flat earth and topography

After the generation of interferogram, the unwanted contribution to the phase that can be determined are removed from it. This includes the contribution from the reference surface (flat earth phase) that is approximated and subtracted from each pixel using its reference location. The location of each pixel is determined using geocoding procedure. [27] provides a mathematical framework for geocoding that is based on least-squares adjustment involving interferometric phase, range, Doppler centroid frequency and flight path. For deformation analysis, the topographic phase is also removed from the interferogram using either a DEM or a topographic map generated using a short temporal baseline interferogram. See [28] for more details.

2.3.4. Spectral filtering

As mentioned before, spectral filtering is carried out to reduce the effects of geometric decorrelation. Imaging the ground from two different incidence and squint angles will result in a frequency shift of the spectra of the master and slave images in the range and azimuth direction respectively. This shift in range is calculated using the expression [22]

$$f_\phi = \frac{2B_\perp}{\lambda R_m \tan(\theta^m_{\text{inc}} - \alpha)}, \tag{2.9}$$

where $B_\perp$ refers to the perpendicular component of the baseline, λ is the wavelength of the radar pulse, R_m refers to the range between the platform and the target, α represents the terrain slope and θ^m_{inc} refers to the incidence angle of the master acquisition. The calculation of this shift can be used to remove the non-overlapping part of the range spectra that is caused due to the shift. The shift in the azimuth spectra is calculated in a similar fashion using the squint angle to remove the non-overlapping part of the azimuth spectra. The study by [29] dicusses the spectral filtering in range and azimuth in more detail, while [26] provides this discussion specifically for the ERS mission.

2.3.5. Complex multilook

"Multilook" step involves spatial averaging of the signal to reduce the noise. This averaging is performed over adjacent pixels that show a constant signal component. As shown in [10, 18] the multilooked interferogram for a pixel k can be calculated as

$$< I_k >= \frac{1}{L}\sum_{i=1}^{L} M_i S_i^*, \tag{2.10}$$

where L refers to the multilook factor, i refers to the index of the adjacent pixels used for averaging, M and S refer to the master and slave image respectively. The study by [30] goes into more detail about the process of complex multilooking.

2.3.6. Phase Unwrapping

The phase differences of the interferogram are wrapped. The process to obtain absolute phase differences from the wrapped phase differences is known as "unwrapping". For the InSAR technique it is commonly assumed that the difference between the phase of two adjacent pixels is less than half the wave cycle. This assumption holds except for conditions when the spatial gradient of the signal components are very strong, such as in a mountain landscape with sudden changes in topographic slope, or large deformations close to the fault line of an earthquake. The reader is referred to [31] for more comprehensive overview.

2.3.7. Limitations

As mentioned before, using InSAR for deformation analysis requires isolating phase difference component for deformation from other components. To prevent the temporal decorrelation, only surfaces with high coherence value are usually utilized for InSAR analysis. This constraint leaves out large parts of the world where the land-type does not exhibit high radar coherence characteristics. Similarly, to prevent geometric decorrelation, the interferograms obtained from large perpendicular baselines cannot be used for analysis, limiting the choice of the input acquisitions to those whose baselines fall under the critical value. These factors constrain the opportunity for carrying out InSAR analysis over a region of interest. Additionally, for cases where small deformation signals are expected, it becomes difficult to identify and separate the atmospheric signal from the deformation signal using this technique. Efforts made to address these limitations has led to the development of modified InSAR techniques. The most prominent among them is the PSI method.

2.4. Persistent Scatterer Interferometry

In light of the limitations mentioned in the previous section, a modified approach developed by [6] increases the scope of the application of satellite interferometry to areas that, as a whole, do not show high coherence characteristics.

This technique called PSI, utilizes specific PS pixels of differential interferograms that are generated from a stack of SAR images with a common master, to obtain deformation time-series. The classification of a pixel as a PS is based on the following definitions of persistent and distributed scatterers.

A pixel of a SAR image spans over multiple scattering entities within its resolution cell. The response recorded for this pixel represents the superposition of responses from all the elements associated with that pixel. If the resolution cell happens to contain a strong point scatterer, the signal from this element dominates in the pixel while the other elements contribute additional noise called clutter. Such pixels exhibit point scatterer type behavior and are known as Persistent Scatterer pixels (PS pixels or sometimes referred directly as PS). Strong persistent reflection from the dominant point scatterer ensures the stability of the signal recorded in the interferograms with large temporal and spatial baselines. The PSI technique relies on the presence of features that show such strong and stable scattering behavior for long time periods over the region of interest. Coherent information available from pixels associated with these features allow formation of geodetic network over which deformation analysis can be carried out in an otherwise noisy interferograms.

In absence of a dominant point scatterer in a resolution cell, the response recorded in the pixel can be decorrelated. Such pixels are known as Distributed Scatterer pixels (DS pixels or DS). Figure 2.2 shows the phasors associated with typical PS and DS pixels. Figure 2.2a illustrates the presence of a strong scatterer that leads to a large phasor vector with clutter from the remaining elements represented by Gaussian circular distribution. Figure 2.2c shows this phasor for a DS pixel with only clutter in absence of a strong scatterer. While, it is possible that selective interferograms formed with pairs of SAR images with small temporal and perpendicular baseline have DS pixels that contain coherent information (study by [18] goes into more detail about how such coherent information can be exploited for analysis) this section focuses on PSI techniques based on the analysis of the PS pixels alone. Using a network of PS pixels, deformation time-series is estimated for each PS. Along with deformation time-series, this technique also provides estimates of topographic height and atmospheric signal delay time series. For this, the technique relies on the nature of the temporal and spatial dependencies (and decorrelations) of these effects in a stack of interferograms.

Since the advent of PSI by [6] several alternative algorithms have been developed [17, 32]. The following section expands on some of the key steps involved in a typical PSI processing chain applied to a stack of differential interferograms referenced to a common master image.

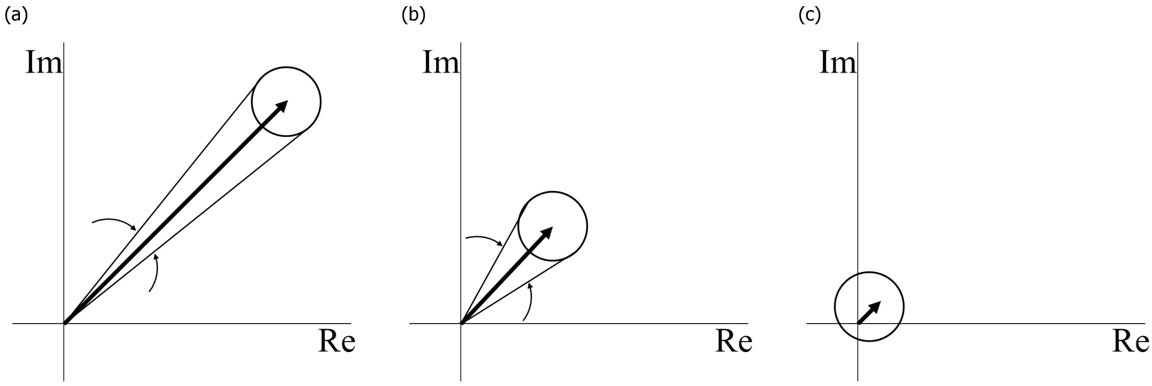

Figure 2.2: Illustration of a phasor in a complex plane, with the vector denoting the amplitude of the signal from PS in a resolution area with the slope angle denoting the phase. The circle represents the clutter which is assumed to have a Gaussian Circular distribution. The angle formed by the tangents of the circle passing through the origin (marked here with arrows) denotes the phase variance. (a) Phasor in a complex plane for a typical PS pixel with a strong point scatterer. (b) Phasor for a PS pixel for a scatterer with weaker backscatter characteristics relative to (a). (c) Phasor for a DS pixel in absence of any strong scatterer in the resolution cell. This figure illustrates that phasors with large amplitudes have a smaller phase variance. [Source: [10]]

2.4.1. PSI Processing Steps

This section gives a brief overview about the typical PSI processing methodology which involves selection of PS pixels, formation of geodetic network, parameter estimation and removal of atmospheric signal.

The first step of the analysis involves selection of "persistent scatterer candidates" (PSCs) and "potential persistent scatterers" (PSPs). The selection of the final PSs will be from these sets of points that are initially shortlisted by the "amplitude dispersion index" denoted by D_A. The first selection of potential PS points is based on the idea of using temporal stability of amplitude as a proxy for the temporal stability of phase. The dispersion amplitude index is a measure of this temporal stability of amplitude and can be expressed as [6]

$$D_A = \frac{\sigma_A}{\mu_A} \approx \hat{\sigma}_\phi, \tag{2.11}$$

where σ_A refers to the standard deviation of the amplitude and μ_A is the average amplitude computed over the time range of the stack.

Figure 2.2 from [10] shows a phasor in a complex plane, with the vector denoting the amplitude of the signal from PSs of different sizes in a resolution area with the slope angle denoting the phase. The circle denotes the circular distribution of the clutter within the resolution area. Thus, it can be observed that assuming a Gaussian circular distribution of the clutter, a larger amplitude leads to a lower phase variance. This assumption for clutter holds for homogeneous vegetation fields, forests and deserts [18]. The use of amplitude dispersion as a proxy for the phase variance is limited to low standard deviation cases where $\sigma_\phi < 0.25$ radians. This is illustrated in Figure 2.3 which shows a scatter plot of the simulated relation between the dispersion index and phase along with the linear relationship between them. The simulation is generated by keeping the signal fixed at 1 and varying the noise using standard deviations between 0 and 0.8. This model is simulated for 3000 points in a stack of 50 SAR images for a complex variable expressed as a combination of signal with noise. This figure shows that low values of amplitude dispersion can be used as an estimate of phase variance.

Thus, using thresholds on the dispersion index (D_A), initial selection of the PSC and PSP are made. PSPs are used to densify the network and are therefore selected using a less strict threshold.

The selected PSCs are used to form a geodetic network which allows computation of deformation as double-difference time series. This refers to the observation of deformation obtained as a differ-

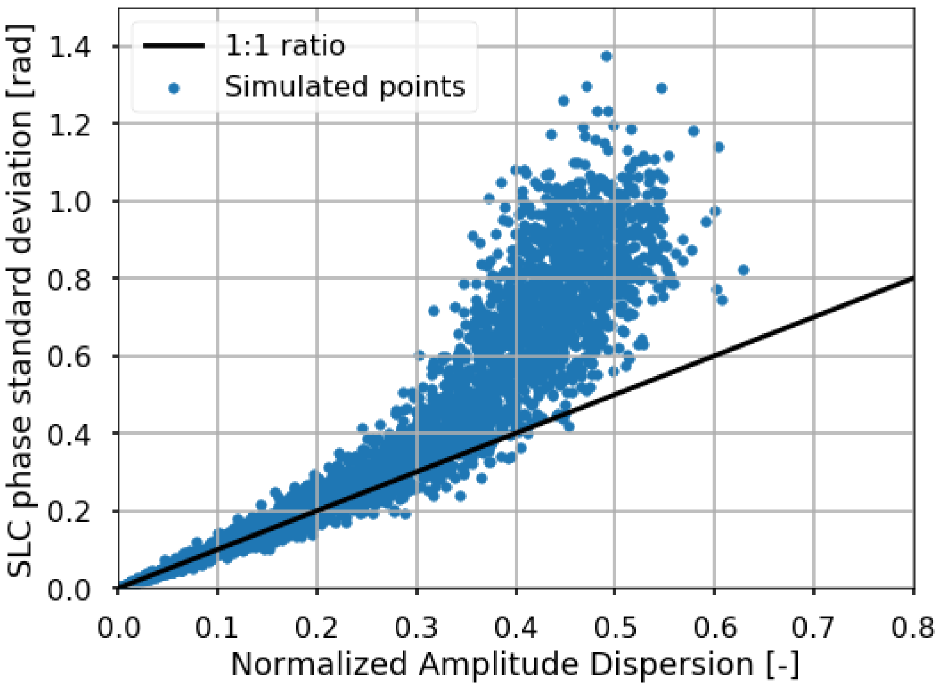

Figure 2.3: Relation between the amplitude dispersion and the phase standard deviation. This result is based on the simulation carried out in [6, 18]. The simulation of a complex variable ($z = s + n$) as a combination of a signal (of magnitude 1) with varying noise is carried out 3000 times for 50 SAR image stack. The standard deviation of noise is varied from 0 to 0.8. The black line represents the linear relationship between them while the blue markers represents the simulated relationship. The figure illustrates that this linear relationship agrees well for lower values of amplitude dispersion.

ence carried out temporally (difference between the two acquisition times) and spatially (difference between two points or PS pixels in this case) [33]. The construction of a network can be carried out by constructing a triangulated irregular network based on Delaunay triangulation which relies on the principle of maximizing the minimum angle of the triangles formed by the connecting arcs of the PSCs in the network [34]. A freely connected geodetic network can also be constructed using PS points as demonstrated by [35]. The redundant design of the network ensures that parameter testing can be performed.

The parameter estimation step involves estimation of parameters such as topography, deformation and integer ambiguity. The aim of this step is filter out the different components of the observed phase differences by devising a functional model. Integer ambiguity can be a parameter to be estimated in the functional model or separate algorithms can be implemented for this purpose – LAMBDA or bootstrapping method.

The development of a functional model to estimate the rate of deformation requires a-priori knowledge of the nature of deformation in space and time. In case this knowledge is not available, the region is assumed to have a linear deformation mechanism [36]. If the actual deformation does not follow this linear mechanism then its deviation from this linear behaviour will come up in the residuals. The relationship between the deformation component of the phase difference and the actual deformation modelled linearly can be expressed as

$$\phi_{\text{defo}} = -\frac{4\pi}{\lambda} D_{\text{LOS}} = -\frac{4\pi}{\lambda} T \cdot \Delta_D, \tag{2.12}$$

where T is the temporal baseline from the master acquisition and Δ_D denotes the rate of displacements.

As mentioned before in Equation (2.8), the relationship between the topographic phase difference (ϕ_{topo}) and the topography height (H) can be expressed using the far-field approximation as [3, 10, 18]

$$\phi_{\text{topo}} = \frac{-4\pi}{\lambda} \frac{B_{\perp}}{R\sin(\theta_{\text{inc}})} H, \tag{2.13}$$

where the notations are identical to one mentioned in Section 2.2.

For the functional model this relationship is expressed in the following form which is equivalent in the relationship but is expressed with different notations

$$\phi_{\text{topo}} = \beta \Delta_H, \tag{2.14}$$

where β is equivalent to the first half of the Equation (2.13) and denotes the height to phase conversion factor while Δ_H is equivalent to H and represents the topographic height. Thus using relationships expressed in Equation (2.12), Equation (2.13) and Equation (2.14) the following model is devised for parameter estimation

$$\phi = \beta \Delta_H - \frac{4\pi}{\lambda} T \cdot \Delta_D + \phi_{\text{error}} + 2k\pi, \tag{2.15}$$

where $2k\pi$ represents the functional model for estimating integer ambiguity, ϕ_{error} represents the residuals, ϕ represents the observed phase differences at the PSC locations and topographic height (Δ_H), deformation (Δ_D) are the parameters of interest to be estimated. Note that the atmospheric and noise components are not included in the model but will be estimated and removed separately from the residuals.

Thus the parameter estimation of deformation, topography and integer ambiguity is carried out over each arc. A new selection of PS is carried out of the available PSCs in three steps.

The selection steps involve removal of PSCs based on the deviation of time series from the specified functional model [6, 18] which is measured by its precision. Ensemble coherence ($\hat{\gamma}_{\text{ens}}$), used as an index for performing this selection can be expressed as

$$\hat{\gamma}_{\text{ens}} = \frac{1}{K} \left| \sum_{k=1}^{K} \exp(j \cdot \phi_{\text{error}}) \right|, \tag{2.16}$$

where K represents the total number of interferograms, j is the imaginary number, ϕ_{error} is the residual obtained as a difference between the observed and the model phase. Thus using a threshold on $\hat{\gamma}_{\text{ens}}$, some PSCs can be rejected.

In the second selection step, all the PSCs which are not connected to at least 3 arcs are rejected. The final step involves rejection of PSCs that fit the network.

The filtering step involves determination and removal of the atmospheric signal. This involves assumptions about the spatio-temporal characteristics for the effects of atmosphere and un-modelled deformation. A high pass filter is passed through the residual in the time domain. The atmosphere is assumed to be correlated in space but not in time. Vice-versa, un-modelled deformations are assumed to be un-correlated in space but correlated in time. This results in a residual phase time series for each point at the PSC locations containing atmospheric signal and orbital errors. From this, an atmospheric phase screen (APS) is created for each epoch, using Kriging interpolation which acts as a low pass filter in space [18]. Thus a stack of APS images are obtained for each epoch, as the atmospheric signal is intended to be removed from both the PSCs and PSPs.

These APS images are subtracted from the interferograms and the steps for the formation of the network and the estimation of the parameters are reiterated with PSCs and PSPs, now with atmospheric corrected signals. The set of PSPs whose two arcs fit the network of the PSCs are stored and the rest of the PSP points are rejected. Thus, deformation time series, topographic height and an atmospheric time series is obtained from a single reference point. Variance component estimation can be employed to estimate its precision.

2.5. Interferometry with artificial PS

As shown in the preceding sections, InSAR is a technique which utilizes the difference in phase between two or more SAR images over a common area at different times. Such differences in phase can be utilized to generate digital elevation models (DEMs) and/or to determine the movements within the domain mapped by the image [37].

Using differential phase from InSAR (also referred to as DInSAR) deformation maps over an area spanning hundreds of kilometres can be generated. Meaningful analysis can be carried out using this technique provided the region shows high coherence and the response characteristic does not change too much between acquisitions due change in physical properties. This approach has been utilized to monitor deformation resulting from earthquakes, volcanic activity, ice motions, underground extractions and mining [38].

From Section 2.3, Persistent Scatterer Interferometry (PSI) is a type of InSAR technique that utilizes multiple image datasets to identify specific scattering centres, called persistent scatterer (PS) that are stable and can be used as data points for analysis in a SAR image. The approach also involves correcting for atmospheric effects using atmospheric phase screen providing finer results than DInSAR [38].

This requires multiple SAR image dataset that contains sufficient number of PS. A PS point is characterized as a point in the area of interest that has a dominant response and shows stable phase behaviour over time. In an urban setting, there are several artificial structures with corners that are able to reflect a significant fraction of the incoming signal, providing the opportunity to be PS points. Thus, the technique of PSI provides a potential for monitor applications in urban areas [39, 40] and several studies around the world have demonstrated use of this technique over urban centers [38, 41–43].

In regions with no naturally occurring PS, they can be installed in the form of artificial reflectors (AR) that can provide the opportunity to carry out PSI analysis by acting as well known scattering centres, making them useful for validation purposes [33, 38, 39]. Usually, the location and occurrence of naturally occurring PS benchmarks cannot be regulated, which makes the approach opportunistic, making it difficult to ascertain beforehand whether the area of interest can be monitored. However, the installation of an AR provides a degree of control in terms of location of such points and increases PS density [44] facilitating validation studies with other geodetic observations [45].

The technique of PSI increases the scope of application of space interferometry, which was limited to the regions of high radar coherence, to the regions where only selective targets within the area show suitable coherence properties. The deployment of artificial reflectors further increases this opportunity to study areas that by itself do not have any dominant target for PSI analysis. It allows not only the introduction of PS to these sites but also provides an additional degree of control over their location.

2.6. Corner Reflectors

Corner reflectors (CR) are a type of artificial reflectors (AR) that employ the principle of internal reflection to generate a strong reflecting echo to the incoming signal from the satellite. A typical CR has two or three faces arranged orthogonally to each other and are made of conductive material like aluminium. Such an arrangement ensures that the signal is directed back to the direction of incidence.

CR can act as an essential PS point in a region with low naturally occurring PS or can complement already existing PS in the region. CRs have been used for validation of PSI by comparing them with levelling. A five-year study of CR time series showed that the measurement techniques levelling and PSI are in agreement within the error bounds [33]. Several studies have demonstrated the validation of CR as a reliable PS by carrying out "blind" experiments with the deliberate movement of CR [40, 46].

Such use of CRs for the purposes of deformation monitoring applications has been carried out by studies. From monitoring landslides in China [47], detecting small surface displacement in Germany [39], to gain insights into the deformation patterns of valley walls in Alberta [48].

The study [47] provides a case where conventional D-InSAR technique was used to obtain the topography of the Yangtze River Three Gorges dam area. Furthermore, 10 CRs were also deployed over the mountains in the vicinity, which are covered with heavy vegetation and heavily decorrelated, for monitoring Xintan landslide stability. Experiment in Bonn, Germany [39] deployed 19 CRs along a 20 km extent in across-track direction to monitor small surface displacements. A study carried out in Little Smoky River valley in Alberta, involved observing displacements in order to investigate deformation patterns of the valley walls which are not well understood [48]. The test site was characterized by heavy vegetation and the deformation patterns of the valley walls were expected to be complex (multiple recent slides superimposed on older more passive slides). The line of sight deformations were close to those measured by slope inclinometers that marked the horizontal component of deformation.

CRs have been the preferred type of AR being used for such studies as they are economic and conceptually simple. They do not require any kind of external power source, and being a non-electrical device they do not have any decay or drift in their response [44].

However, the design of CRs has requirements that put a lot of constraint on its design. The minimum dimension of a CR depends on the kind SAR sensor to be used for the study. C band sensors can require a CR with a side dimension of 1 m to 1.5 m depending on the mode of the sensor. This makes the reflector large and heavy. Size and weight can be a source of concern if the CR settles under its own weight and thus the deformation signal might not represent the true movement of the ground [44]. Even though the reflectors are provided with perforated holes, there have been cases where they get clogged [49] and affect the response behaviour. Disturbance by winds or debris [44] is also a point of concern and using them under precipitation and snow can prove to be a potential challenge [48, 49]. With one fixed setup, only one of the satellite passes either ascending or descending can be used for analysis [44]. In addition, not all design dimensions of a CR will behave in the same way in the SAR images of different sensors. In light of these concerns with CRs, radar transponders (RTs) have started to emerge as a possible viable alternative to corner reflectors.

2.7. Radar Transponders

A radar transponder (RT) is a device that receives a radar signal, amplifies it and retransmits it back to the source, with a constant phase delay of the signal. In principle, a RT is an amplifier placed between a receiver and a transmitter sealed under a small casing [50]. Such a device should preserve phase stability and coherence. It is an active device, which is pre-set to activate itself in a time window of satellite overpass.

2.7.1. Radar Transponders - Applications as a potential PS

RTs have already been used before for external calibration of SAR sensors [51]. The current versions of the devices are able to provide solutions to a lot of challenges posed by CRs. Being an electrical device the geometry of the object does not affect its response, which makes it a compact, lightweight device that works autonomously after its deployment [44, 52]. It is unaffected by dust or snow debris. Unlike a CR, the device can be designed to work for both ascending and descending pass over multiple sensors in a single setup.

However, these are electrical devices which require constant electrical power source near the region of interest. If power source near the region of interest is not available then lead batteries have been used, although for a long-term monitoring projects, battery life might prove to be inefficient [53].

They are thus also susceptible to electrical drift or decay and can introduce an error source due to temperature variation and ageing [44, 50]. The current cost of RT is higher than CR. On the practical side, a study might require permission or license from the government before using RT for radio transmissions as in [52].

Advances are being made on the hardware side to identify and address these issues. For instance, this study involves the use of RT devices that are being operated by a constant AC power supply in winter and use solar panels as a power source in summer.

More advancement on the electrical deviceation side can provide a lot of other advantages such as ancillary metadata and virtual deployment. The device can be designed to provide an additional ancillary data encoded into the reflected signal. This can allow each installed reflector to be local autonomous monitoring sensors that can record and transmit locally generated non-radar data that could be utilized for SAR imaging applications thus adding more informational value to the SAR image data stack [50]. Adjusting the internal delay of the device can provide the flexibility of virtually placing the device anywhere in the SAR track even when they are placed elsewhere physically. Such RT with an adjustable internal delay has been developed and tested where the devices were placed virtually over the lake [51].

Using artificial reflectors (both RTs and CRs) provide an opportunity to collocate InSAR with GNSS that can provide deformation estimates in absolute sense that allows for comparison of different regions imaged separately [9, 53].

Potential advantages provided by RTs over CRs build a strong case for investigating their viability as a potential PS. Advances in designing better ARs help alleviate the constraints of PSI studies by increasing the number of data points and increases the geographical scope of InSAR deformation monitoring applications. This study is an effort to test the current transponder device prototypes for their use in PSI analysis. The phase stability of these devices is tested under the current time period of study. Their response in SAR images is quantified to detect if there is a discrepancy or decay in their amplified response. Two different kinds of RT devices have been deployed in the study along with two types of corner reflectors. Performance analysis of these PSs is compared against each other under different satellite tracks.

2.8. Previous experiments

The culmination of the current study has been a continuum of the efforts carried out from TU Delft in this field. This section provides a short description of these studies to give a context for the current experiment. This description is based on the study carried out in [7]. These studies cover the extent of RT applications from detecting small displacements over grassland in Delft, landslide monitoring in Slovenia, establishing precision values in Wassenaar, carrying out datum connection approach in Ijmuiden. A separate study monitoring pipeline deformation in Italy using RT with PSI is also included [52].

2.8.1. Delft Validation Experiment

The setup of this experiment involved three RTs (T1, T2 and T3) and two CRs (C1 and C2) installed at a dairy farm in Delft. This location ensured low background clutter (from grass). Possible movements of the radar transponders and corner reflectors were assumed to be related to soil expansion and shrinkage only. The radar transponders were linked to the ERS-2 satellite which operated in zero-gyro mode. Levelling measurements were carried out between the devices (T1-C2, T2-C1 and T3-C1) and double-difference between deformation were calculated so that the relative deformation signal from InSAR can be compared to the relative deformation signal in levelling. These levelling height double-differences were converted to radar line of sight using the cosine of the radar incidence angle. These levelling double-differences had a precision of 2 mm. For the RT-CR InSAR double-difference, a precision of 6.7 mm was obtained, which improved to 3.9 mm after removal of two outliers. The double-differences from InSAR measurements showed a good agreement with the double-differences obtained from levelling.

The RT T1 and CR C2 were located close to each other and the similarities in T1-C1 double-difference and C2-C1 double-difference implied that the RT and CR (T1 and C2) behaved in identical manner for this PSI analysis.

2.8.2. Slovenia Deformation Experiment

This setup had three RTs along with a GPS receiver located at three points, two points were on one side of the Sava fault and the other point was on the opposite side of the fault. The site was in a heavily vegetated Alps region, known historically to be prone to landslides. The transponder was linked to the ENVISAT satellite's two tracks (t108 and t381), one of which (t381) unfortunately had a drifting baseline as the satellite was subject to change in orbit by a forced manoeuvre. This caused a change in the orbit number and thus two-time series were analysed. During InSAR analysis, the topographic phase was removed using a DEM. For track t108, the precision obtained for the double-difference was 4.9 mm which improved remarkably to 1.8 mm after removing 1 outlier. The precision obtained for track t381 was 4.6 mm. These results did not have any outliers.

These results established that RT can be used for monitoring events such as landslides. This study provides a practical case of deformation monitoring, as the landslide site selected is known to have historical debris flow, with potential for future slides presenting a risk to a village in the valley.

There are several error sources in both experiments that may have worsened the radar transponder precision estimate. The error sources include the orbit change of ENVISAT, the zero-gyro mode of ERS2, assumptions on atmospheric delay difference, the time between levelling measurements and transponder readings (during which soil can expand or shrink), snow over the GPS receiver etc.

2.8.3. Wassenaar Experiment - I

Using the insights into the error sources of the previous two experiments and the availability of the RADARSAT-2 satellite (no drifting baseline or zero-gyro mode), another experiment in Wassenaar was carried out. This experiment initially was to be performed with four radar transponders. However, due to unexpected problems with one of the radar transponder, it was removed and the experiment was carried out finally with three radar transponders (CAT1, CAT2, CAT3) over a farmland. To reduce the effect of swelling and shrinkage, the top layer of soil was removed and concrete pads were placed which acted as platforms of the radar transponders. A modern and more precise levelling device is used to perform the validation experiment such that the levelling precision was less than 0.1 mm. The double-difference transponder precision for track t102 was 0.8 mm and for track t202 was 1 mm.

This experiment was able to drastically improve the precision levels (to sub-millimetre levels for track t102) that were obtained for RT devices providing a much clearer insight into the performance capabilities of using such devices for PSI.

2.8.4. IJmuiden Experiment

This experiment was carried out to test InSAR's datum connection using GNSS that would provide the velocity of the reference point. Such an approach can provide deformation maps in absolute sense. To analyse the impact of local sea level rise, it important to compare its motion with absolute ground deformation. Thus, tide gauges prove to be an appropriate point of such a study given the context of its practical application in assessing sea level rise. Such a study was carried out at GPS stations in IJmuiden, Eijsden and Vlissingen which are also tide gauge stations. Three radar transponders were installed at these tide gauge stations with an intention of collocating them with permanent GNSS antenna. Due to logistical issues the RT at Eijsden was not connected directly to GNSS antenna but was rather installed on the roof of an adjacent building. Thus the deformation time series measured from

RT and GNSS antenna cannot be confirmed to be measuring identical signal and this site was not used for the experiment. The RT installed at Vlissingen on the other hand had issues with power supply. Only the transponder at the IJmuiden tide gauge was utilized for InSAR-GNSS datum connection.

PS deformation map is obtained relative to IJmuiden PS point. The GPS results from the collocated GNSS antenna is used to determine the motion of this reference point and connect the relative deformation maps from InSAR to a geodetic datum. This datum connection is performed to obtain absolute deformation map relative to the Normaal Amsterdams Peil (NAP) datum. Such absolute deformation maps relative to NAP could be compared to the tide gauge readings of sea levels which are also measured relative to NAP. The deformation results indicated subsidence which aligned with the expected soil compaction in the area.

Thus this experiment demonstrated the potential application of RT devices installed near tide gauges for flood monitoring and risk analysis against sea level rise.

2.8.5. Italian pipeline stability experiment

A similar study to one mentioned in Section 2.8.2 was carried out in Campomorone, Italy, using 7 prototype RT devices (also CAT devices manufactured by SEA in Bristol, UK which were used in Wassenaar Experiment - I and Slovenia Deformation Experiment) to measure ground and pipeline motion in the area. This study relied solely on the LOS movements of RTs and did not involve double-difference deformation or use of CRs. Three RT devices (referred to as CAT 1, 3 and 4) were anchored to the pipeline. One device was anchored to the ground and installed close to the pipeline (CAT 2) while the rest (CAT 5, 6, 7) were anchored to the ground in the vicinity of the pipeline. A "blind experiment" was performed where one of the devices (CAT 4) was subjected to a tilt and then brought back to horizontal. Both tilt and return tilt motion were captured (13.6 ±1.9 mm and -9.8 ±1.7 mm) in the SAR images that were analysed for Envisat track 387 which aligned with the expected LOS motion (between 13 and 16 mm). Return tilt activity was also captured by RADARSAT 1 interferogram which recorded a LOS movement of (-9.5 ±1.8 mm). The study was able to detect a higher rate of LOS motion in the central section of the slope. Similar to the study in Slovenia described in Section 2.8.2 this study was able to show that it was possible to use RT devices with PSI analysis to monitoring landslide events. This study spanned for a time period for less than a year and the authors stressed on using more number of SAR acquisitions. While GPS campaigns were carried out as an alternative geodetic technique to validate LOS motion for this study, their comparison with the InSAR results proved to be challenging.

The results from these initial experiments mark the use of these new generation RTs and test their capabilities for practical applications from obtaining absolute movements, checking the pipeline stability to landslide monitoring. The current study carried out in Wassenaar follows the experiments that are described in Section 2.8.1 to Section 2.8.4 and aims to provide a comparative analysis of performance behaviour of the different prototypes of RTs and CRs and how these behaviours are influenced by external factors. The following chapter describes the conditions of the experiment that has been carried out for this purpose.

3

Wassenaar Field Experiment

The first half of this chapter describes the setup and condition of the experiment. A brief description of Wassenaar location and its choice for the test site is provided in Section 3.1. The setup of devices employed in the present study evolved from the experiment that was carried out prior to this one at the same location. Section 3.2 describes the setup of this prior experiment - Wassenaar Experiment-I. Section 3.3 covers the setup of devices for the experiment covered in this study - Wassenaar Experiment-II. It introduces the different types of ARs, describing their installation and their timeline of operation whose analysis forms the main crux of the results in this report. The second half of this chapter describes the local surveys carried out to measure the stability of this network. Section 3.4 describes the ground survey campaign carried out throughout the course of this experiment and presents the results derived from the updated dataset reported in Appendix A. These ground survey measurements will be used to validate the InSAR measurements in subsequent chapters which answers the second research question proposed in Section 1.2.

3.1. Wassenaar Test Site

Wassenaar is a coastal municipality situated around 10 Km north of the city of The Hague in the Netherlands. The site is a private property farm and has been a grass field for several years. The landscape is flat, without any considerable slope or any natural outcrops that might show up as a PS except for those installed artificially. Except for soil shrinkage and expansion, the site is expected to show no major deformations, providing controlled conditions during the period of experimentation [7].

Wassenaar is considered to be a relatively dry patch between the North Sea to the west and marshes of Rhine delta towards the east. The subsoil consists mostly of barrier beach deposits which are overlaid with dune sands. Barrier beach refers to the raised bar-shaped sand beaches that form natural barriers between the dry land and wet marshes close to the sea. These deposits of dunes are usually aligned parallel to the coast - referred to as "Older dunes" (*"strandwal"* in Dutch) - which are separated by beach flats formed by an advancing coastline in the Subboreal period. The Wassenaar test site is situated on the second row of old dunes, next to a beach flat [54]. The old dunes at the test site had been excavated at the end of the 19th century and the field was until recently used for growing flower bulbs. The soil type is a mixture of clay and sand (*"geestgronden"* in Dutch, see [55]), without any significant peat or clay deposit in the subsurface. The water levels found in nearby canals are at 50 cm from the surface. The canals are a part of the dewatering system in the Netherlands and the levels are maintained to $1-2$ dm levels. The test site as a whole is subjected to tectonic movements but such motions do not influence the relative motion between the devices other than initially settling under self-weight.

3.2. Wassenaar Experiment - I

The test site has been operational for experiments since June 2013 and Figure 3.1a shows the initial arrangements of the devices for the experiment. The previous experiment employed RTs manufactured by SEA whose locations were marked as CAT4, CAT5, CAT6 and CAT7. On these locations, four concrete pads of dimension 2 m by 1.5 m by 0.15 m were installed (Figure 3.1b) on 23rd July 2013. The SEA RT were captured in satellite acquisitions from RADARSAT-2 descending track t102 and t202 from 8th August 2013 till 26th September 2015. The analysis of three RTs (one RT was rejected due to malfunction) within this setup is carried out in [7]. The response from RTs were also acquired from Sentinel-1A descending orbits of t037 and t110 from 19th December 2014 until 26th September 2015.

(a)

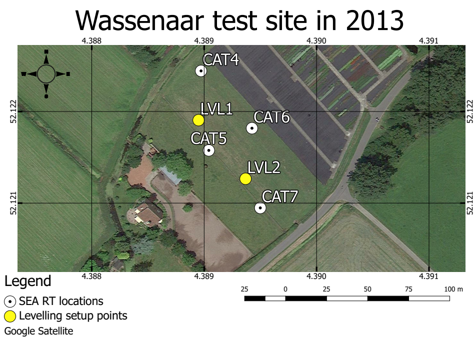

(b)

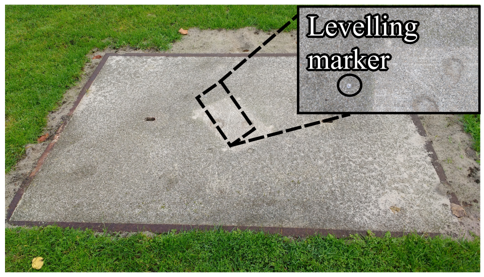

Figure 3.1: (a) Map of test site as seen in 2013, showing the locations of the SEA transponders at CAT4, CAT5, CAT6 and CAT7. LVL1 and LVL2 represent the location used to setup levelling device to measure height changes between the concrete pads. (b) Concrete foundation with an inset figure showing the levelling marker near the center of the pad.

The installation of the concrete pad involved removal of the top layer until the underlying undisturbed sand layer is exposed. This sand layer is then levelled by a laser system over which the pre-manufactured concrete pad is lowered and levelled. A levelling marker close to the center of the pad is placed to monitor its movement in subsequent survey campaigns carried out between 2013 and 2015. These campaigns involved measuring the height difference between the levelling markers. These measurements of height changes between the pads were smaller than 1 mm and could be attributed to the initial settling under self-weight during the first six months of the installation period. Thus, the practice of employing concrete paving pads along with the unique geographic characteristics of the test site provides a very stable platform for PS devices used for the experiments.

3.3. Wassenaar Experiment - II

In 2016 the Wassenaar test site was reconfigured for a new set of experiments. Reconfiguration was deemed necessary in order to accommodate more devices and to include acquisitions from both descending and ascending tracks. The locations and duration of the various PS devices along with their installations are described in a chronological order.

On 22nd September 2016, two concrete pads previously at locations CAT5 and CAT7 were removed and relocated to new positions WASS02 and WASS03. The locations CAT5 and CAT7 were not used from this point on as a platform for PSs. Additionally, two new concrete pads of dimension 2 m by 2 m by 0.15 m were installed at locations WASS01 and WASS04. The locations CAT4 and CAT6 were undisturbed but renamed to WASS06 and WASS05 to be consistent with the location naming convention for this experiment. Thus the network now consists of six concrete pads, four from the previous experiments of which two are relocated and two new pads of slightly larger dimensions. These positions were obtained as a result of minimizing the interference between responses from different systems and trying to maintain roughly equal distances to levelling setup points LVL1 and LVL2 so as to minimize the collimitation errors. Figure 3.2a shows the new device locations with the names of the devices that were installed since 2016.

On 26th September 2016, two MUTE RT were installed over the concrete pads WASS01 and WASS02, which are located near an AC power source. The first generation MUTE device MUTE-1 was installed

Figure 3.2: (a) Map of test site with the network of devices in 2016, showing the locations of the devices deployed at the test site. LVL1 and LVL2 represent the same locations used in Wassenaar - I to setup levelling device to measure height changes between the concrete pads. (b) MUTE RT with the installed solar panel at the test site. (c) Locations of RTs at the test site with MUTE-1 in foreground and MUTE-2 in the background. (d) Location of CRs at the test site, in the background from the MUTE-1 location. Zoomed inset image shows the ascending-descending pair.

over the larger pad WASS01 of 2 m by 2 m while the second generation device MUTE-2 was installed over the pad WASS02 of dimension 1.5 m by 1.5 m. Figure 3.2c shows their relative positions on the test site. The MUTE transponders have a vertical pole with a base plate that is attached to the concrete pad using three bolts. The baseplate was levelled using the provided adjustable screws and spirit level. Using the Trimble R8 GPS system the MUTE RTs are aligned with respect to the geographic north and their positions are measured with an accuracy of 1 cm. They are connected to AC power and the solar panels are installed (Figure 3.2b). The devices are protected using a temporary fence against large animals. In the previous experiment, each pad was provided with a levelling marker close to the center of the pad. On WASS01 and WASS02, two markers are provided on two ends of the pads - 0.7 m east and 0.7 m west to the center of the MUTE basepoles, as seen in Figure 3.3a, in order to measure its tilt in the subsequent levelling surveys (Section 3.4.1). Also, additional reflective markers are attached to each MUTE over its basepole, eastern and western face of its radome (Figure 3.3b) for subsequent Total Station measurements (Section 3.4.2).

(a) (b)

[Source: Photographed by Dr.ir. H. (Hans) van der Marel] [Source: Photographed by Dr.ir. H. (Hans) van der Marel]

Figure 3.3: (a) Concrete pad of a MUTE RT showing the levelling markers 0.7 m east and west to the center of the basepole with an inset image showing one of the markers in more detail. (b) Reflective markers attached to a MUTE RT at the east-west face of the radome and to the basepole to act as a target for the Total Station measurements.

A file with the mission schedule was uploaded on 27th September 2016 and MUTEs have been operational since that epoch. On 7th March 2017, at 12:50 UTC, a deliberate movement of 7 mm in MUTE-1 was introduced as a part of the blind-detection experiment. The object of the experiment is to check the value and precision detected with the InSAR technique. Since 13th April 2017, the power source of the MUTEs has been changed from 240V AC to the solar power.

Two CRs, one for ascending track and descending track each, were installed on either side of WASS06 on 4th February 2017 as shown in Figure 3.4a. These are aluminum triangular reflectors with each leg length of 1.425 m. The CRs are mounted on an iron frame with square plates of 30 by 30 cm attached to its corners. A 25 cm deep groove is dug into the ground in the shape of the iron frame (Figure 3.4b). The CRs are mounted on this square iron frame and stiffened using metal rods and wires.

The boresight angle of the CRs - angle to the peak RCS direction measured from the vertical axis of the CR - is 61.42°. The CRs are kept undisturbed once initially installed and the boresight is fixed. Thus it is not possible to point the CR to maximize the RCS for each satellite, and a choice has to be made to maximize RCS for either Sentinel-1 or TerraSAR-X. Since the RCS of the CR is lower for C band relative to X band, the boresight is aligned to maximize the RCS for Sentinel-1. Thus the CRAS should be aligned to the ascending track of Sentinel-1 and CRDS to its descending track. Sentinel-1 is a constellation of two polar orbiting satellites - Sentinel-1A and Sentinel-1B - that operate 180° apart which allows a greater coverage and global revisit time of six days [56]. Thus there are two sets of tracks available from the ascending pass (track t088 & t161) and descending pass (track t037 & t110) of both satellites. The CRAS is aligned to the average incidence and azimuth dip angles of tracks t088 & t161 of the ascending pass and similarly, CRDS is aligned to the mean viewing directions of tracks t037 & t110 of the descending pass. These values are reported in Table 3.1.

(a)

(b)

Figure 3.4: (a) The ascending and descending CRs after installation near the concrete pad WASS06. (b) Image just prior to CR installation showing the iron angle frame over which the CR rests and the 25 cm deep groove excavated into which the frame is subsequently lowered.

[57] provides the theoretical relationship between the geometry of a CR and its RCS by equating the reflection from CR's apex to an equivalent flat plate of area A_{eq}. This relationship, for a signal of wavelength λ is expressed as

$$\text{RCS} = 4\pi \frac{A_{\text{eq}}^2}{\lambda^2}. \tag{3.1}$$

Using this expression the theoretical RCS value for C-band and X-band radar at this boresight is obtained as 40.65 dBm^2 and 45.71 dBm^2 respectively. Since the devices are pointed in the average track direction, its orientation as observed from different tracks will be slightly misaligned. Hence, the theoretical values will be slightly lower than those obtained at boresight (see Section 4.4.1 and Section 4.4.6). The coordinates of the apex of the CR are measured using the Trimble R8 GPS system. SAR acquisitions over the test site after 4$^{\text{th}}$ February 2017 include responses from CRs and MUTEs.

Between July and August 2017, both MUTE RTs are briefly turned off and the devices were not operational between these epochs. From 3$^{\text{rd}}$ August 2017, the MUTE devices are turned back on and subsequent acquisitions are obtained until the MUTE devices were removed on the 4$^{\text{th}}$ of September 2017.

In August 2017, also two new experiments started at the test site in the framework of other projects. One project involved several prototype double backflip (DBF) corner reflectors [8]. On August 3$^{\text{rd}}$ 2017, a mockup of the DBF (DBFm) was installed at location WASS03. The mockup was subjected to several changes and on November 4$^{\text{th}}$ 2017, the mockup was replaced by a new prototype. The change in the device setup that is relevant for the study occurred on August 19$^{\text{th}}$ 2017. At this epoch, different components of the ascending mode of the DBFm CR are subjected to a deliberate tilt of about 4.4° as part of the experiment for the other project. This contributes 5 mm movement in the LOS direction for Sentinel-1 track t088 and 0.8 mm LOS movement for track t161. On 10$^{\text{th}}$ August 2017, the first Electronic Corner Reflector (ECR) for the second project was installed at WASS04. On August 13$^{\text{th}}$ the second and third ECR were installed. ECR1 and ECR2 were both installed at WASS04, one for descending track (ECR1), and one for ascending track (ECR2). ECR3 was installed at WASS05 for ascending track only.

On 4$^{\text{th}}$ September 2017 both MUTE RTs stopped their operations and are removed from the site. On the 5$^{\text{th}}$ of November, two new prototype DBF corner reflectors were installed. The DBF mockup at WASS03 was replaced by the DBFX and at the former locations of MUTE1, on WASS01, the device DBFT was installed. The DBF CRs are designed to operate for both ascending and descending passes. Similar to the CRAS/CRDS installation, the boresight of each face is aligned to the average viewing geometries of tracks from the corresponding ascending and descending pass. The ECR devices are also aligned to the average viewing geometries of the respective pass (ECR-1 aligned to the average angles of track t037 & t110, ECR-2 and ECR-3 aligned to the mean geometry of track t088 & t161). These alignments are reported in Table 3.1 for each device. No other changes to the test site have been made during this time period, except occasionally trimming the grass field.

This timeline of device installation and operation is shown in Figure 3.5 and Table 3.1. This study involves analysis of the Sentinel-1 acquisitions between 28th June 2016 and 17th March 2018. Since some of the devices were operational at the site after March 17th, their end dates are not provided in Table 3.1. The Figure 3.5 shows that location WASS01 has been used by MUTE-1 and DBFT. At WASS03, the double backflip mockup CR DBFm was subsequently replaced by a DBFX CR prototype. ECR1 and ECR2 share the same location WASS04 with ECR1 operating for descending passes and ECR2 for ascending tracks. However, ECR1 had some issues during its operations and very few images were acquired for this device. Since this study concerns the time series analysis of the RCS and phase results obtained from Sentinel-1 acquisitions, the results from ECR-1 are deemed too short for analysis for this study and are not discussed here. The phase results are analyzed as double-difference of pairs obtained for different PS combinations. The presence of conventional CRs on the test site is long enough for it have a significant operational overlap with all the remaining devices. Thus, each device is paired with CRs to carry out double-difference analysis that is discussed in the Chapter 5.

INSTRUMENT	TYPE	SYSTEM	LOOK	START DATE	END DATE	LATITUDE [deg]	LONGITUDE [deg]	HEIGHT [m]	ASCENDING		DESCENDING	
									INCIDENCE [deg]	AZIMUTH [deg]	INCIDENCE [deg]	AZIMUTH [deg]
CRAS	Square based ASC Triangular CR	*	ASC	04-02-2017	-	52.12220641	4.38901537	43.50	37.50	259.05	-	-
CRDS	Square based DSC Triangular CR	*	DSC	04-02-2017	-	52.12224247	4.38893272	43.52	-	-	40.67	100.05
MUT1	MUTE (Speng) RT	S1/TSX/CSK	*	25-10-2016	04-09-2017	52.12195395	4.38848089	44.37	-	-	-	-
MUT2	MUTE (Speng) RT	S1/TSX/CSK	*	25-10-2016	04-09-2017	52.12169717	4.38896942	44.40	-	-	-	-
DBFm	Double Backflip CR mock-up	*	*	03-08-2017	04-11-2017	52.12136109	4.38937711	43.39	37.50	259.00	40.67	101.00
DBFT	Double Backflip Triangular CR	*	*	05-11-2017	-	52.12195395	4.38848089	44.37	37.50	259.00	40.67	101.00
DBFX	Double Backflip eXtended CR	*	*	05-11-2017	-	52.12136109	4.38937711	43.39	37.50	259.00	40.67	101.00
ECR1	(Metasensing) Electronic CR	S1	DSC	10-08-2017	28-02-2018	52.12152705	4.38974799	43.47	-	-	38.00	100.80
ECR2	(Metasensing) Electronic CR	S1	ASC	13-08-2017	28-02-2018	52.12152705	4.38974799	43.47	38.00	259.20	-	-
ECR3	(Metasensing) Electronic CR	S1	ASC	13-08-2017	28-02-2018	52.12190956	4.38942611	43.40	38.00	259.20	-	-

Table 3.1: Table with the location and durations of the different types of PS devices used in the experiment. The locations are determined by Trimble R8 GPS system with a horizontal accuracy of 1 cm and vertical accuracy of 2 cm. The height coordinates of the RT includes the height of the pole. Symbol '*' represents that the corresponding entry supports all sensors or tracks depending on the column. The last two columns report the alignment of the device. The end dates of the devices operational after the time period covered in this study are not provided.

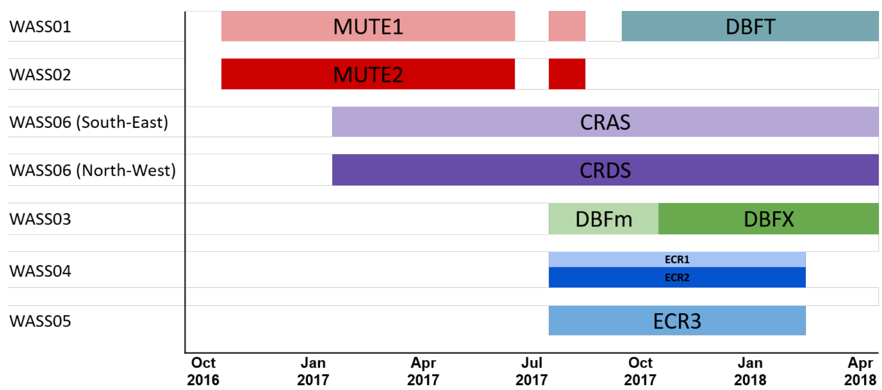

Figure 3.5: Chart showing the locations of the various PS devices at the test site and the duration of their operation. The y axis represents each location against the time axis. Each PS device is represented by the bar with the color representing the type of the device. Different shades of colors are used to differentiate devices of the same family. Devices MUTE1-DBFT, DBFX-DBFm and ECR1-ECR2 have shared the same locations over the time period of study. Conventional CRs (CRAS and CRDS) are operational on the test site long enough to allow for each device to be paired with them for double-difference analysis.

The coordinates in Table 3.1 have been measured using the Trimble R8 GPS system and are utilized for InSAR processing. The coordinates are given in the International Terrestrial Reference Frame (ITRF 2008). The ITRF 2008 coordinate system is very close to WGS84 system. The GPS device has an accuracy of 1 cm in the horizontal and 2 cm in the vertical provided in the European Terrestrial Reference System 1989 (ETRS 89). The measurements were carried out on the pad before the devices were installed and not specifically the position of the device itself. Therefore, the accuracy of the horizontal position is about one decimeter. To account for vertical pole over which the MUTE RT rests, the height of the MUTEs have been measured from the bottom of the pole to the baseplate of the radome four times (from four corners north, south, east and west) and averaged (≈ 1.07 m). The accuracy of these measurement readings are within $1-2$ mm range with a precision of 0.5 mm. This height is added to the reported height coordinate shown in Table 3.1. Figure 3.2a provides a visual map of these positions with device names as labels.

With the complete description of types of ARs on the site and their temporal availability now provided, the next section proceeds to describe the ground survey campaign carried out to measure the stability of these devices.

3.4. Local surveys

This section describes the results obtained from [58] reporting the local surveys that were carried out every couple of months between the time periods of 2016 and 2017. Since that report, an additional campaign was carried out in August 2017. The data from [58] and the new campaign can be found in Appendix A. The following sections have been included to describe the stability of the setup and how it was determined from these campaigns. The stability of the network is checked by testing and measuring the stability of the concrete pad and the vertical pole. Levelling campaigns are carried out to see if the concrete pad is stable or if it is showing signs of subsidence and tilting. Total Station measurements are performed to check the stability of the poles. The following sub-sections covers these techniques.

3.4.1. Levelling

As mentioned in Section 3.3, the concrete pads with MUTE RTs have been provided with two levelling markers, each 0.7 m east and west to the MUTE basepole's center, to monitor the concrete pad's tilting and subsidence. The tilting of the plate is considered to be the change in height difference between the east and west markers while the subsidence value is taken to be average of the two.

The levelling device is placed at LVL1, roughly 30 m away from both MUTE RTs and the measurements are carried out in two circuits each with a clockwise and counter-clockwise loop. Markers on WASS06 and WASS05 are stable and taken as the reference points for the campaign. The accuracy of the height differences measured in this manner is 0.2 mm [58].

The heights of the markers are measured relative to the average height of the two reference points. Then the height differences with respect to the first epoch are computed (double-difference height as reported in Table A.3, Table A.5 and Table A.6).

Figure 3.6 shows the evolution of the heights of these markers to monitor the stability of the concrete pad over time. For MUTE RTs the average measurements from the east and west markers are depicted here. The height differences of MUTE-1 , CRDS and CRAS seem to be stable throughout the entire time period. The height differences of these devices are within the measurement noise. For MUTE-2, the height relative to the reference seem to be declining with time since the first epoch. The velocity of this motion is estimated to be 0.965 ± 0.157 mm/year based on the linear least squares fitting procedure.

In order to assess the tilting of the pad, the heights of both the East and West markers for the MUTE RTs are measured as well. Figure 3.7a and Figure 3.7b shows the height measurements from levelling of the east and west markers through the campaign as measured for MUTE pads. For each device, a difference in the heights of the east and west markers is computed and expressed with respect to the first epoch. Figure 3.7c shows the evolution of differences in height between the east and west markers. From Figure 3.7a, the western marker of MUTE-1 shows a relatively higher decline than the eastern marker but the height difference between these markers (as seen in Figure 3.7c) are still within the measurement noise. Thus the observed tilt of the pad with MUTE-1 is not significant. Figure 3.7b shows the east marker over MUTE-2 subsiding significantly while the western marker is

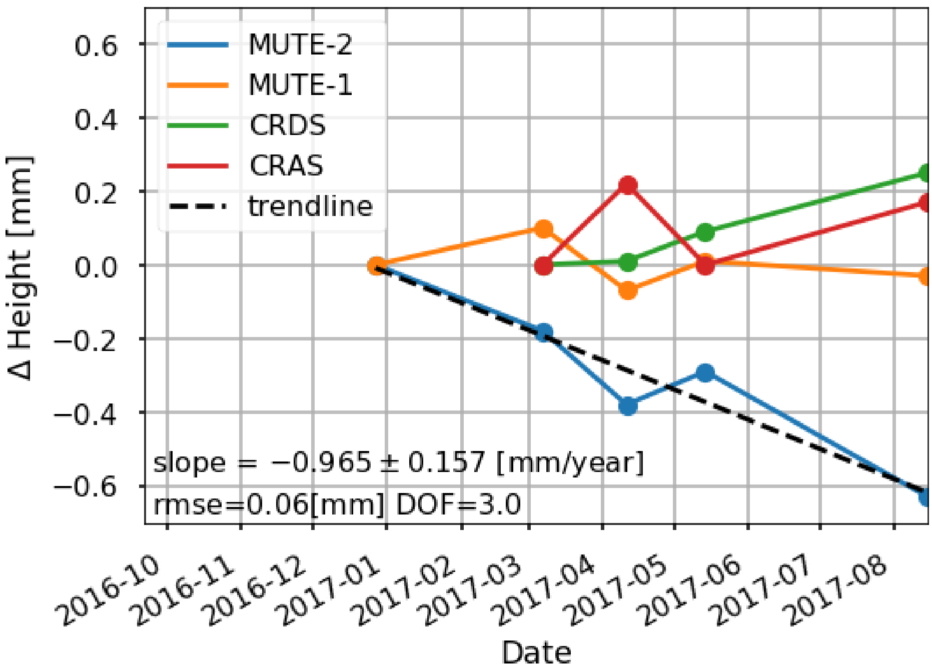

Figure 3.6: Height differences from levelling campaigns between CRs and MUTE RTs with respect to the reference and the first epoch. These results are generated from the data reported in Table A.5. For MUTE RTs the average of the east and west markers are depicted here. The figure illustrates a subsiding trend in MUTE-2 (0.965 ± 0.157 mm/year) based on the linear least square fit, while the height differences for MUTE-1 and CRs seem to be within the measurement noise.

relatively stable. Figure 3.7c shows a higher difference between the heights of east and west markers for this pad. Thus the eastern part of the pad of MUTE-2 is subsiding faster than the western part due to tilt in the concrete pad. As the MUTE devices are installed on a 1.07 meter pole (see Section 3.3, last paragraph and Figure 3.2), rigidly attached to the concrete pad, the tilting of the pads results in an East-West movement of the MUTE device at the top of the pole.

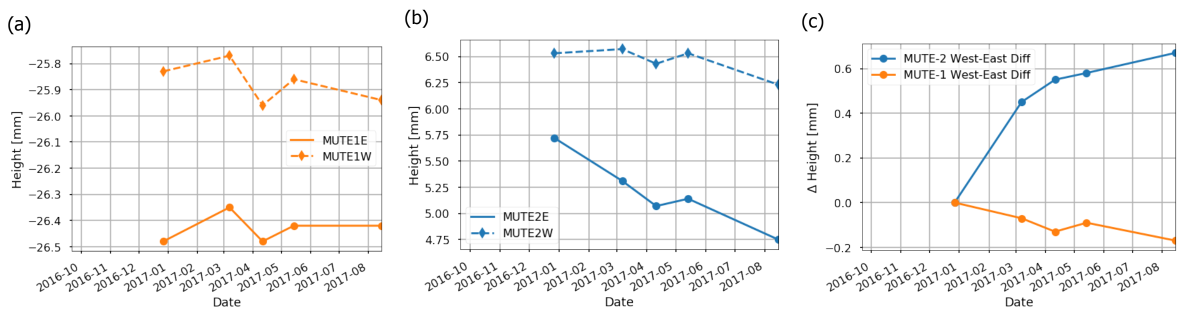

Figure 3.7: Subfigures (a) and (b) shows the measured height of the east and west markers at different measurement epochs for MUTE-1 and MUTE-2 respectively. These observations are reported in Table A.4. The East-West motion for each MUTE is obtained as a difference between the heights of its west and east markers. This signal is expressed with respect to the first epoch and shown in Subfigure (c). Motion in eastward direction is positive here. Tilt in the concrete pad of MUTE-2 results in a higher subsidence of the eastern marker than the western marker.

3.4.2. Total Station

A Total Station is an electronic theodolite that measures distances, angles and coordinates to reflective markers. As mentioned in Section 3.3, each MUTE RT is provided with reflective markers over the basepole, and to the east and west side of the radome. The marker at the basepole is taken as the reference point. The measurements are obtained by placing the device 5 m north of the MUTE RT and are repeated by turning around the face of the device to prevent the collimitation errors. In order to determine the stability of the pole, the difference between east and west marker's 3D coordinates are determined with respect to the basepole using the Total Station device. The change in these coordinates over time represent the movement of the top radome relative to the bottom basepole.

The Total Station measurements are carried out with Topcon GPT 7003i device with an accuracy of 0.5 mm in the Up-Down and North-South direction and a higher accuracy of 0.2 mm in the East-West direction. The Up-Down and North-South components are more sensitive to the distance measurement. While the measurement value in the East-West direction depends more on the angle measurements that can be determined relatively more accurately. Thus, the accuracy of the East-West component is slightly higher than the other two components. Measurements during the first epoch of the campaign were carried out in a different ranging mode, potentially introducing measurement error in the first distance measurement. This is expected to affect the North-South and Up-Down components of the results for the first epoch. Here the focus is on the East-West component which is less sensitive to the ranging error.

Total Station campaign results for displacements measured in three directions (East-West, North-South and Up-Down) are plotted in Figure 3.8. Here West, South and Up directions are positive. The time series is constructed by taking the mean of the east and west markers. Figure 3.8a shows the result for MUTE-1. The resulting coordinates for MUTE-1's Up-Down component show distinctly, the change in height of about 7 mm due to the deliberate displacement applied on 7$^{\text{th}}$ March 2017. Figure 3.8b is generated for MUTE-1 after applying a correction for the known displacement. The east-west component shows a total displacement of 0.3 mm to the west. Figure 3.8c shows the Total Station measurements for MUTE-2. This RT seems to have moved 0.6 mm to the east between the first epoch and 7$^{\text{th}}$ March 2017 after which it moves close to its initial position till 14$^{\text{th}}$ May 2017. The campaign on August 15$^{\text{th}}$ 2017 shows this device moving 0.52 mm eastward again. The movements observed in the results of the Up-Down and North-South direction can be attributed to the measurement errors (especially for the Up-Down component, as the length of the pole has not changed).

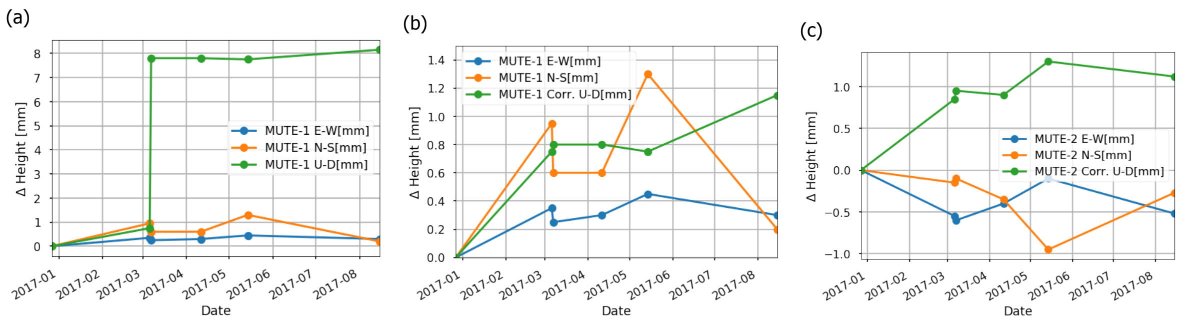

Figure 3.8: (a) Evolution of displacement in three directions as measured from Total Station measurements for MUTE-1. A 7 mm jump the Up-Down component can be seen. (b) Shows the same result as (a) but the data has been corrected for the known deliberate displacement. (c) Displacement evolution from the same campaign for MUTE-2. Motions in West, South and Up directions are positive.

Since the movement in East-West direction is obtained from levelling as well as Total Station, the following section compares the observations in this direction from the two techniques.

3.4.3. Comparison of East-West component

Comparison of East-West motion for MUTE RTs obtained using levelling and Total Station provides a further understanding of the movements of these devices at the test site.

Figure 3.9 shows the comparison of the east-west movement of the concrete pad as measured in the levelling campaign and the east-west component of the movement of MUTE radome with respect to the basepole measured from the Total Station. The slope estimates and quality of linear fit for MUTE-2 are also reported.

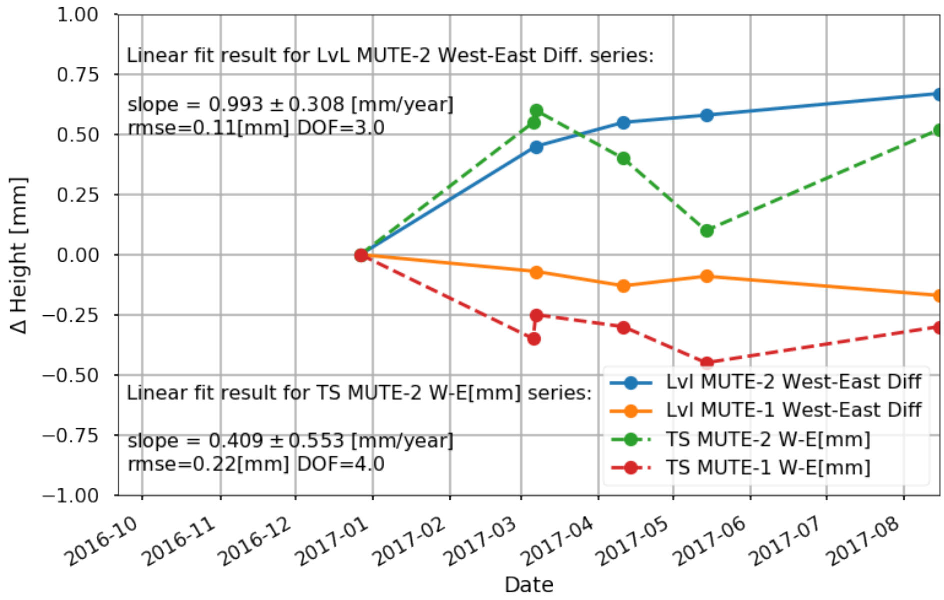

Figure 3.9: Comparison between the East and West markers (installed over the concrete pad) as measured from levelling campaign and the East-West displacement of the markers (attached to the RT radome) as measured from the Total Station for MUTEs. The east west motion as seen by the Total Station seems in line with the levelling results. Motions in the eastern direction are positive.

The results from both techniques agree on the general direction of the east-west component of the MUTE movements, ie. MUTE-2 moves eastwards and MUTE-1 westwards. The largest difference between the two techniques is observed on the 14th May 2017. There is a distinct difference in the motions of MUTE-2 detected between the period of 7th March to 14th May 2017. Total Station measurements indicate this PS returning to its position as observed on the first epoch while levelling suggests this device continuing its eastward movement throughout this time period. It has to be noted that the Total Station measurements are carried out over the devices while the levelling measures markers over the concrete pads that acts as a platform for these devices.

The differences between the total station and levelling measurements could also be an indication that the poles are flexing under forces exerted by winds. This is also something that is readily observed when shaking the MUTEs by hand; the basepoles are not completely stiff and can flex under force with an amplitude of approximately one mm. When the RT MUTE-1 was being removed from the site, upon termination of its operations on September 4th, it was learned that the installation of the RT had been defective. One of the nuts of the bolt that holds the circular baseplate was loose and thus was not firmly attached to the circular baseplate leaving a gap of 0.65 mm between the top of the circular plate and the bottom of the basepole. This allowed the top of the pole to potentially move 4 mm in the direction of the loose nut. Coincidentally, the device cabinet attached to this RT was aligned toward the same direction whose weight might able to resist the movement in this RT to some degree. This is a possibility but doesn't necessarily have to be the case, especially under strong wind conditions. This point has to be taken into account during the interpretation of the results for MUTE-1.

Using the principle of least-squares a polynomial of degree one is fitted to the signals obtained from MUTEs. Figure 3.10 shows the estimates of velocity received by the linear fitting procedure for MUTE-1 and MUTE-2 from levelling and Total Station techniques. The error bars represent the uncertainty of the estimate obtained as one standard error of the slope parameter. Based on the levelling signal, the MUTE-2's eastward velocity is estimated at 0.993 ± 0.308 mm/year. Based on the

Total Station measurements this velocity is estimated at 0.409 ± 0.553 mm/year. Due to the decline in the signal between 6th March and 14th of May the slope obtained using Total Station is less steep and the RMSE for the fitting procedure, in this case, is high. MUTE-1's linear velocity from levelling campaigns is estimated to be -0.253 ± 0.062 mm/year towards west while from Total Station measurements, westward linear velocity is estimated to be -0.431 ± 0.279 mm/year. The estimates obtained from Total Station measurements show higher uncertainty for signals obtained from both devices. No gaps are seen between the regions bounded by these error bars for the difference in techniques for MUTE-1 and similarly, the error bars overlap for uncertainty in the estimated slopes from both techniques observing MUTE-2. Thus the difference between the estimates obtained from different techniques observing MUTE-1 and MUTE-2 are not statistically significant.

The following section presents the conclusions drawn regarding the stability of the device from the ground survey measurements presented here so that these findings can be contrasted against the motion determined from InSAR measurements.

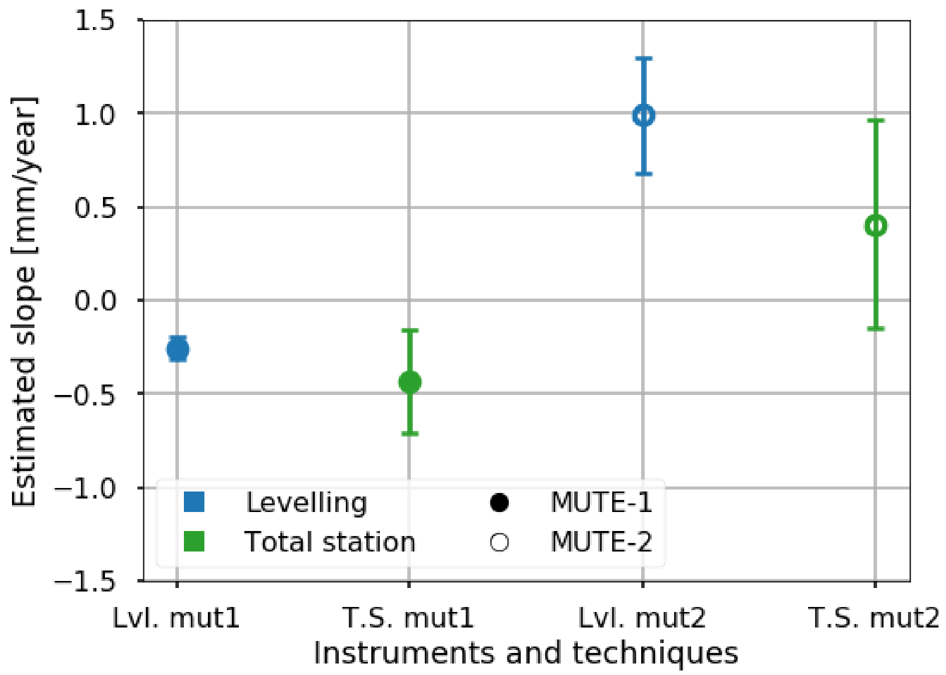

Figure 3.10: Estimated slope parameters obtained using techniques of levelling and Total Station obtained for device MUTE-1 and MUTE-2. The techniques are differentiated by colors and the devices are differentiated by marker style.

3.5. Local survey conclusions

The survey carried out during this experiment show that the concrete pads of MUTE-1, CRAS and CRDS devices are observed to be stable in the vertical direction. This translates to a stable LOS signal obtained from levelling for MUTE-1. However, the loose connection of one of the bolts to the circular plate indicates that this device can move in the horizontal plane (especially under heavy wind conditions). A relatively small westward tilt is detected in MUTE-1 results. The concrete pad of MUTE-2 seems to be subsiding with a rate of 0.965 ± 0.157 mm/year. Furthermore, tilting of the concrete pad of MUTE-2 results in a movement toward the East. The estimated velocity in this direction from levelling data is estimated as 0.993 ± 0.308 mm/yr while the data from Total Station estimates this velocity at 0.409 ± 0.553 mm/yr. The differences in the East-West components from the two techniques can be an indication of poles flexing under strong wind conditions.

The focus of this Chapter was on the setup of the device network for the experiment and quantifying the stability and movements of these devices for the time period of study. The following two Chapters describe the results (in amplitude and phase respectively) obtained from the responses of these devices as recorded from the satellite SLC images of the test site described here. The movements derived from InSAR will be compared to the motions detected by ground survey results that are reported in this Chapter.

4

Analysis of Radar Cross Section

Amplitude, wavelength and phase are parameters that describe a wave where amplitude provides a measure of signal strength. The strength of the reflected signal depends on the target from which it is reflected, this is expressed as Radar Cross Section (RCS). Anomalies in RCS can provide insights into the influence of external factors on the strength of the radar signal reflected back by the devices. Investigating the changes in the magnitude of the signal allows us to test whether factors that affect the strength of the signal and lead to anomaly in the RCS also affect the phase of the signal (research question 3.b). Therefore, analysis of RCS is carried out in this chapter in addition to phase analysis (Chapter 5) to aid the interpretation of phase result anomalies and to explore the nature of influence external factors can have on the performance of the devices. The analysis of RCS is covered here by defining this parameter, describing ways in which it is extracted from SAR images (research questions 1.a, 1.b), considering the influence of external factors on the resulting time series (research question 3.a) and comparing the stability of time series generated from different AR devices (research question 1.c). The following paragraph provides a more detailed outline of results presented in this chapter.

The initial sections provides some context for RCS. Section 4.1 begins with the importance of RCS as a parameter. A formal definition of RCS is provided in the following Section 4.2. Section 4.3 describes the work-flow to obtain RCS based on this definition. It also states the different methods employed to extract signal and clutter from SLC observations. Section 4.4 covers the entire analysis of the RCS time series derived from the work-flow. Section 4.4.1 tests the different approaches of extracting RCS signal against theoretical value in order to select the appropriate method for further analysis. Section 4.4.2 provides a discussion of the statistical distribution of signal and how the expectation of signal and clutter for each device can be obtained. Different methods of clutter observations are compared in Section 4.4.3 in order to determine if the representative value of clutter can be extracted from SLC images. With signal and clutter available from appropriate methods for all devices, Section 4.4.4 points out the anomaly in the RCS time series of MUTE-1 device where an unexpected jump is encountered. Section 4.4.5 covers the anomalies for devices whose RCS performance is influenced by meteorological factors. This section describes how the meteorological dataset is prepared, which type of meteorological events affects RCS response and what is the influence of temperature on MUTE device response specifically. Section 4.4.6 describes the influence of deliberate tilt imparted to DBFm on theoretical and observed RCS. Section 4.4.7 compares and analyzes the stability of device response across different devices. Section 4.4.8 reports the a-priori phase standard deviation approximated using representative value of signal and clutter estimates.

4.1. Importance of RCS measurements

In order to extend the scope of PSI applications, in particular to non-urban areas with low PS density, it is essential to describe the quality of deformation estimates [59].

The quality description of deformation is closely related to the quality description of the interferometric phase. Aside from representing measurement precision, a part of this description is influenced by the physical properties of the PS and their surroundings making it difficult to establish them a-priori. The physical property of a PS shapes the reflected radar pulse. The contribution from the surrounding distributed scatterers (DS) gets superimposed on the reflection from PS, introducing noise in phase and amplitude. As mentioned in Section 2.4.1, the temporal stability of amplitude can be used as a proxy for phase variance. Since the stability of the PS signal is disturbed by the surrounding clutter, the ratio of response from the PS and the background provides a measure of stability that can be utilized to approximate a-priori phase variance. The ratio of responses is known as signal to clutter ratio (SCR).

From [16] SCR is defined as

$$\mathrm{SCR} = \frac{s^2}{c^2} \tag{4.1}$$

where s is the signal amplitude or point target RCS and c refers to the clutter amplitude or average clutter RCS. [60] describes the relationship between SCR and phase standard deviation (σ_ϕ) as

$$\sigma_\phi = \frac{1}{\sqrt{2 \times SCR}} \tag{4.2}$$

Thus quantifying the amplitude response from the PS facilitates approximation of a-priori phase variance. Quantifying the contribution of signal from a PS and clutter of the surrounding DS has not been standardized. This study explores and analyses some of the different ways the response from PS can be quantified to provide a more realistic a-priori quality description of phase.

Amplitude provides a measure of strength of the signal. In practice however, one is interested in the strength with which the target can reflect back the signal, especially when the study is focused on analyzing the performance of different devices. So while amplitude is a property of the signal, RCS provides a measure of the characteristic of the object that reflects the signal. A formal definition of RCS is stated in the following section. The reflectors are therefore designed for specific RCS that they should ideally operate at, giving a measure of the strength of the signal that is reflected by them. As mentioned in Chapter 3, in this study new prototypes of CRs and RTs recently manufactured are tested. The amplitude response of these devices observed from SAR images are obtained in the form of RCS which can be compared against the values claimed by the manufacturer to verify the quality of performance.

By computing RCS, the aim of this study is also to analyze if the signal component of RTs remains stable compared to the response from CR. Computing RCS and phase response of the devices over time provides a basis for comparison and judgment of the pros and cons of using RT devices against CRs. Being electronic devices, decay in performance is a possibility [7] and resulting changes in amplitude could result in the change of a-priori phase variance approximation. This effect can also potentially hinder their phase response affecting their phase stability and introducing an additional error term contributed by the performance of the device. However, unstable phase, in itself cannot point to the presence of this effect as it may represent genuine ground displacement, residual topographic heights and baselength differences. If on the other hand, the stability of the RCS is compromised along with that of phase, it can perhaps indicate the influence of a performance characteristic of the device, especially when no ground motion are detected by alternative deformation monitoring technique used for validation. In other words, analysis of RCS is provided here to test if it can potentially act as an measure of electrical performance of the device that might help explain the lack of stability in phase.

RTs are required to function on a fixed time schedule of satellite overpasses. It is possible, that due to some operational glitch or other practical issues, the device malfunctions on specific days during the satellite overpass, and thus the resulting images records clutter instead of the PS signal. Such malfunctions have been observed in the previous experiments conducted in Wassenaar mentioned in Section 2.8.3, using RADARSAT-2 data. Under such conditions the recorded phase would be decorrelated and correspondingly RCS would drop to the levels of the surrounding DS. Thus, it becomes important to first check if the device was active, and on that basis decide to include or exclude the data point to look at the phase signal. This decision on the mode of operation of the RT can be made automatic and based on the RCS of the transponder signal.

Laboratory experiments carried out on the MUTE prototype have shown that the performance of the device depends on the temperature and introduces error components in amplitude and phase. These tests provide the variation in the signal response under a range of temperature values. For amplitude, the values from these tests are expressed in RCS. Thus changes in RCS of RT are expected to reflect such thermal effects. The aim of this study is to investigate the degree to which the influence of temperature is observed on the phase and RCS results of the devices.

While temperature is the meteorological factor that may effect the RT's response, CRs are potentially vulnerable to precipitation. Such events might lead to a build up of excess snow/rain in their apex that can hinder the signal reflected back to the satellite. To counter this effect, conventional CRs are provided with holes to drain out the excess water. This measure is not always effective in removing excess snow as build-up of dirt and debris are known to have blocked these holes in previous experiments like [49], rendering this counter-measure less effective. The novel design of the new generation CRs used at this site and described in [8, 9] is expected to have some self-cleaning properties under windy conditions. It is reasonable to expect that there will still be some accumulation of snow and dirt in its apex that will influence the results. The stability of RCS and phase results described in this study are used to test whether if this design is able to more effectively counter the influence of build-up in the apex than a CR.

In subsequent sections, different ways to extract RCS are considered and one of them will be selected as a standard way to obtain RCS across all platforms. This selection is based on the comparison of RCS values obtained from SAR acquisitions to the theoretical RCS values of CRs. Unlike transponders, the RCS of the CR depends solely on the geometry of the device, the incidence angle of the incoming pulse and wavelength of the sensor. The relationship between the geometry of the CR and its corresponding theoretical RCS is provided in Equation (3.1). In order to understand the different ways in which the RCS is extracted from the SAR image, it is helpful to first understand how the RCS is defined and how it relates to the SAR image as obtained from the satellite.

4.2. Definition of RCS

RCS is a metric to measure a target's ability to reflect radar signal in the direction of the receiver. The strength of the reflected signal can be determined by comparing it to the reflection of an ideal metallic sphere. RCS expresses the projected area of an equivalent ideal spherical isotropic conductor that would be required to scatter the same power back to the receiver [61]. The unit of RCS is m^2.

Since most objects reflect anisotropically, the reflections from typical targets are significantly stronger than an isotropic sphere. Thus, the comparison to reference yields high values and typically the RCS is converted to the logarithmic scale and expressed in decibel units

$$\sigma[\mathrm{dBm}^2] = 10log_{10}(\sigma[\mathrm{m}^2]). \tag{4.3}$$

RCS is defined in terms of the scattering matrix, providing a relationship between the transmitted and received radar signals in a typical radar system (Section 2.1). For a satellite radar system, this information is available in the form of a product. The Sentinel-1 product is obtained as SLC images whose pixels represent the phasor that contains the information about the amplitude and phase as explained in Section 2.1. Each pixel of a typical SLC image contains the phasor P which can be represented by the following complex number notation

$$P = \mathrm{Re}(P) + j\mathrm{Im}(P), \tag{4.4}$$

where, $\mathrm{Re}(P)$ and $\mathrm{Im}(P)$ are the real and imaginary part of the complex phasor P and j is the imaginary unit. The amplitude A or strength of the radar reflection of a pixel, can be expressed in terms of the real and imaginary part of the complex number as

$$A = \sqrt{\mathrm{Re}(P)^2 + \mathrm{Im}(P)^2}. \tag{4.5}$$

The absolute value of this complex number is sometimes also referred to as Digital Number (DN). The intensity of the radar reflection is the squared measure of amplitude or DN.

The magnitude of radar reflection represents the interaction between the incident pulse and target but it is also influenced by radiometric parameters like antenna gain, system loss, effective aperture of antenna etc. which introduces a bias in the SAR images [44, 62]. These additional contributions which do not represent target properties are accounted for by performing radiometric calibration. Radiometric calibration converts the pixel value in SAR images to one of the backscatter coefficients - normalized radar cross section (σ_0), radar brightness (β_0) or γ_0, that are free from radiometric bias.

Normalized RCS - σ_0 - is dimensionless and represents the RCS (σ) per unit illuminated area projected on the surface. This relation can be expressed as

$$\sigma_0 = \frac{\sigma}{A}. \tag{4.6}$$

If ρ_{az} and ρ_{r} denote the resolution of a SAR image in azimuth and range respectively and θ_{inc} is the local incidence angle, then the illuminated area A in an image pixel can be expressed as

$$A = \frac{\rho_{\mathrm{az}}\rho_{\mathrm{r}}}{\sin\theta_{\mathrm{inc}}}. \tag{4.7}$$

The coefficient γ_0 represents the RCS per unit area of incident wavefront (perpendicular to the slant-range) while the coefficient β_0 - referred to as radar brightness- represents the RCS per unit area projected in the LOS direction. Coefficients γ_0 and β_0 are also dimensionless. Using the geometric relationship, σ_0 can be expressed in terms of β_0 as

$$\sigma_0 = \beta_0 \cdot \sin\theta_{\mathrm{inc}}. \tag{4.8}$$

Following the Equation (4.7), Equation (4.8) and the definition of σ_0 (Equation (4.6)), the RCS of a point target σ, in the line of sight can be expressed in terms of radar brightness by the following expression

$$\sigma = \beta_0 \cdot \rho_{\mathrm{az}} \cdot \rho_{\mathrm{r}}. \tag{4.9}$$

Typically SAR products are provided with calibration factors that allow conversion between these backscatter coefficients.

The calibration factor provided with the product here converts the amplitude to the radar brightness coefficient β_0. For Sentinel-1, the calibration factor (k_{S1}) is used in the following form to obtain the calibrated radar brightness

$$\beta_0 = \frac{1}{k_{\mathrm{S1}}} \cdot |\mathrm{DN}|^2. \tag{4.10}$$

Using Equation (4.9), a time series of RCS estimates can be obtained from the set of SAR acquisition images once they are calibrated to radar brightness. Using Equation (4.3) these estimates are then converted to dB scale.

Thus, the quantity σ, RCS, is actually β_0 converted into the units of RCS. It contains contributions from all scatterers in a resolution cell, the point target under study (CR or a RT device) as well as the surrounding clutter (as represented by the phasor in Figure 2.2a).

The description of how this approach is adopted in the work-flow to obtain RCS using different ways is explained in the next section.

4.3. Processing Methodology

The study [15] describes methods to extract RCS from SLC images for CRs with known theoretical RCS in order to compute the calibration factor required to scale the image so as to obtain a similar response. In this study, the calibration factor is already known and it is used to extract RCS from SLC images. The extraction of RCS and phase for a particular PS from the SLC images requires the location of its dominant signal from the resolution cell. Based on the location coordinates of the PSs, a spatial search window called the signal window is defined to locate this dominant response.

In this study, the dominant signal from an SLC image spatial window is extracted in three different ways. The first method referred to here as **"Peak Mean location method"** extracts the signal from the location of maximum response obtained from the average of SLC image stack during which the PS analyzed is visible. This approach assumes that the location of the PS signal thus obtained from the average SLC image is valid for all operational epochs in the stacks. The second method, **"Peak Instantaneous location method"**, extracts the signal from the location of maximum response obtained from the SLC image for each epoch. The third method integrates the response from the main lobe of the sinc curve which is then scaled by the number of pixels utilized in integrating that response. This method is named as **"Integrated Response method"** and resembles the methods that have been employed in [15, 49]. The responses obtained using these three methods are discussed in Section 4.4.1.

The background clutter that introduces noise in the dominant signal is due to the contribution of the grass field and the exposed top surface of the concrete foundation slab covered by the corresponding resolution cell. Perhaps the clutter level of the concrete slab is lower and less variable than the clutter exhibited by the grass field. Here an attempt is made to determine clutter level from SLC images using three different approaches. As explained in subsequent paragraphs that covers these approaches in more detail, only one of these methods extracts response from the same resolution cell as the PS point and the maximum response in the resolution cell is utilized for this purpose. Therefore, it is likely that the clutter level thus extracted from the SLC images using this approach does not quantify the clutter of the foundation that is in the immediate vicinity of the PS point and it overestimates the clutter value as a result of using the maximum response (since the aim here is to obtain a conservative estimate of a-priori phase standard deviation). In other words, the exposed foundation slab on which the AR device is installed might result in a lower clutter influence on the signal response, however, this cannot be tested using measurements since the strategy adopted here is to get a conservative estimate of clutter for approximation of a-priori phase standard deviation. Subsequent computation of SCR and phase standard deviation from clutter is carried out using Equation (4.1) and Equation (4.2) and presented in Section 4.4.8.

The first approach of extracting clutter from SLC image is based on the assumption that the response of the DS from the same location prior to the installation of the PS device at the test site is similar to the DS response during the period when the PS devices are operational. The first method, called the **"Prior-installation Peak Instantaneous clutter"**, uses the stack of SLC images prior to the installation of the device on the test site to extract maximum clutter response from the relevant signal window. They are used as the representative value of clutter after converting them to RCS in dB scale. Highest value of clutter is extracted from the signal window to obtain a conservative estimate of a-priori phase variance.

The approach described above extracts DS clutter from the same location in space as that of the PS device but at different point in time. While the remaining two approaches extract clutter at same temporal instants as the PS signal but at different spatial location than the resolution cell that the device occupies. Other than the signal window, two additional spatial windows are defined to obtain clutter characteristics from the remaining two methods. The clutter window locations are selected such that they are in the vicinity of the PS device analyzed, that their location is still on the grass field and that the response of scatterers within these windows remain unaffected by the signals of any PS device on the test site (i.e. signal from the sidelobe of the reflector analyzed or other reflectors in the field will not leak into this spatial window). By placing the clutter window in the vicinity of the device, an assumption is made that the response from this window is representative of the clutter at the PS device location. Since the experiment is carried out over a uniform grass field, it is reasonable to state that the assumption holds as physical properties do not vary significantly between the PS location and the clutter window. The second method determines clutter as the mean of the maximum response found within the two clutter windows while the device is operational in the signal window. This mean of maximum observed clutter amplitude is calibrated and converted to RCS in dB scale. This approach is referred to here as the **"Peak Instantaneous clutter"**.

On the other hand, **"Integrated clutter"** is obtained by adding up the response from the two clutter windows and and dividing it by the total number of pixels in the two windows. The idea here is to extract clutter by integrating the response detected by DS across several pixels in the clutter window and scaling it by the number of pixels. A comparison between these three approaches is carried out in Section 4.4.3.

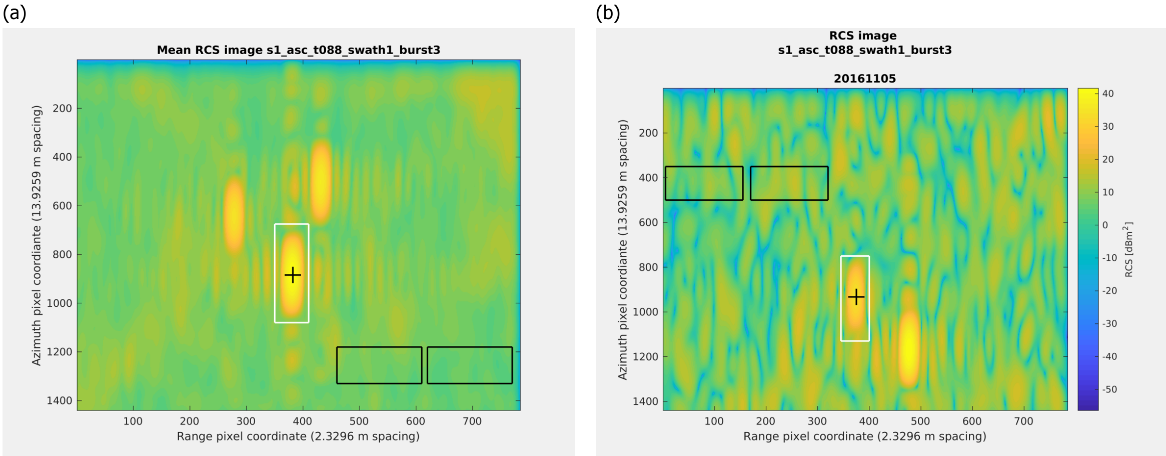

Figure 4.1: (a) Average RCS image obtained by averaging a stack of SLC images from track t088 centered on device MUTE-2. The white box denotes the spatial window of the signal where the dominant signal is extracted using different methods. The black cross denotes the coordinate where the maximum response is obtained from this average SLC image. This location is then subsequently used to extract signal from SLC images for each epoch under the Peak Mean location method. The two black box denotes the clutter windows. (b) SLC image obtained for MUTE-1 during the epoch 5th November 2016. Similar to (a) the signal is extracted from the region bound by the white box and the black boxes are the clutter windows used to obtain the clutter amplitude. The black cross denotes the maximum response obtained from the window for this specific epoch. The location of this maximum response varies from epoch to epoch.

The following list describes the algorithm used in a script to extract RCS, phase and double-difference time series:

1. Generate stacks of SLC images, interferograms, height to phase arrays from S1 SAR acquisitions.
2. Load the metadata of the experiment that contains information necessary for computations, such as the epochs of SLC acquisitions, information about the track, the initial size of the spatial search window, calibration factors, oversampling factors, locations of processing directories etc.
3. Read the separate GPS coordinates file containing the locations, installation and end dates for the different PSs.
4. Determine the bounding box dimensions based on the size of the search window and spacing in the azimuth and range direction.
5. Iterate the following steps for each PS device to obtain the RCS and phase time series:

(a) Check that the crop bounds are within the domain of the SLC image.

(b) Read the SLC images, interferograms and height to phase arrays loading all epochs after accessing them on the high performance computing cluster using the paths provided. For each device, the loaded images are cropped by centering the image on the measured device location. These cropped images obtained at different epochs are collectively stored together in common stacks.

(c) Oversample these images using the factors provided for each case. For the Sentinel-1 sensor, the oversampling factor for range is 16 and for azimuth is 96. (This step improves the resolution of the SLC images and helps in extracting signal more accurately. Approximately square pixels are obtained after this step.)

(d) Convert the stack of SLC images to the stack of images containing the amplitude response by computing the absolute values of the SLC images.

(e) Generate an average response image by computing the average of all the amplitude images in the stack for instances when the PS being analyzed is in "ON" condition. Use indices with 1 and 0 to flag images for epochs when the PS is operational.

(f) Convert the average response obtained to decibel scale.

(g) Use the specified spatial search window of the signal to find the maximum response in the average SLC image. (The location of this maximum response is used to obtain the signal from individual SLC images under the Peak Mean location method).

(h) Find the range and azimuth indices of the maximum response of the average SLC image.

(i) Iterate over individual SLC images from the stack.

(j) Generate an intensity image (digital numbers) for each epoch by squaring the amplitude image and apply the corresponding calibration factor to convert it to the $\beta_\circ$ image.

(k) Generate the RCS image for each epoch by taking the product of the $\beta_\circ$ image with the corresponding area of the resolution cell (Equation (4.9)).

(l) Convert the RCS responses to the decibel scale (Equation (4.3)).

(m) Find the maximum response from the values in the specified signal spatial window.

(n) Obtain signal - i.e. amplitude and phase, from the signal window in three different ways

   i. Peak Mean location method: extract signal from the maximum response location of the average SLC image stack when the device is operational (See Figure 4.1a).

   ii. Peak Instantaneous location method: extract signal from the maximum response location of the SLC image acquired for the epoch for which the signal is to be determined (See Figure 4.1b).

   iii. Integrated Response method: extract signal by integrating the main lobe of the response detected across several pixels in the spatial window and scale it by the number of pixels that covered the main lobe.

(o) Obtain clutter amplitude from signal and clutter windows in three different ways

   i. Prior-installation Peak Instantaneous clutter: extract maximum clutter response from signal window using the selected stack of images prior to the installation of the PS devices.

   ii. Peak Instantaneous clutter: extract the means of the maximum clutter recorded in the two clutter windows for each SAR SLC epoch.

   iii. Integrated clutter: compute the sum of all the responses in the two clutter windows and scale this sum with the total number of pixels in the two windows.

(p) Obtain clutter amplitude by taking the mean of the maximum amplitudes obtained in the each of the two clutter windows.

(q) Convert the stack of phase from radians to degrees. (These are the phase-difference values that will be used to compute the double-differences between different PS devices.)

(r) Write the results to a CSV file with each row representing values from each epoch for RCS and phase.

6. Iterate the following steps for each combination of pairs of all PS to obtain the double-difference time series of phase-differences:
   (a) Generate indices to identify each PS device pairs used for computing double-difference.
   (b) Using these indices compute the difference between the phase-difference values obtained from the previous step.
   (c) Resolve the integer ambiguity in the time series using local gradients to estimate shifts such that the differential phase is in $-\pi$ to π range. For time series that are subjected to deliberate movements, this integer ambiguity resolution has to be done by dividing the time series into two parts, before and after the epoch of deliberate movement so as to prevent false detection of the deliberate movement as an integer shift that needs to be resolved.
   (d) Using the relation from Equation (2.12), convert the differential phase time series from degrees to millimeters. Subsequently, convert this time series in the vertical direction by normalizing it by the cosine component of the provided incidence angle. This provides a stack of double-difference time series in vertical direction expressed in millimeter units.
   (e) Write the results in a CSV file with differential phase values at different epochs along the rows of the CSV files.

Now that the RCS and phase time series are generated in the manner described here, the remaining part of this report is based on the analysis of these results.

4.4. Analysis of RCS time series

This section covers the analysis of signal magnitude obtained as RCS time series. First, by testing the observations against the theory, a choice is made to select the appropriate signal RCS results in order to carry out further analysis. Then the anomalies in the resulting time series are highlighted. The influence of external factors on these anomalies and hence the performance of devices is discussed. The factors considered here include a change in meteorological conditions, influence of temperature on MUTE performance and the effect of deliberate tilt in DBFm on its RCS. Subsequently the stability of the signal from different devices are provided and the effect of accounting for the factors on the stability of signal response is reported. Finally using a representative signal and clutter values, an approximation of a-priori phase standard deviation is obtained. This a-priori value will be compared with the precision obtained from the measurements in the subsequent chapter.

4.4.1. RCS Methods

Section 4.3 describes how the signal response from all PS points is extracted from SLC images using different approaches. This section tests the result obtained using these methods against their theoretical values in order to select the approach that will be utilized to carry out analysis of RCS time series results.

Figure 4.2 shows the RCS signal in dB scale as obtained from SLC data using different approaches. Three different colored box plots mark the three different methods employed to obtain the signal. The box covers the range from 25th to 75th percentile, the interquartile range. The horizontal line in the box represents the median of the distribution. The lower and upper whiskers cover 1.5 times the interquartile range and the data points beyond this range are represented by markers. This comparison is carried out for devices for which a theoretical value of RCS can be determined by their geometrical dimensions using the equations provided in [57].

The theoretical value of RCS is determined by the area of flat plate that would be necessary for the reflection pattern to be equivalent to the CR for which the value is to be determined. This equivalent flat plate area depends on the dimension of the CR - its leg length and its orientation towards the satellite. To maximize the response from the CR, ideally the boresight is aligned towards the direction of the satellite. For Sentinel-1 data however, one must deal with two sets of satellites - Sentinel-1A and Sentinel-1B. Therefore, there are two sets of ascending tracks (t088 and t161) and two sets of descending tracks (t037 and t110) to which the devices can be pointed. As mentioned in Chapter 3, the ascending CRs are pointed towards the average direction of ascending tracks and similarly the descending CRs are pointed towards the average direction of descending tracks. Thus, there is a minor misalignment in both ascending and descending pairs of the tracks as the boresight is slightly off from the ideal direction in all cases which leads to a small drop in the theoretical RCS values that can be expected to be observed from each track. Using the offset in the boresight introduced by pointing the device in the average direction in the expression provided by [57], the lowered theoretical RCS is determined. Device DBFX has a special design where the triangular orthogonal plates have truncated tips and their theoretical RCS (after accounting for the effects of small misalignments) is computed using simulation [63]. These lowered theoretical values are shown in the Figure 4.2 with a purple horizontal line. The radiometric accuracy of the Sentinel-1 system is defined as 0.3 dB (one standard deviation) which is achieved for all operational modes after ESA carried out refinements for Sentinel-1A system [64–66]. This accuracy is represented in the Figure 4.2 as interquartile range using shaded stripes around the theoretical RCS level.

The distribution of the observed RCS extracted from SAR SLC data is shown in the figure by box plots. Different box plots show the results obtained using the three approaches and their position on the horizontal axis indicates the track from which they are observed. The difference in RCS obtained using the three approaches isn't statistically significant. The result obtained from the three approaches are almost equivalent and the choice of the method used to extract the signal will not significantly affect the analysis. The RCS obtained for devices CRAS, CRDS, DBFX is underestimated using all approaches when compared to their theoretical values. A possible explanation of the general underestimation of values (on average 1.28 dBm^2) for these CRs can be attributed to some physical property of the reflector such as buckling of plates, lack of orthogonality of reflection surfaces, surface property changes in the material used to manufacture the reflector etc. which impedes the efficient reflection of the radar pulse back to satellite. Small mechanical deviations of reflection plates in orders of a few millimeters can occur in ground monitoring CR devices. While in the case of CRs manufactured for radiometric calibration, special care is taken to constrain deviations from ideal corner shape (remote controlled CRs deployed by DLR constrain such deviations to ± 1 mm attaining low RCS uncertainty of 0.2 dB for this device [66]) which makes them more expensive. Since the tendency of the observations is to underestimate the RCS level, "Peak Instantaneous" approach is chosen as a method of preference for extracting RCS and phase analysis because the its median tends to be higher across multiple devices.

Several data points in the distribution lie outside the interquartile range of the box plots (black markers in Figure 4.2) in at least one track of all devices shown in the figure. For all devices except DBFm, these low RCS values coincide with extreme meteorological events. In case of DBFm, a deliberate change in the alignment of the devices is responsible for some of these data points. These changes are investigated in the subsequent sections.

Like the signal, clutter is also extracted using three distinct approaches. A comparison between them is reported like the one carried out in this section for signal. Along with the clutter observations extracted from SAR images, the expectation value of clutter derived from amplitude time series is also included in the comparison. The following section describes the distribution of the signal and how the expected value of the signal and clutter can be derived from it. These expectation values will be subsequently utilized in approximating a-priori phase standard deviation.

4.4.2. Expectation of signal and clutter

Amplitude response of point scatterers provides a measure of a-priori phase variance using SCR [10]. Here, the amplitude behavior of the devices is obtained as a time series of RCS measurements. Deriving SCR from the measurements will require representative values of signal and clutter from this time series. Since the underlying distribution of amplitude values is given by Rician distribution, these expected values are obtained using Maximum Likelihood Estimation (subsequently referred to as MLE)[63]. The following paragraphs provides some context regarding the amplitude distribution in a typical SAR SLC image by building on the concepts provided in Section 2.4 in further detail.

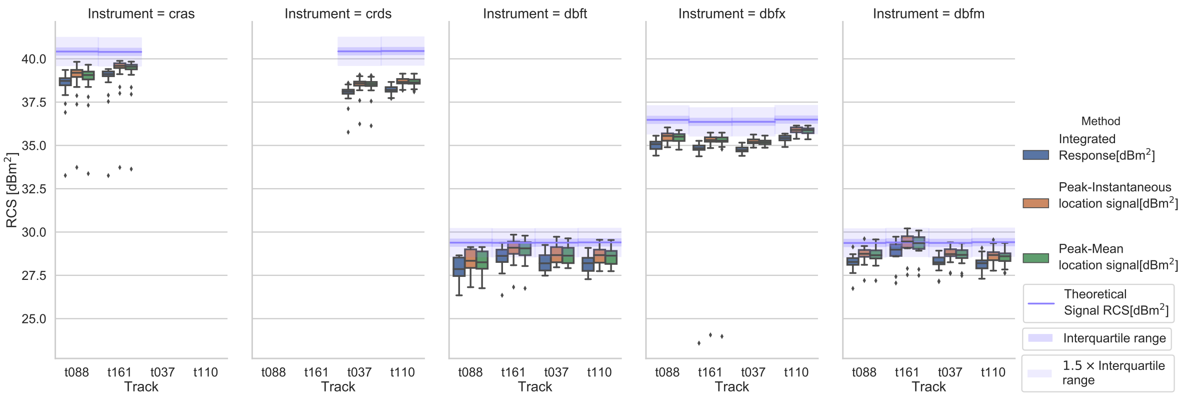

Figure 4.2: Comparison of RCS signal in dB scale extracted from SLC images using three different approaches for CR devices whose theoretical RCS values can be computed using [57]. The theoretical values are obtained after accounting for a minor misalignment caused by pointing the device in the average track direction and are shown in the figure by a purple horizontal line. The shaded stripe expresses the radiometric accuracy of Sentinel-1 system in interquartile range. Three different box plots mark the three different methods employed to obtain signal. Each box plot represents the distribution of these RCS results as observed from each track (which is marked by their position on the horizontal axis). The difference between the results obtained using the three approaches is not statistically significant. Since the tendency of the observations is to underestimate the RCS values relative to theoretical level, results from "Peak Instantaneous" approach are selected for subsequent analysis which have a higher median across the different devices of the three methods.

In a SAR system, typically a resolution cell is large enough to contain several scatterers. Response from each individual scatterer cannot be discerned independently. Rather, the response from resolution cell is modelled as a summation or a superposition of all the individual scatterers present in that cell. In absence of a strong dominant scatterer, the combined response from all other distributed scatterers leads to a random speckle or clutter in a SAR image. In Figure 4.4a, the response from DSs in a typical resolution cell are represented by small vectors whose summation results in a net response of the resolution cell given by the grey dashed vector.

The information about this response is recorded in the SLC image using a complex number - known as a phasor. The expectation and variance of parameters derived from resultant phasor depends on their distributions which are provided in [10] for a resolution cell of DSs. The probability distribution function of this complex observable is represented by a circular Gaussian distribution. Amplitude signal is derived as the length of this vector as shown in the Equation (4.10) and its probability distribution is given by the Rayleigh distribution while the phase is described by a Uniform distribution. Intensity or power, which is obtained as a square of the amplitude is expressed by Exponential distribution.

If, however one of the scatterer in the resolution cell is a PS with high RCS characteristics, then its signal will dominate the net response of the resolution cell while the response from the surrounding DS acts as an additional noise. Figure 4.4b shows this scenario with a vector representation where the larger arrow represents the signal of the dominant scatterer and smaller vectors represent the response from the other elementary DS. The net summation results in the dashed arrow which deviates from the original signal by an amount determined by the response from the surrounding clutter. The amplitude response in this case takes the form of Rician distribution [6]. This distribution is described by mean (the true value of the noise-free signal) and the standard deviation of noise introduced (clutter) [67]. The intensity or power in this case is expressed by scaled χ^2 distribution with two degrees of freedom.

The installation of different devices on the test site is carried out to provide a strong PS point in the relevant resolution cell. Thus, when the devices are operational or in "ON" condition the latter case is applicable and the measured amplitude response exhibits a Rician distribution. Simulations carried out with varying range of signal and clutter magnitudes show that the sample mean and variance are not equivalent to population mean and variance for Rician distributed data or to the true value of the simulated signal (Appendix B). In other words, sample mean and variance are biased estimators and they cannot be taken as representative value for the signal and clutter of the distribution. This bias is stronger when SCR is low. Thus, unbiased estimation of signal and clutter is carried out directly from amplitude times series using MLE for Rician distributed data. Simulations also show that when intensity or power is expressed in dB scale as power levels (a parameter that is similar to RCS, which is essentially calibrated intensity expressed in dB scale), sample mean turns out to be a good estimator of true noise free signal.

The value of a-priori phase variance is obtained here using the SCR derived from the ratio of ML estimate of signal and clutter. This result is reported in Section 4.4.8. The expected amplitude obtained using MLE is converted to RCS as described in Section 4.2 and expressed in dB scale. Table 4.1 reports this value along with the expected value obtained using sample mean and is sorted by the difference in values obtained using the two approaches. The sample mean RCS reported here is obtained by first computing the average in the linear scale and then converting it to dB scale since the logarithm of averages is not the same as the average of logarithms. The number of samples used for obtaining mean is same as the number of observations used in ML estimations. The differences between the expected values from both approaches are within -0.16 dBm^2. This is in line with the results obtained from the simulations which show that the sample mean does not differ very significantly from true noise free signal when the amplitude is expressed as power levels in dB scale.

In summary, the result reported in this section shows that MLE can be employed to obtain an unbiased estimate of device amplitude response that has an underlying Rician distribution. Although, when the amplitude time series is converted to RCS in dB scale, the difference between the sample mean expectation and MLE is small.

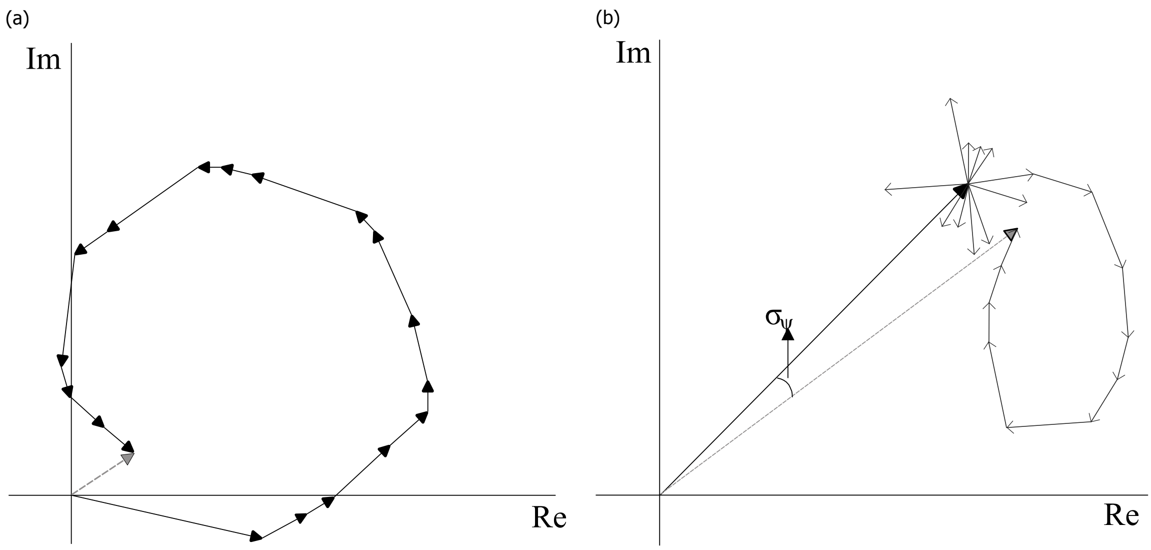

Figure 4.4: Vector representation of scatterer response in a resolution cell. Figure (a) concerns the case where the resolution cell contains multiple DSs, as represented by the smaller vectors. The net response of the resolution cell is modelled as the summation of the all elementary vectors and is represented here by the grey dashed vector. Figure (b) depicts the other case where the resolution cell is populated by a PS whose strong response dominates over the clutter from other DSs. The dominant signal is represented here by the large solid arrow and the smaller vectors represents the response from other DSs. These vectors are shown here translated to the same origin. Their net summation results in the dashed arrow which deviates from the original signal by an amount determined by the response from the surrounding clutter. [Image source: [10, 59]]

4.4.3. Clutter comparison

The clutter responsible for noise in phase is due to the response from the surrounding DSs in the resolution cell. This response cannot be extracted directly when a PS is present because its signal dominates the resolution cell and other DSs cannot be discerned. Here, the three different approaches described in Section 4.3 are utilized to extract clutter from SLC images. However, unlike signal, there is no ”true

Device	Track	No. of samples	Sample Mean RCS[dBm^2]	No. of Observations	ML estimate RCS[dBm^2]	(ML estimate RCS - Sample Mean RCS)[dBm^2]
ecr1	s1_dsc_t037	8	29.825	8	29.661	-0.164
ecr1	s1_dsc_t110	6	34.618	6	34.484	-0.135
dbfx	s1_asc_t161	22	35.048	22	34.934	-0.114
mut1	s1_asc_t161	18	33.664	18	33.568	-0.096
mut1	s1_asc_t088	45	34.226	45	34.169	-0.057
mut1	s1_dsc_t110	41	33.729	41	33.674	-0.055
mut2	s1_dsc_t110	40	39.049	40	39.013	-0.036
mut1	s1_dsc_t037	39	34.059	39	34.025	-0.034
ecr3	s1_asc_t161	19	29.644	19	29.613	-0.031
dbfm	s1_asc_t161	14	29.311	14	29.283	-0.028
dbft	s1_asc_t088	22	28.372	22	28.348	-0.024
cras	s1_asc_t088	65	39.075	65	39.052	-0.023
dbft	s1_asc_t161	22	29.017	22	28.995	-0.021
mut2	s1_dsc_t037	41	38.775	41	38.754	-0.021
cras	s1_asc_t161	67	39.489	67	39.469	-0.02
mut2	s1_asc_t161	18	40.335	18	40.316	-0.019
ecr2	s1_asc_t088	15	32.633	15	32.615	-0.018
dbft	s1_dsc_t110	20	28.655	20	28.639	-0.016
dbfm	s1_asc_t088	15	28.699	15	28.684	-0.015
dbft	s1_dsc_t037	22	28.719	22	28.704	-0.015
dbfm	s1_dsc_t037	16	28.701	16	28.688	-0.013
dbfm	s1_dsc_t110	16	28.634	16	28.622	-0.012
ecr3	s1_asc_t088	21	32.143	21	32.131	-0.012
mut2	s1_asc_t088	45	40.887	45	40.876	-0.011
ecr2	s1_asc_t161	14	32.074	14	32.066	-0.007
crds	s1_dsc_t037	68	38.543	68	38.537	-0.006
dbfx	s1_asc_t088	22	35.496	22	35.492	-0.004
dbfx	s1_dsc_t110	20	35.861	20	35.858	-0.003
crds	s1_dsc_t110	66	38.688	66	38.686	-0.002
dbfx	s1_dsc_t037	22	35.223	22	35.221	-0.002

Table 4.1: Comparison of RCS values obtained using sample mean and maximum likelihood estimation (stated here as MLE) for devices in operational "ON" condition. The table is sorted by the difference in the values obtained using the two approaches. The results in each row provides the representative value for each device as observed from four Sentinel-1 tracks. The sample mean of RCS is obtained by first computing an average in linear scale and then converting it to decibel scale. The ML estimate is obtained by first estimating the amplitude parameter directly from amplitude time series. This parameter is then converted to RCS in dB scale. The number of observations used to compute this estimate are provided in the table and are identical to the number of samples. This result shows that the value obtained using sample mean is close to the value obtained using ML estimation and the differences are within -0.16 dBm^2. Note: The mock-up device 'DBFm' is marked as 'DBF_' here.

clutter" to compare these observations with. As mentioned in the previous section, the expectation value of clutter is also obtained directly from amplitude time series using MLE. This approach is applied here in two ways: a) by estimating clutter using time series prior to installation or **Prior-installation MLE clutter** (Note: this time series will not be available for new devices that replace other devices at the same location) and b) by estimating clutter using amplitude time series after the epoch of device installation or **Post installation MLE clutter** [68]. This method relies on the devices having a constant level of RCS over the entire time series (not an instantaneous estimate). This section tests whether clutter estimated directly from amplitude signal using MLE is in line with clutter RCS observed from SAR images by comparing them.

The clutter extracted from SAR images and the ML estimated clutter levels are compared in Figure 4.5. The parameters represented by the box and the horizontal median line are identical to the one described in Section 4.4.1. The box plot shows the distribution of the clutter observed in dB scale for devices in different tracks. In each case, three different colored box plots are used to mark the three methods used to obtain clutter while the colored error bars depict the expectation value of clutter along with its associated uncertainty estimated using the two MLE approaches.

Comparing results of different observation methods, one observes that, in general, the clutter obtained using the two Peak Instantaneous approaches are similar to each other whether they are extracted prior-installation or during the time period when devices are operational. This shows that the clutter characteristics of this particular grass field does not vary significantly with time for the period of this experiment (with the exception of the clutter derived for device CRDS which exhibits seasonality). Clutter obtained using Integrated method provides lower clutter values relative to the one obtained from Peak Instantaneous approaches (both prior to device installation and during device operational period) by 6.88 dBm^2 on average. Comparing results of different expectation estimates the result shows that across several devices, the Prior installation MLE clutter estimates a lower clutter level than post installation ML estimate that relies on signal amplitude time series. Comparing observations with estimates, the result shows that devices CRAS, ECR-1, MUTE-1 and MUTE-2 the clutter extracted using the Peak Instantaneous method (prior to installation and during device operation) are in agreement with the clutter obtained using post-installation MLE. For devices CRDS, ECR-2, DBFm, DBFT and DBFX (except for track t161) the clutter obtained using the Integrated method is in agreement with the ML estimated clutter. For the remaining device - ECR-3, MLE clutter estimates are lower than the clutter obtained using all three methods. MLE clutter results show a lot of variation across different devices. Depending on whether the ML estimate is relatively high or low , it will be in line with either the peak methods or the integrated method respectively. MLE clutter is not in line with observations from a specific method although it is in similar range of magnitude as the observations.

The following devices on the test site share the same location: i) MUTE1, DBFT and ii) DBFm, DBFX. The ML estimates for the latter pair ii) DBFm, DBFX are similar (difference between the two estimates is not statistically significant) but the post installation ML estimates for pair i) MUTE-1, DBFT are significantly different. Estimating two different clutter levels for same location suggests either that the ML expectation value does not always capture the clutter characteristics of the ground as quantified in this study from SAR images (assuming that the clutter level has not changed significantly with time and its level remains same for MUTE-1 and DBFT operational period) or that the assumption is invalid and the result implies that the clutter level at this location has changed significantly with time. In absence of a "true clutter" value, it is not possible to test either of these possibilities.

Based on the result shown here, no single approach of extracting clutter can be conclusively said to be better than others across all devices. As mentioned earlier, it must be noted that the methods of extracting clutter from SLC images do not capture the clutter characteristics of the foundation slab in the immediate vicinity of the PS point whose clutter characteristics in addition to the clutter of grass field in the resolution cell determines the overall clutter level that influences the signal. Thus, clutter extracted from the response of the grass field in the vicinity of the device location does not necessarily provide a representative clutter that can be utilized to compute a-priori phase variance in PS. And despite the variation in the results obtained for post-installation ML estimated clutter, this approach is utilized to obtain representative value of clutter to approximate the a-priori phase variance based on the results from simulation that suggests that this approach is most adequate to obtain the expectation value.

Thus for each device representative values of signal and clutter are available along with their RCS signal time series. Some of these time series show anomalies that point to the influence of external factors upon device performance. The following sections discuss the influence of these factors on RCS results.

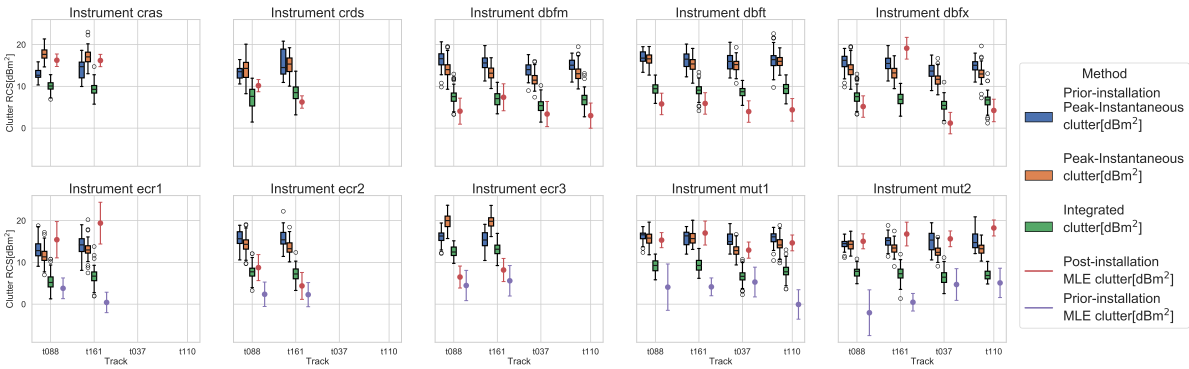

Figure 4.5: Comparison of clutter in dB scale obtained from SLC observations and estimated using MLE approaches for all devices on the test site. The distribution of clutter values obtained from SAR images for each devices in each track is represented by a box plot while the clutter estimates along with their uncertainties are represented by error bars. The position of the box plot and the error bars in the horizontal axis marks the track from which they are observed. Three different colored box plots mark the three different methods employed to obtain the clutter while the two colored error bars mark the clutter obtained using two MLE approaches.

4.4.4. Estimation of step jump

While the RCS time series derived for different device pairs share a lot of similarities, the response obtained from RT MUTE-1 shows a uniquely peculiar behavior. The RCS results obtained from all observation tracks show an abrupt jump in the time series between the epochs of 12th June 2017 and 15th June 2017. Since no changes have been deliberately introduced at the test site during this time period, this jump is unexpected. To clarify this step is only observed in MUTE-1, which is the first generation MUTE RT device, but not in the second generation MUTE device MUTE-2. Figure 4.7a shows this step as a shift in the RCS time series derived for observations from track t088. This step is estimated using the method of least squares and for track t088 is obtained as -1.93 ± 0.30 dBm^2. The result of this estimation for other tracks are shown in Figure 4.7b except for track t161 where measurements from around this epoch are unavailable. The error bars show the standard errors of parameter estimate. An average step of -2.05 dBm^2 is observed across the tracks (as shown in the figure by the black line). The difference in the RCS step is not significantly different across ascending and descending tracks. Since this shift is observed across different tracks, it is unlikely that it represents an error in satellite acquisition images. Section 4.4.5 considers whether a drastic temperature change might explain this step change. The following chapter tests whether these shifts in time series are also observed for phase results and subsequently potential causes for this behavior are explored.

4.4.5. Environmental effects

This section is an attempt to understand the influence of environmental factors on the RCS behavior of different devices on the test site. The first sub-section describes how the meteorological dataset is prepared for this purpose while the remaining two sub-sections report the influence of extreme events found in the prepared dataset on the RCS results and the influence of temperature specifically on RCS results of MUTE RTs respectively.

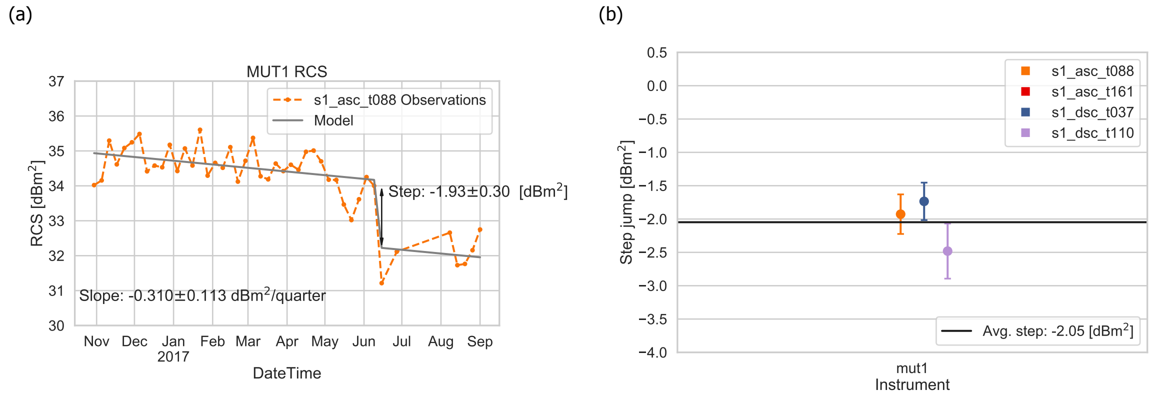

Figure 4.7: Results of step estimation for MUTE-1 RT. a) RCS time series for device MUTE-1 as observed from ascending track t088. The observation time series is modelled as linearly changing with time along with a step in the time series. This step is encountered between 12th June 2017 and 15th June 2017 and is estimated at -1.93 ± 0.30 dBm^2 using the least squares method. The grey line represents the model. b) Step encountered in the RCS time series for MUTE-1 devices as observed across all the processed Sentinel-1 tracks except for track t161 since no observations are available from this track during the epoch of step change. The tracks are color coded as shown in the legend. Error bar represents the standard error of parameter estimate and the black line shows the average step values of -2.05 dBm^2.

Meteorological data

The Royal Netherlands Meteorological Institute (Koninklijk Nederlands Meteorologisch Instituut or abbreviated as KNMI) operates and maintains a network of automatic weather stations covering the entire extent of the Netherlands that record ground observations every day. Weather station at Voorschoten is one such location near the test site where automatic sensors measuring variables such as temperature, precipitation, wind, solar radiation, cloudiness, visibility, air humidity, and air pressure are deployed. Figure 4.8 shows the map indicating the location of this station along with its proximity to the test site at Wassenaar.

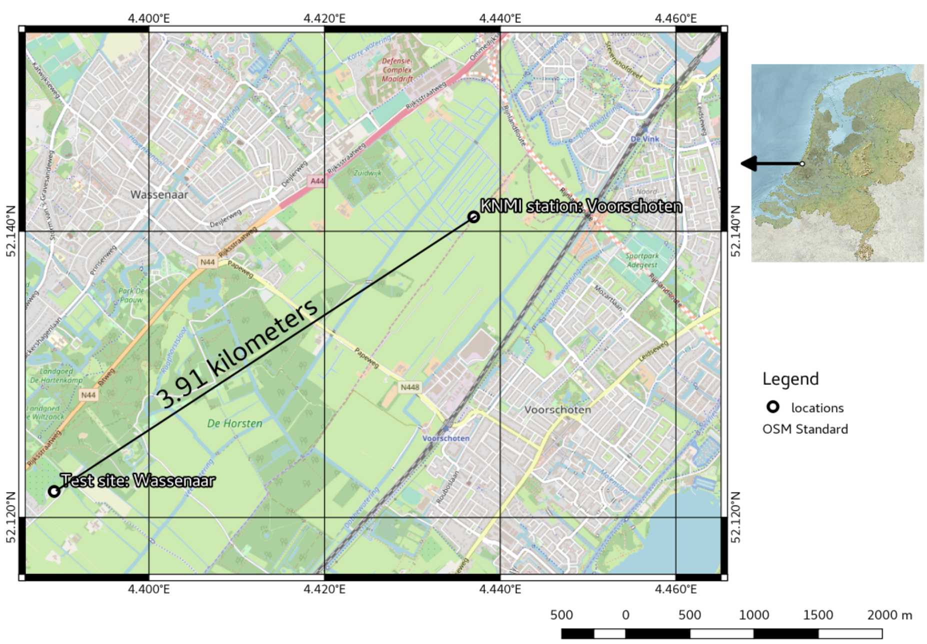

Figure 4.8: Location of the weather station and its proximity to the test site. The distance between the sites is 3.91 kilometers. Map of The Netherlands is depicted at the top right corner.

The data from the meteorological station is publicly available and used for carrying meteorological analysis for the RCS time series in the subsequent section. Here temperature, precipitation, snow and wind speed are used for the analysis as potential variables that might affect the experiment. The conventional CRs at the test site have been provided with small perforations for draining excess water collected during a major rainfall event. However, a chance visit to the site after such event showed that these holes can get blocked, retaining rainwater and snow in the apex that has the potential to alter the reflection of the pulse sent to the satellite. The RTs do not have a geometry that would cause such an accumulation of rainwater. However, according to the specifications provided by the manufacturer, it is known that the performance of the RTs can depend on the temperature. Temperature is not expected to have a direct effect on the performance of CRs. From the previous chapter, it is also known that the stability of the MUTE RTs can be sensitive to wind conditions. To understand what influences these environmental variables might have on the performance of reflectors, the data obtained from the meteorological stations is utilized.

In order to analyze the effects of the different environmental conditions on the site, the duration of the event such as precipitation or snowfall has to be taken into account. The effect of an event such as a thunderstorm might last for duration well beyond the precipitation interval. Considering only the conditions at satellite overpass instances for meteorological analysis might miss such events that have occurred prior to the satellite overpass. The amount of excess water or snow collected in the apex of the corner reflector depends on several factors like the rate of evaporation or melting, the amount of water or snow collected, humidity in the atmosphere, temperature, time of the day, cloud cover conditions, orientation towards the sun, the rate of loss from the drainage etc. To truly determine if a particular event involving these parameters, has affected a SAR acquisition, each satellite acquisition data has to be considered individually with the factors stated above that determine the amount of excess water. These factors are hard to determine and vary on different time scales.

Here, this effect is partially accounted for by utilizing cumulative values for precipitation, wind speed, and snow. Since the satellite data for this experiment involves many acquisitions from multiple tracks, it is pragmatic to set a specific duration period to accumulate the values for all satellite acquisition epochs. In order to determine the set duration for which to assimilate the values, different duration values are experimented with (taking 2, 4, 6, 24, 48 and 72 hours) and the resulting meteorological time series are compared with the RCS time series. The visit to the test site validates the assumption that the unusual dip seen in the RCS time series for CRDS on a specific epoch is due to the heavy rain and snow event that occurred prior to satellite overpass. Different assimilated time series are compared to see which set duration value is able to detect this instance as the extreme precipitation and snow event. Using this experiment, the period of twenty-four hours is deemed appropriate to attribute the unusual changes in RCS seen to the extreme weather event. This duration is long enough to able to flag such instances close to the satellite acquisition epoch while being short enough to minimize false detection of events that have not affected the experiment. It has to be noted that this duration is obtained for this particular site, based on the meteorological observations seen during this time period. It can be expected to vary for other similar experiments.

The results generated using these procedures are discussed in the following sub-sections.

Meteorological analysis

This section tests whether extreme meteorological events such as snowfall, rainfall and strong winds affect the amplitude of the signal returned to the satellite by the deployed devices. As stated above, the recorded measurements of these events are prepared cumulatively for a period of last twenty-four hours before the exact acquisition epoch. Thus, this comparison assumes that the influence of a meteorological event to affect the signal lasts for a day.

Figure 4.10 shows these RCS result time series for devices CRAS (track t088), CRDS (track t037), DBFT (track t161) and DBFX (track t161). Measurement values more than 2.5 standard deviations away from mean are classed as outliers (mean and standard deviations depicted in these results as horizontal lines are obtained after removing them). In the figure, these values appear as sudden dips in the time series and are pointed out using cross markers.

All outliers happen to have been recorded during the epochs where the cumulative rain in the last twenty-four hours exceeds 10 mm (depicted in the figure as ”heavy rain”) or the recorded cumulative snow exceeds 2 magnitude value (snow occurrence is recorded more than twice in the last twenty-four hours) which is referred to as ”heavy snow events”. This shows that accumulated snow/rainwater in the CR apex dampens the amplitude of the signal. This assertion is validated for one heavy snow event on 12th February 2017 when a random site visit revealed that snow gathers in the apex of CRDS. The RCS response of this device is also affected by the snow event on 3rd March 2018. The measurements corresponding to these two epochs are outliers as shown in Figure 4.10b.

The SAR image from ascending track t161 on 11th December 2017 is acquired during heavy snow epoch that dampens the RCS response from conventional CR CRAS (track t161 result for this device is not shown here) and two double-backflip CRs - DBFT and DBFX (Figure 4.10c and Figure 4.10d). On the following day, 12th December 2017, which recorded both heavy snow and heavy rain, the SAR image acquired from track t088 marks a lower RCS only for conventional CR CRAS (Figure 4.10a).

In other words, throughout of this experiment, the conventional CRs are observed to be affected from both heavy rain and heavy snow events while the amplitude performance of next-generation DBF CRs is observed to be susceptible only to select heavy snow events. This suggests that the downward-pointing design of DBF devices drains the excess water collected in its apex. Thus, the design of this device is able to provide an effective drainage solution to this problem faced by conventional CRs. Some snow is expected to stick to the reflection surface and affect the results.

To clarify, the results presented here do not mark *every* rain and snow event that occurred during or twenty-four hours before the acquisition. It only marks the epochs where the cumulative rain and snow exceeded the specified threshold value and such events happen to coincide with outliers. It must be noted that heavy snow and heavy rain events are recorded at other epochs where the RCS response is observed to be stable and only those events are highlighted here which are argued to be affecting the RCS signal. In other words, instances of every RCS outliers coincide with rain and/or snow event, but not every occurrence of such events necessarily leads to RCS outliers.

No significant relation between RCS observations and other meteorological variables (like wind speed, humidity etc.) is observed during this experiment.

The values of RCS response from device ECR-3 as observed from ascending track t161 also exhibit outliers corresponding to snow epoch on 11th December 2017. However, since it is a RT device, this dampening of RCS might be related to either low-temperature conditions (measured 0° C at this epoch) or measurement errors (ECR prototypes used on this site are experimental in nature). Similarly, high RCS recorded for MUTE-1 devices correspond to low-temperature conditions. The effect of temperature on RCS is considered in more detail in the subsequent section.

Temperature correction

Prior to the installation of the MUTE RTs at the test site, temperature sensitivity of these devices is tested by the manufacturer SPENG. The result of this laboratory experiment is available as a set of delta gain values corresponding to a set of temperature observations ranging from $-20°$ C to $65°$ C. This relationship is shown in Figure 4.11 after interpolating values between the data set. The device is considered to work under ideal condition at $27°$ C and the correction factor is set to zero at this temperature. Values beyond this temperature have a negative gain value and the signal obtained for temperatures below $27°$ C is expected to have a positive gain. Based on this relation correction factors for temperatures observed during SAR epochs can be determined. This section evaluates the effect of applying temperature correction for MUTE RCS results.

The correction factors are obtained for temperatures measured at each epoch using gain-temperature relation. However, it is not clear whether to add or remove this factor for applying correction. This is determined by the operation that improves the RMSE of the curve fitting procedures. In Figure 4.12, the RMSE without temperature correction are plotted on the horizontal axis against RMSE obtained

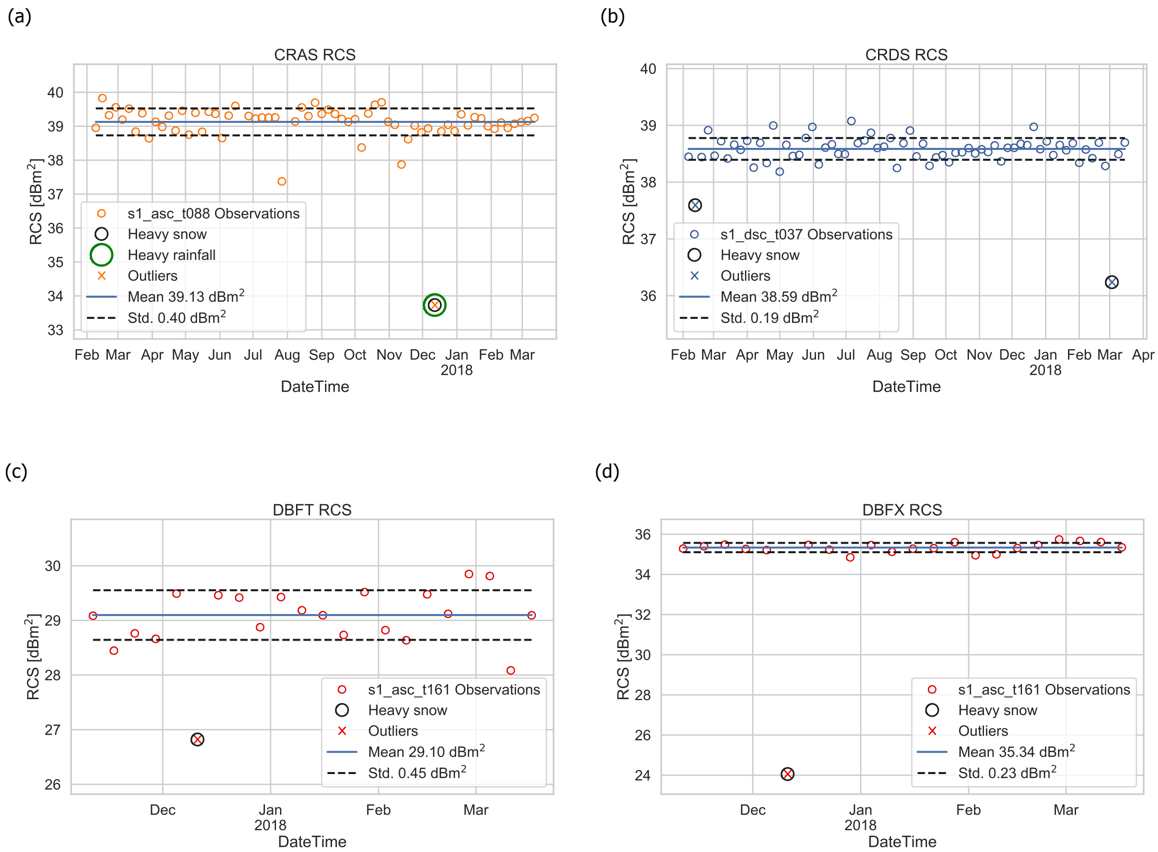

Figure 4.10: RCS time series results derived for devices: a) CRAS from track t088 b) CRDS from track t037 c) DBFT from track t161 and d) DBFX from track t161. Measurements marked with a cross points out the outliers in the time series results. These dips in the RCS results coincide with heavy rain and/or heavy snow events detected prior to the acquisition using a nearby weather station data (marked here using black hollow-circles). The outliers in RCS observed for devices DBFT and DBFX (Figure 4.10c and Figure 4.10d respectively) are affected by the heavy snow event that occurred on 11th December 2017. While CRAS outlier from track t088 corresponds to the heavy snow accompanied by heavy rain on the following day - 12th December 2017 as marked by the green hollow circles in Figure 4.10a. The RCS of CRDS (Figure 4.10b) gets dampened by two heavy snow events that occurred on 12th February 2017 and 3rd March 2018. The resulting mean and standard deviation obtained after removing these outliers are plotted as solid and dashed lines respectively as shown in the figure.

after adding and removing the gain values on the vertical axis. It should be noted that a linear model is fit to the RCS results of MUTE-2, while RCS results for MUTE-1 are modelled linearly with a step jump. The results from MUTE-1 and MUTE-2 are distinguished by marker symbols specified in the legend. The marker faces upward for addition of the correction factor to the RCS and faces downwards when the correction is subtracted from RCS. These markers are color-coded on the basis of the track from which they are observed. As shown in the Figure 4.12, the subtraction of gain value reduces the RMSE errors. Based on the improvement of RMSE observed from this result, going forward the gain values are subtracted from observed RCS to apply temperature correction. The RCS obtained from such temperature correction is analyzed in the following paragraphs.

The temperatures around the epochs of step jump in MUTE-1 RCS are stable. Therefore a sudden temperature change is not responsible for this effect. The overall effect of applying temperature correction is equivalent to a shift in the distribution with a drop in RCS levels of about 0.5 - 2.0 dBm^2. This correction stabilizes the RCS result time series. This is shown in Table 4.2 where applying temperature correction lowers the slope estimated from model fit procedure (exception is the result for MUTE-1 from track t110 where applying this correction increases the slope estimate).

The stability of RCS magnitude gives a measure of device performance. The RCS response from MUTE devices (of both first and second generation type) is not stable as the presence of declining trend shows in the uncorrected RCS time series. This raises the question: why does the RCS signal exhibit this trend? It is known that the RCS response for these devices is influenced by temperature. Generally speaking, the temperature time series corresponding to the epochs of SAR observations rises steadily for the time period during which the MUTE devices are operational. Thus, correlations >0.7 are obtained between uncorrected RCS and temperature for five out of the eight results reported in Table 4.2. Applying temperature correction stabilizes the trend in the result and lowers the correlation with temperature. Thus temperature maybe able to explain the trend behavior in the result. However, the trend in the RCS time series could have also been due to device malfunction in first generation MUTE RT MUTE-1. The performance of this electrical device may be declining linearly with time and this malfunction may have also been responsible for the abrupt step jump in its RCS results. Both these potential causes are weighed against each other in the following chapter that concerns analysis of phase results. If linear trend and step is observed in phase results even after applying temperature correction, then perhaps it lends some weight to the argument that device malfunction is responsible.

To summarize, the effects of applying temperature correction on the RCS results is demonstrated using Table 4.2 which reports some statistics of time series for results prior to and after applying temperature correction. The results from MUTE-1 track t161 are based on few data points and thus its results are rejected here. Rest of the table demonstrates that applying temperature correction stabilizes the time series by reducing the severity of linear slope, lowering the RMSE and reducing the correlation with temperature. However, the cause of linear trend in RCS results may have also been due to an internal device malfunction.

4.4.6. Effect of tilt in DBFm on RCS

Just as a step is observed in the RCS response of MUTE-1 device, another shift in the results is observed for device DBFm. However, unlike MUTE-1, this change is caused by deliberate action introduced at the test site on 19th August 2017. This change involves intentionally increasing the tilt of the device. It is undertaken as a part of another experiment carried out at the same test site which is outside the scope of this study. Since these changes influence the results of the current report, they are briefly pointed out here. In the following chapter, a little more context is provided regarding this experiment where it becomes important to account for this effect for the observed phase results.

Figure 4.14 shows the effect on time series of RCS obtained for this device due to this change. Since the tilt is only introduced in the ascending half of the device, this change is only observed for ascending tracks t088 and t161. It is performed quite early on after the deployment of the device and the data

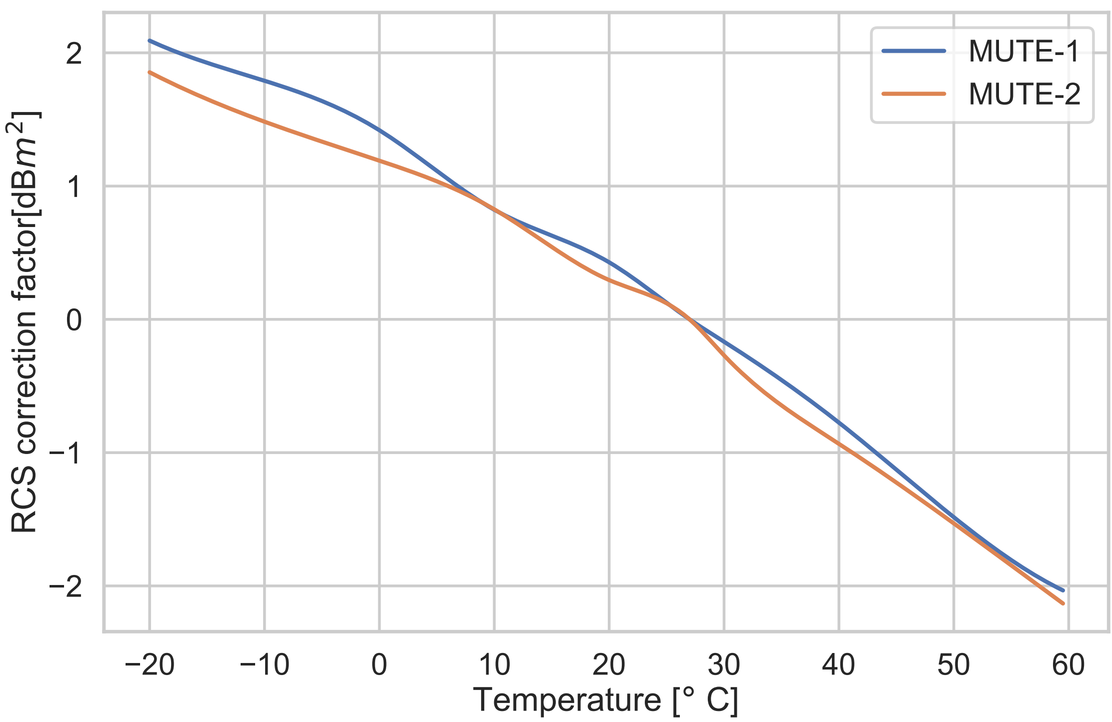

Figure 4.11: Temperature correction factors provided as delta gain over a range of temperature values. The relationship shown here is obtained after interpolating a set of correction factors recorded against temperature for RCS from a laboratory experiment carried out by SPENG. The device RCS operates ideally at 27° C where the correction factor is set to zero. Gain values are negative for temperature higher than this value.

Device	Track	DOF	Uncorrected				Temperature corrected			
			RMSE [dBm^2]	**Slope [dBm^2/quarter]**	**Slope Error [dBm^2/quarter]**	**CC**	**RMSE [dBm^2]**	**Slope [dBm^2/quarter]**	**Slope Error [dBm^2/quarter]**	**CC**
mut1	s1_asc_t088	42.0	0.499	-0.31	0.113	-0.804	0.392	-0.071	0.089	-0.634
mut1	*s1_asc_t161*	*15.0*	*0.52*	*0.531*	*0.298*	*-0.886*	*0.398*	*0.675*	*0.228*	*-0.816*
mut1	s1_dsc_t037	36.0	0.413	-0.164	0.102	-0.74	0.344	0.074	0.085	-0.461
mut1	s1_dsc_t110	38.0	0.671	0.352	0.157	-0.566	0.553	0.562	0.13	-0.307
mut2	s1_asc_t088	43.0	0.337	-0.3	0.054	-0.756	0.29	-0.063	0.046	-0.166
mut2	s1_asc_t161	16.0	0.362	-0.405	0.083	-0.778	0.343	-0.195	0.078	-0.464
mut2	s1_dsc_t037	39.0	0.499	-0.367	0.086	-0.551	0.495	-0.141	0.085	-0.145
mut2	s1_dsc_t110	38.0	0.778	-0.291	0.137	-0.433	0.754	-0.097	0.133	-0.146

Table 4.2: Comparison of different statistics derived from RCS time series to show the effect of temperature correction on MUTE RCS results. The third column provides degree of freedom as a measure of number of observations used to compute different statistics. The results for MUTE-1 from track t161 (italic row in the table) are based on fewer data points (owing to the data gap between April and August 2017) and thus this result is rejected here. RMSE for MUTE-2 device is obtained from a linear model fit to the data. For MUTE-1, a linear model with a step jump is used. Applying temperature correction on RCS results reduces the RMSE of the fit, stabilizes the time series by reducing slope magnitude (with the exception of MUTE-1 result obtained from track t110) and leads to a lower correlation with temperature.

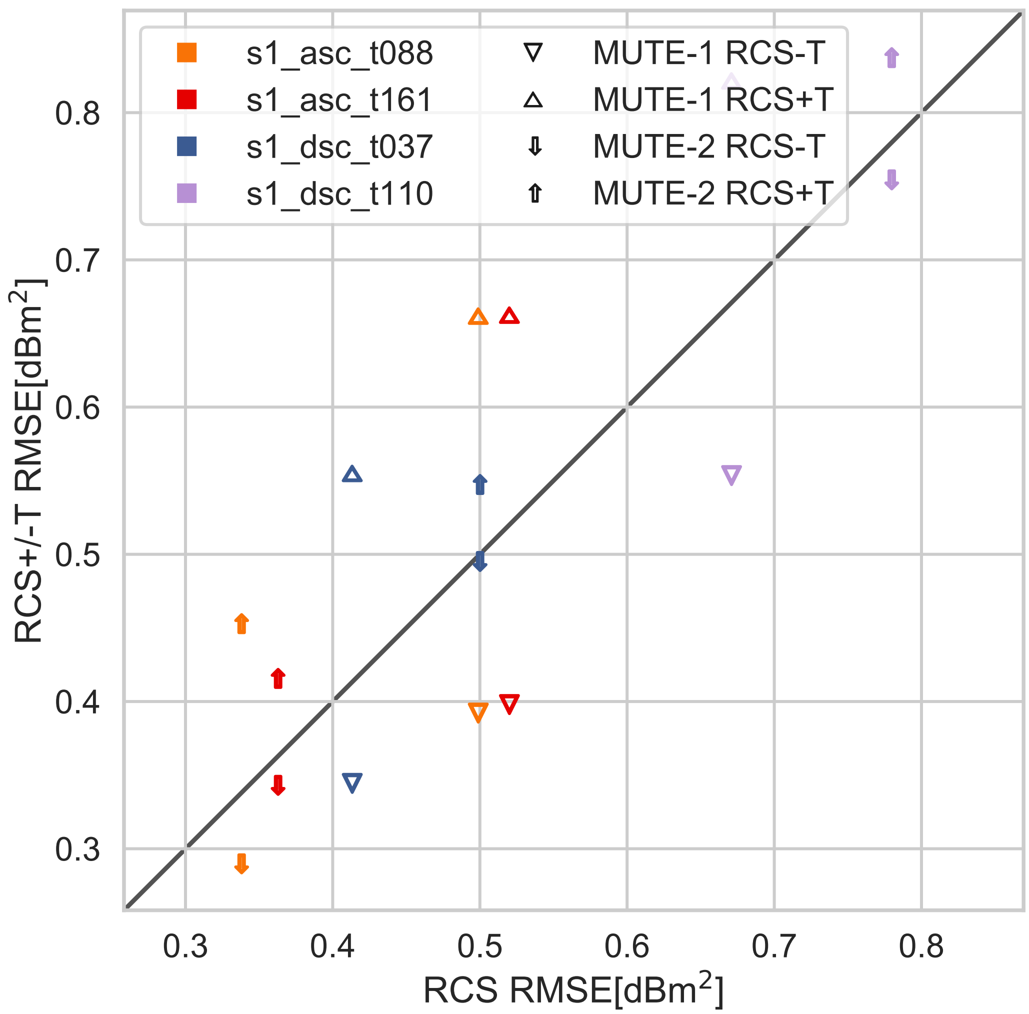

Figure 4.12: Comparison of RMSE values to determine the operation of temperature correction. The vertical axis marks the RMSE values for temperature corrected RCS after addition and subtraction of correction factors. While the RMSE values for uncorrected RCS is marked on the horizontal axis. The RMSE is obtained after fitting a linear model to MUTE-2 RCS and a linear model with a step to MUTE-1 RCS. The marker style distinguishes the device type, the orientation of the marker depicts whether the correction is added or subtracted and the color of the marker specifies the track from which the RCS is observed.

points that correspond to the epochs before introducing this tilt are shown here with cross markers. The gray line represents a linear model with an abrupt shift corresponding to the deliberate tilt fit to the data using least squares. This effect is observed as a drop in the RCS time series for track t088 and a positive shift in track t161. This is in line with expectation as the overall effect of this tilt is an increase in misalignment for track t088 while for track t161 misalignment is reduced.

The reflection surfaces of DBFm and DBFT devices are triangular reflectors, while for DBFX the reflection surfaces are triangular with truncated tips. A more detailed description of the geometrical design choices is provided in [8, 9]. Figure 4.15 shows the RCS characteristics of such triangular reflection surfaces (grey curve) for a range of incidence angles. This curve of theoretical RCS for different incidence angle of the device is obtained based on the geometric dimensions of the reflector (leg-length = 0.9 m), its orientation to the incoming signal (incidence and azimuth of the reflector after accounting for the offsets in orienting the device as reported in Appendix A) and the wavelength of that signal ($\lambda = 0.055$ m) using the relationship provided in [57]. The curve peaks at the boresight angle of $54.74°$ at which the maximum RCS is obtained (as annotated in the figure by a black marker).

As mentioned in Section 4.4.1, ideally, the unit vector from the apex of the CR in the direction of the boresight would be aligned towards the direction of the satellite to maximize the RCS. However, since two sets of ascending and descending tracks are available, a choice is made to align the devices towards average track direction. Therefore, there is a small misalignment as the boresight is slightly off from the ideal direction for all tracks. In addition, there is another misalignment introduced ($0.36°$ in the ascending half and $0.19°$ in the descending half of the device) due to a mismatch between the tilt planned and the actual tilt orientation achieved at the test site. This additional misalignment reflects small imperfections that can be expected in orienting the device of this size despite utmost care and attention. And consequently there is a small drop in the theoretical RCS that can be expected from device response observed from both tracks. This can be observed from the values annotated in the Figure 4.15 using solid circle markers for tracks t088 (29.37 dBm^2) and t161 (29.40 dBm^2) which are slightly lower than the value annotated for boresight (29.51 dBm^2).

On 19th August 2017, the ascending half of this device is tilted towards the direction of track t161 to reduce the misalignment from this track. Since the boresight is now rotated towards the position of satellite in track t161, the theoretical RCS value increases to that of the boresight as shown in the figure by the corresponding ring marker. Moving boresight towards track t161 also means moving it further away from the satellite position of track t088. Thus, there is a further drop in theoretical RCS relative to its maximum value (from 29.37 dBm^2 to 29.03 dBm^2).

These theoretical values for before and after the change in orientation are reported in Table 4.3 along with the RCS response measured from SAR images. Since the change in tilt is introduced early in the experiment, fewer data points are available for observations for before realignment condition. Mean and standard deviation of the observed values are used to represent the measured RCS for the entire duration of the experiment. Two observations for track t161 before introducing realignment are slightly lower than expected as can be seen from cross markers in Figure 4.14b. This leads to higher standard deviation values and a relatively higher difference in this case. However, after realignment, a better agreement between the theoretical and measured values is obtained. Overall the difference between the measurements and their theoretical values before and after applying tilt is within 1.7 dBm^2 and the change in the results of time series is in line with what is expected in theory. Small deviation from theoretical values can be attributed to influence of the clutter in the resolution cell and residual errors in radiometric calibration.

In the following section, which is dedicated to the discussion of device RCS response stability in general, the effect of accounting for this deliberate tilt on the stability of time series is depicted by representing slope estimates obtained before and after removing acquisitions from epochs prior to this deliberate tilt.

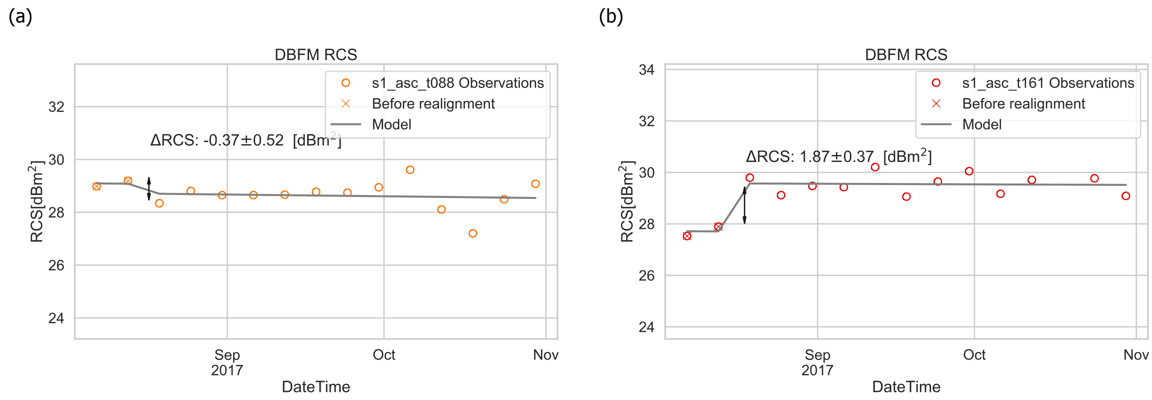

Figure 4.14: RCS time series for device DBFm (marked in the figure title as 'DBF_') showing the effect of tilt as observed from a) track t088 and b) track t161. The time series is modelled as linearly changing with time with an abrupt shift that corresponds to the epoch of deliberate tilt (19th August 2017) imparted to the ascending half of DBFm CR. The grey line represents this model. The measurements carried out before this change are shown here with a cross marker. A negative shift is observed in the RCS results for track t088 while for track t161 there is distinct increase in the RCS level since this epoch. Such changes can be expected as the overall effect of this tilt is an increase in misalignment for track t088 while for track t161 misalignment is reduced.

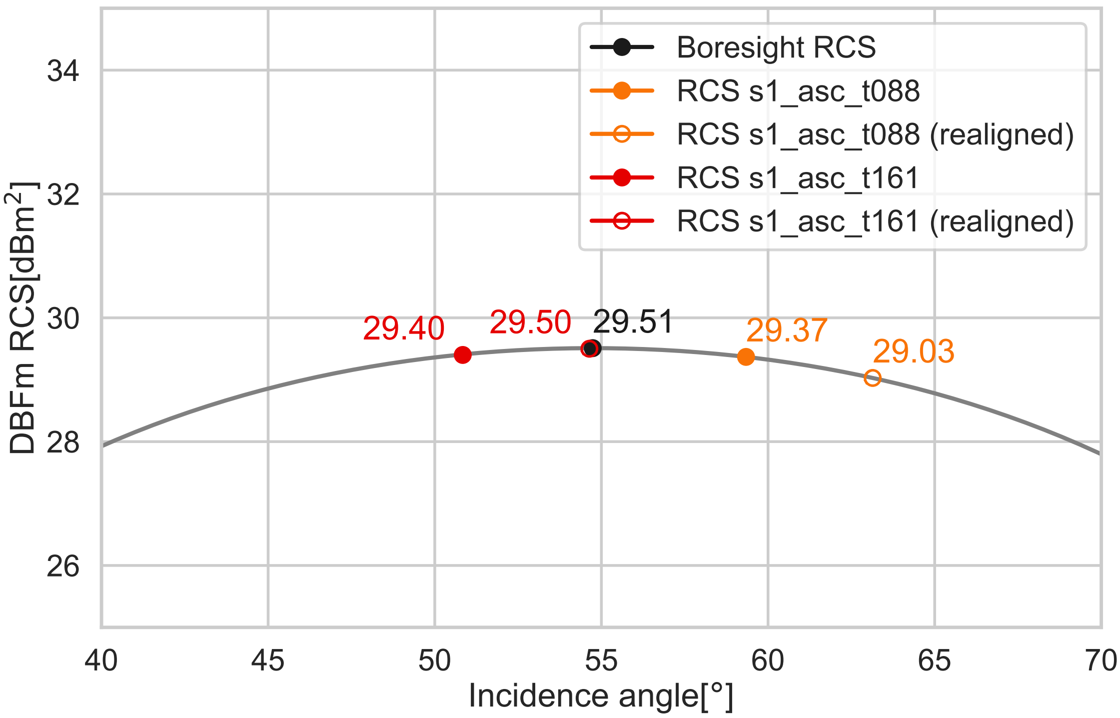

Figure 4.15: Theoretical RCS for triangular reflection surfaces of DBF CRs obtained for a range of incidence angles. The grey curve is obtained from [57] for the parameters applicable for device DBFm ($\lambda=0.055$ m and $l=0.9$ m). The curve peaks at the boresight angle of $54.74°$ with a maximum RCS of 29.51 dBm^2 annotated by the black marker. Initially, the ascending half of device DBFm is planned to be aligned in the average direction of two Sentinel-1 ascending tracks t088 and t161 which introduces small misalignment and leads to a drop in the theoretical RCS for both tracks. The theoretical RCS corresponding to these angles are marked in the figure using a solid circle. On 19th August 2017, this half of the device is tilted deliberately to reduce the misalignment for track t161. The RCS corresponding to this alignment is shown here by ring markers. For track t161, the theoretical value for average direction 29.40 dBm^2 increases to almost the maximum value of 29.50 dBm^2 after deliberate tilt. As this direction is changed in the favor of track t161, there is a further drop in the theoretical value for track t088 (from 29.37 dBm^2 to 29.03 dBm^2).

Track	Condition	No. of observations	Theoretical RCS[dBm^2]	Mean observed RCS[dBm^2]	Standard deviation[dBm^2]	(Theoretical RCS - Mean observed RCS) [dBm^2]
s1_asc_t088	Before realignment	2	29.37	29.09	0.15	0.28
s1_asc_t088	After realignment	13	29.03	28.62	0.56	0.41
s1_asc_t161	Before realignment	2	29.40	27.71	0.26	1.69
s1_asc_t161	After realignment	12	29.50	29.54	0.39	-0.04

Table 4.3: Theoretical and measured RCS for device DBFm as observed from the ascending tracks of Sentinel-1 before and after providing deliberate tilt on 19th August 2017. Since the tilt is introduced early in the experiment, fewer observations are available for "before realignment" condition. The theoretical RCS reported here come from the relation provided by [57] for the parameters applicable to DBFm device at this site as shown in Figure 4.15. The observed RCS for the device is reported as mean and standard deviation of measurements. Accuracy of these estimates relative to theoretical value are within 1.7 dBm^2 with a much lower accuracy for track t161 before deliberate tilt(results for the first two epochs are unusually low as shown in Figure 4.14b) but a much higher accuracy after deliberate tilt.

4.4.7. Stability of device response

The response of a device can be considered to be stable if a near-constant signal is observed from it for each SAR epoch while the device is operational. This stability is therefore quantified here as the strength of the linear trend present in the RCS time series. In an ideal case, a stable device should exhibit no trend in its RCS signal. In practice however, small deviations from zero slope estimates are encountered as a result of variability in calibration factor, amplitude variability of the device as a result of small plate movements and influence of clutter. Variability introduced due to the mechanical movements in the device cannot be modelled here but in general an assumption is made that the trend estimate of the RCS signal for a stable device will be within ± 0.5 dBm^2/quarter. This magnitude has been selected here to identify signal response of devices whose high trend magnitudes cannot reasonably be expected from natural variability, although, this assumption can be problematic for short measurement time series. In this section the stability of different device response are compared by analyzing the magnitude of linear trend estimate using least-squares approach.

Figure 4.16 shows this comparison for different PS devices as color-coded error bars representing the trend with its standard errors of parameter estimate. The result for device ECR-1 have high associated uncertainties and are not included in the Figure 4.16 since these estimates are based on very few data points. The CRs- CRAS and CRDS show most stable behavior over time with slope values closest to zero (slope estimates across different tracks are in the range -0.008 ± 0.0188 dBm^2/quarter to -0.050 ± 0.019 dBm^2/quarter). The slope parameters of these devices have been estimated with high degree of freedom (using more number of data points relative to other devices) and they exhibit lowest uncertainty. Devices DBFs and ECRs on the other hand, have been on the site for a shorter period of time and thus the estimated slope parameters have higher associated uncertainties.

The trend results for MUTE devices are provided for signal before and after applying temperature correction using circular and triangular markers respectively. The slope values discussed here for MUTE-1 are obtained after accounting for the step change in the model. Applying temperature correction stabilizes the RCS response. This is evident from the near-zero slope estimate (within range ± 0.25 dBm^2/quarter) obtained for temperature corrected RCS as depicted in the figure by the triangle error bars. This improvement is observed across all tracks except track t161 and t110 of MUTE-1. The MUTE-1 RCS time series from track t161 have large data gaps and the model fit is carried out on fewer data points as shown by the low degree of freedom in Table 4.2. This result is thus rejected. It should be noted that the trend in the result does not necessarily point to the influence of temperature alone as it might have resulted due to deterioration of device performance due to instrument malfunction.

As mentioned in Section 4.4.5, the outlier measurement points (more than 2.5 standard deviation away from the mean) correspond to epochs of heavy snow and heavy rainfall events. Three cases are shown in the figure where removing these outliers leads to an improvement of slope estimates. The slopes estimated after removing outliers are shown in the figure with square error bars. Removing outlier for DBFX RCS observed from track t161 bring the estimate in agreement with the other tracks of this device. The RCS response of this device is thus found to be stable across all tracks (slope estimates are within ± 0.25 dBm^2/quarter). Outlier removal step also stabilizes the slope estimate for DBFT and

ECR-3 obtained from track t161. For both devices, the RCS response from all operational tracks are found to be stable (slope estimate within ± 0.5 dBm^2).

The ascending half of the device DBFm is subjected to deliberate tilt movement on 19th August 2017 which leads to an abrupt increase in RCS for track t161 and a drop in RCS levels for track t088 (Section 4.4.6). Accounting for this effect fits the model better to the data points and improves the estimate of the trend. However the associated uncertainty of this estimate is too high to conclusively state that the RCS response of this device is stable. These slope estimates and their uncertainties after accounting for this deliberate realignment are shown in the figure using diamond error bars. The RCS response from device ECR-2 show a linear trend during the time period of their operation on the test site. The lack of RCS signal stability for ECR devices observed from the majority of its operational tracks may have to do with a device error specific to this electronic RT. While the high uncertainty in DBFm maybe attributed to imperfect stiffness of this mock-up prototype. Lack of stiffness for this prototype has been documented in [9].

In summary, the fitting procedure with a polynomial of degree one helps identify devices on the test site that show a consistent amplitude behavior with time. The signal response from conventional CRs - CRAS and CRDS are found to be stable across all tracks. Device responses of DBFT, DBFX and second generation RT MUTE-2 are found to be stable once the appropriate corrections are applied to the RCS results, such as temperature correction and outlier removal. Some potential causes for lack of stability are suggested for MUTE-1, DBFm and ECR devices that are not stable.

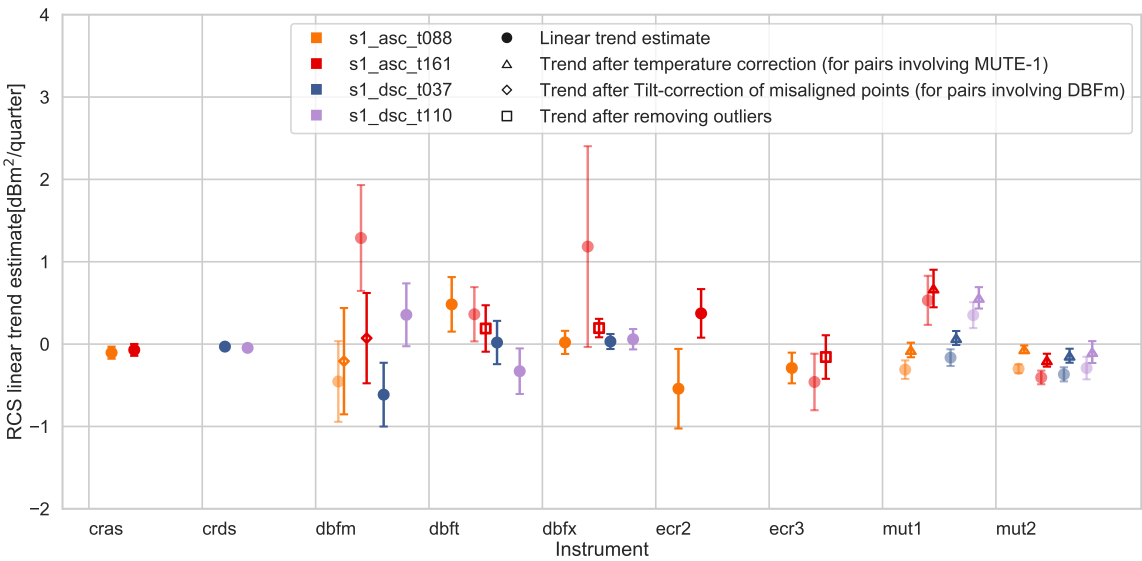

Figure 4.16: Comparison of device magnitude stability represented as the magnitude of linear trend observed in the RCS time series. The error bars represents standard errors of parameter estimate. Device RCS with near-zero slope magnitude are considered to be stable. Using this criteria, CRs CRAS and CRDS are found to be stable. Once temperature correction is carried out device RCS of MUTE-2 is stabilized. The solid markers in the figure represent the slope estimated from RCS without any correction and the triangle marker obtains this statistics for temperature corrected RCS. For MUTE-1 however applying this correction only stabilizes time series for track t088 and t037. Device DBFX is found to be stable across all tracks once the outliers corresponding to extreme snow conditions in track t161 are removed as shown in the figure by the square marker. Removing these outliers also stabilizes the slopes obtained for DBFT and ECR-3 from track t161. Device DBFm is stabilized across all tracks except t037 after the deliberate tilt in the device is accounted for in the ascending tracks as shown by the diamond markers. Response from device ECR-2 are not found to be stable while the results from ECR-1 is rejected because very few RCS data points are available for this device.

4.4.8. Phase standard deviation a-priori approximation

This section reports the a-priori phase standard deviation approximated using MLE signal and clutter estimates. Table 4.4 reports the a-priori phase standard deviation for each device observed from the four Sentinel tracks. SCR is obtained using the amplitude signal and clutter in Equation (4.1).

Device	Track	No. of Observations	MLE signal RCS[dBm^2]	MLE clutter[dBm^2]	SCR	a-priori Phase standard-deviation[mm]
dbfx	s1_dsc_t037	22	35.221	1.204	2521.464	0.062
crds	s1_dsc_t110	66	38.686	6.251	1751.624	0.075
dbfx	s1_dsc_t110	20	35.858	4.23	1454.735	0.082
dbfx	s1_asc_t088	22	35.492	5.165	1078.252	0.095
crds	s1_dsc_t037	68	38.537	10.171	686.42	0.119
ecr2	s1_asc_t161	14	32.066	4.37	588.382	0.129
mut2	s1_asc_t088	45	40.876	15.047	382.686	0.16
ecr3	s1_asc_t088	21	32.131	6.494	366.162	0.163
dbfm	s1_dsc_t110	16	28.622	2.99	365.806	0.163
dbfm	s1_dsc_t037	16	28.688	3.372	340.128	0.169
dbft	s1_dsc_t037	22	28.704	3.967	297.665	0.181
dbfm	s1_asc_t088	15	28.684	4.059	290.093	0.183
dbft	s1_dsc_t110	20	28.639	4.381	266.53	0.191
ecr2	s1_asc_t088	15	32.615	8.75	243.509	0.2
mut2	s1_asc_t161	18	40.316	16.787	225.346	0.208
cras	s1_asc_t161	67	39.469	16.185	212.986	0.214
mut2	s1_dsc_t037	41	38.754	15.642	204.731	0.218
dbft	s1_asc_t161	22	28.995	5.91	203.47	0.219
cras	s1_asc_t088	65	39.052	16.25	190.649	0.226
dbft	s1_asc_t088	22	28.348	5.792	180.132	0.233
dbfm	s1_asc_t161	14	29.283	7.385	154.832	0.251
ecr3	s1_asc_t161	19	29.613	8.177	139.195	0.265
mut1	s1_dsc_t037	39	34.025	12.935	128.512	0.275
mut2	s1_dsc_t110	40	39.013	18.242	119.419	0.286
mut1	s1_dsc_t110	41	33.674	14.664	79.616	0.35
mut1	s1_asc_t088	45	34.169	15.326	76.618	0.357
mut1	s1_asc_t161	18	33.568	17.025	45.11	0.465
dbfx	s1_asc_t161	22	34.934	19.127	38.081	0.506
ecr1	s1_dsc_t110	6	34.484	19.399	32.247	0.55
ecr1	s1_dsc_t037	8	29.661	15.428	26.507	0.606

Table 4.4: A-priori phase standard deviation for each device and track as approximated from the SCR. The signal and clutter estimate used to obtain the SCR is obtained for each device using MLE. Amplitude estimates of signal and clutter are used for obtaining this ratio, however, these values are reported here in dB scale for comparison. The a-priori standard deviation is obtained using Equation (4.2) in radians and is reported here after converting it to millimeters. The table is sorted by this final column. The magnitude of this approximation depends strongly on the signal and clutter estimate obtained. Note: The mock-up device 'DBFm' is marked as 'DBF_' here.

These parameters are reported in the table in dB scale. A-priori phase standard deviation values are derived from SCR using Equation (4.2) in radians and are reported in the table after converting them to millimeters. The table is sorted by this precision. The a-priori phase standard deviation depends on the magnitude of the signal and the degree to which it varies due to surrounding clutter. In the following chapter, these values are compared to the precision obtained from observations posteriori. This comparison tests how accurately the precision of the result can be approximated using the signal and clutter extracted in this study.

Just as this chapter covers the description and analysis of amplitude response, in a similar vein, the following chapter is dedicated specifically to the description and analysis of phase parameter from different ARs.

5

Analysis of phase

The technique of interferometry utilized for geodetic applications relies on the phase property of the radar signal to obtain a measure of change in range between the platform and the target. Using this range component of the phase result, knowledge about topography or deformation of the coherent scatterers can be discerned. Here, the deformation characteristics of the different kinds of reflector devices are determined that are prominent and persistently coherent scatterer points at the test site. Since no significant natural ground movement is expected from this test site, the deformation characteristics of different devices installed on it allows us to determine the stability of their phase results and to test whether the phase response of the devices is affected by external factors or is influenced by the choice of the type of reflector employed. The first form of phase observation that can be used for the interpretation of deformation is a double-difference, that is, an observation obtained as a difference in space and a difference in time [33, 59]. The interferometric phase result of a scatterer is the temporal difference in observation between master and the slave acquisition epochs. These interferometric phases are subsequently subtracted from the phase of the reference point to obtain a spatial difference as well. Thus, the phase results described in this Chapter are obtained as double-difference observations (displacement time series) and expressed in millimeters. The analysis covered in this chapter using such double-difference observations involves testing the InSAR estimated MUTE-1 deliberate movement against the ground truth (research question 2.a), validating vertical and horizontal deformation signal from InSAR with the signal determined from ground survey (research question 2.b), accounting for the influence of external factors such as temperature and device malfunction (research question 3.a), quantifying the effect of deliberate tilt in DBFm in phase results (research question 2.a) and comparing the stability of double-difference time series generated from different AR devices (research question 1.c). The general outline of how these results are presented is described in the following paragraph.

Section 5.1 describes the deliberate movement experiment carried out for RT MUTE-1. It also concerns with the additional step in the observed time series. In Section 5.2, these displacement results are compared to the measurements obtained from ground survey movements described in Chapter 3. In order to explore the cause of disagreement between the InSAR and ground survey techniques for pairs involving MUTE-1, in Section 5.2.1, the data from different InSAR observation tracks is combined to account for the horizontal movements. A fresh comparison is then carried out between the two techniques. The role of temperature correction and the potential of a device malfunction is considered in Section 5.2.3. Section 5.3 describes the movement in LOS direction due to a deliberate tilt realignment introduced in device DBFm. Section 5.4 compares and analyzes the stability of the different devices on the site in terms of their ground motion. Section 5.4.1 further combines observations from different satellite geometries to quantify vertical and horizontal stability for DBF family of devices. Finally Section 5.5 compares the a-priori phase precision with the one obtained from observations.

Initial analysis based on a shorter data stack for select devices (MUTEs and conventional CRs) is provided in [58]. The results reported here are based on the analysis of larger data stacks (including the measurements recorded since the [58] report till 17th March 2018) from all available devices at the test site.

It must be noted that these results are obtained after specific data points from displacement results for pair CRDS-MUTE1 and CRDS-MUTE2 as measured from track t037 on 12th February 2017 are removed as outliers. Figure 5.1a shows this outlier marked with a cross for CRDS-MUTE1 displacement results. These outliers correspond to the corrupted phase response of descending CR CRDS due to accumulation of snow in its apex. Heavy snowfall was measured before the satellite acquisition epoch from KNMI weather station as mentioned in the previous Chapter. The RCS signal for this epoch was also dampened, indicating an influence on both the magnitude and phase of the reflected signal.

5.1. Estimation of deliberate and step movement

This section concerns the detection experiment of deliberate movement in RT MUTE-1. As mentioned in Section 3.3, a 7 ± 0.05 mm vertical movement is introduced in this RT on 7th March 2017. In order to test the accuracy of the InSAR results, the deliberate movement as observed from InSAR are tested against the actual movement introduced. The InSAR double-difference phase results are obtained in the reference of satellite geometry and thus these measurements express movements in LOS direction – as movements towards or away from satellite. These LOS measurements are projected in the vertical direction by scaling them with the cosine of the incidence angle involved assuming there is no horizontal movement involved [10].

These vertical displacement measurements are obtained for all device pairs and the time series obtained for pairs containing MUTE-1 device show a distinct jump corresponding to the specified epoch of deliberate movement – 7th March 2017. Interestingly, there is another secondary step encountered in the time series. Unlike the deliberate movement jump, this change in the time series is unexpected. This step corresponds to the abrupt jump in the RCS response of MUTE-1 that is reported in Section 4.4.4 and Figure 4.7. To clarify, these steps in phase and amplitude results are only observed for the first generation MUTE RT MUTE-1 (no step in second generation MUTE-2 results) and this change (in both phase and amplitude) is encountered at the same epoch – between 12th June 2017 and 15th June 2017 across all tracks. No changes are known to have occurred at the site during this period. Figure 5.1 shows two typical time series, in this case for pairs CRDS-MUTE1 and MUTE2-MUTE1 from Sentinel-1 descending track t037, demonstrating the deliberate movement and the step change as shifts in time series.

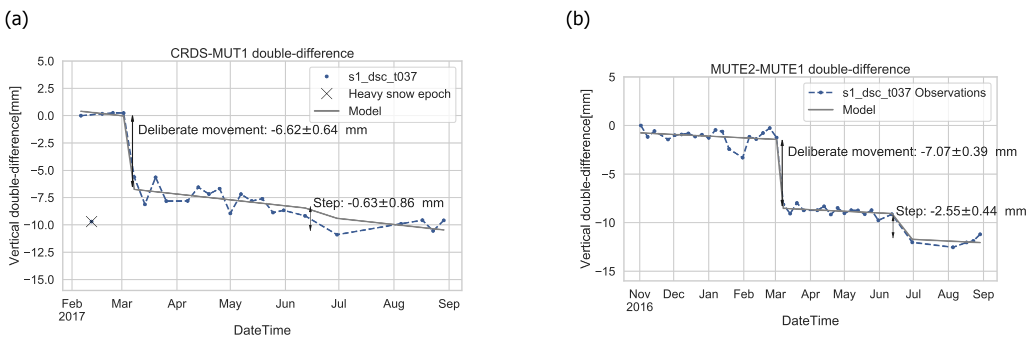

Figure 5.1: Vertical displacement time series for device pairs: a) CRDS-MUTE1 and b) MUTE2-MUTE1 as observed from Sentinel-1 descending track t037. For sub-figure(a), the measurement marked with a cross points out the phase response that corresponds to a heavy snowfall event (cumulative sum of snow measurement in last 24 hours of acquisition as measured from weather station exceeds more than 3 magnitude value) which is marked as an outlier and removed from the dataset. The observation time series are modelled as linearly changing with time along with a jump and a step which correspond to the deliberate movement and step in MUTE-1 RCS respectively. The grey line represents this model for both sub-figures. Deliberate movement and the step in the time series are distinctly observed and estimated at -6.62 ± 0.64 mm and -0.63 ± 0.86 mm respectively for CRDS-MUTE1 pair; while for MUTE2-MUTE1 pair the deliberate movement is estimated at -7.07 ± 0.39 mm and the step is estimated to be -2.55 ± 0.44 mm using least squares estimation.

Based on these vertical measurements, a least squares estimation is carried out to estimate the jump and the step in the time series. This estimated deliberate movement jump from InSAR data is compared with the true deliberate movement as shown in Figure 5.2. Estimates are presented for all device pairs containing MUTE-1, as observed from the four Sentinel-1 tracks. The error bar represents the standard errors of the parameter estimate. The deliberate movement observed from the InSAR agrees well with the actual movement. The only exception is the observation from ascending track t088 for device pair CRAS-MUTE1. This can be explained by the strong linear trend of the time series. The deliberate movement observed from InSAR in vertical direction is reported Table 5.1 along with its error. The difference between observed and actual movement is within range 0.01-0.69 mm. Thus, observations from InSAR can detect and quantify the abrupt changes in the vertical movements with an excellent accuracy and precision that are in the sub-millimeter range. Such movement detection can be carried out over a vegetation area using RTs and CRs as PSs.

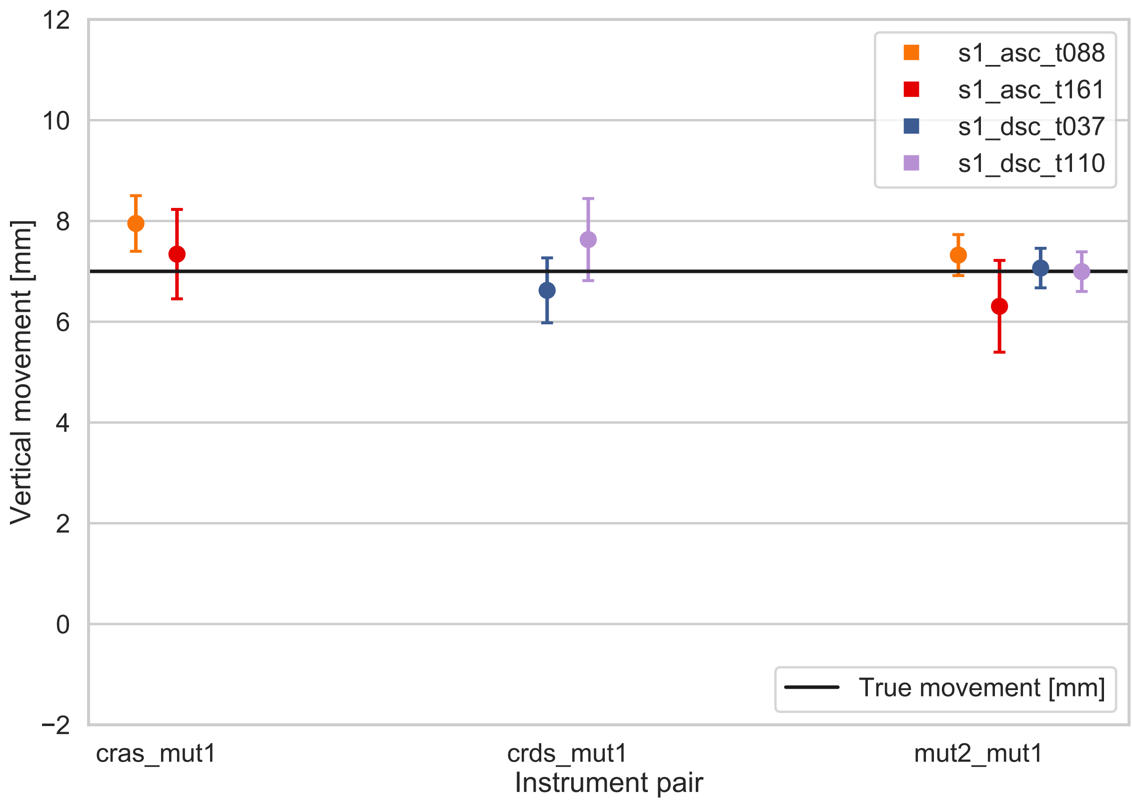

Figure 5.2: Comparison of deliberate movement estimated from InSAR data with the actual movement. These estimates are presented here for each pair of devices containing MUTE-1 from different tracks that are color coded as shown in the legend. Error bar represents the standard errors of the parameter estimate. The black line represents the actual movement of 7 ± 0.05 mm that was introduced deliberately on 7th March 2017. All estimates agree with the actual movement except for CRAS-MUTE1 pair estimate for ascending track t088.

The step movements estimated from different device pairs containing MUTE-1 are shown in Figure 5.3. Observations from track t161 around this epoch are not available and their estimates are not shown here. The error bar represents the standard errors of the parameter estimate. An average step movement of -1.44 mm is observed from these observations, shown in the figure by black line. The difference in the step movement is not statistically significant across different device pairs. Thus, the step movement is about equally strong for RT-RT pair as it is for CR-RT pairs. Since this movement is observed from four independent Sentinel-1 observations, it is unlikely that the step reflects a data-corruption in the satellite images. No significant movement in MUTE-1 device is observed from ground survey results around this epoch, thus ground movement can also be ruled out as a cause for this step. In Section 5.2.3, we consider the possibility of the influence of a sudden temperature change on the

Device Pair	Track	Estimated movement[mm]	Movement uncertainty[mm]	(Estimated movement - Actual movement)[mm]
mut2_mut1	s1_dsc_t110	6.99	0.39	0.01
mut2_mut1	s1_dsc_t037	7.07	0.39	0.07
mut2_mut1	s1_asc_t088	7.32	0.41	0.32
cras_mut1	s1_asc_t161	7.34	0.89	0.34
crds_mut1	s1_dsc_t037	6.62	0.64	0.38
crds_mut1	s1_dsc_t110	7.63	0.81	0.63
mut2_mut1	s1_asc_t161	6.31	0.91	0.69
cras_mut1	*s1_asc_t088*	*7.95*	*0.55*	*0.95*

Table 5.1: Deliberate movement along with its uncertainty as observed from vertical displacement InSAR data for different device pairs containing MUTE-1. The table is sorted by the absolute value of the difference between the actual movement and the movement estimated from different satellite tracks. The estimate from pair CRAS-MUTE1 from Sentinel-1 ascending track t088 is influenced by a strong linear trend in the time series and thus exhibits highest difference relative to the actual movement. With an exception of this observation, the difference between the deliberate movement estimate and actual movement is within 0.69 mm. The precision of values is in sub-millimeter range.

functioning of the RT device.

It must be noted that the change in MUTE-1 displacement results between 12th June 2017 and 15th June 2017 discussed here can also be seen as an artifact of an even steeper trend with a few outlier data points. However, for most amplitude and phase time series this change is abrupt, noticeably distinct and is thus treated as a step in the results. Except for the step estimated from CRDS-MUTE1 pair from track t037 (shown in Figure 5.1a), the uncertainties in slope estimates are reasonably small.

5.2. Comparison of InSAR and Ground survey results for MUTE RTs

The previous section focused on the comparison of InSAR results and ground survey measurements for the detection of single deliberate movement in the time series. This section compares the entire time series from the two approaches. Thus, the effect of deliberate movement is removed from the InSAR results before performing this comparison.

5.2.1. Comparison of results from different tracks

The comparison of InSAR vertical displacement time series with ground survey result is carried out for device pairs CR (CRAS CRDS)-MUTE1, CR (CRAS CRDS)-MUTE2 and MUTE2-MUTE1 since ground survey measurements are only carried out for CRs and MUTE RTs.

Comparison of vertical component projected from LOS

The vertical measurements are obtained by projecting the LOS observations in the vertical direction (assuming no horizontal movement) and accounting for the effects of the known deliberate movement in MUTE-1 RT. Across the different device groups, a good agreement within error bounds of one standard deviation is obtained between the vertical displacement signal obtained from InSAR and the levelling measurement signal (also expressed as vertical double-difference) for CR-MUTE2 pair. Figure 5.5a demonstrates this for descending track t037. For device pairs containing first generation MUTE-1 (both CR-MUTE1 pair and MUTE2-MUTE1 pair) there is a good initial agreement within error bounds between the two approaches, but these vertical displacement signals quickly diverge because of a trend (in addition to the step mentioned in Section 5.1) in the InSAR results. This linear trend is stronger in the measurements observed from ascending tracks and relatively weaker in the measurements observed from descending tracks (except for one time series). The magnitude of this trend for pairs involving MUTE-1 is reported in Table 5.2. For MUTE2-MUTE1 pairs, ground survey results are obtained as vertical displacement from both levelling and total station which are in good mutual agreement within error bounds (See Figure 5.5c and Figure 5.5d).

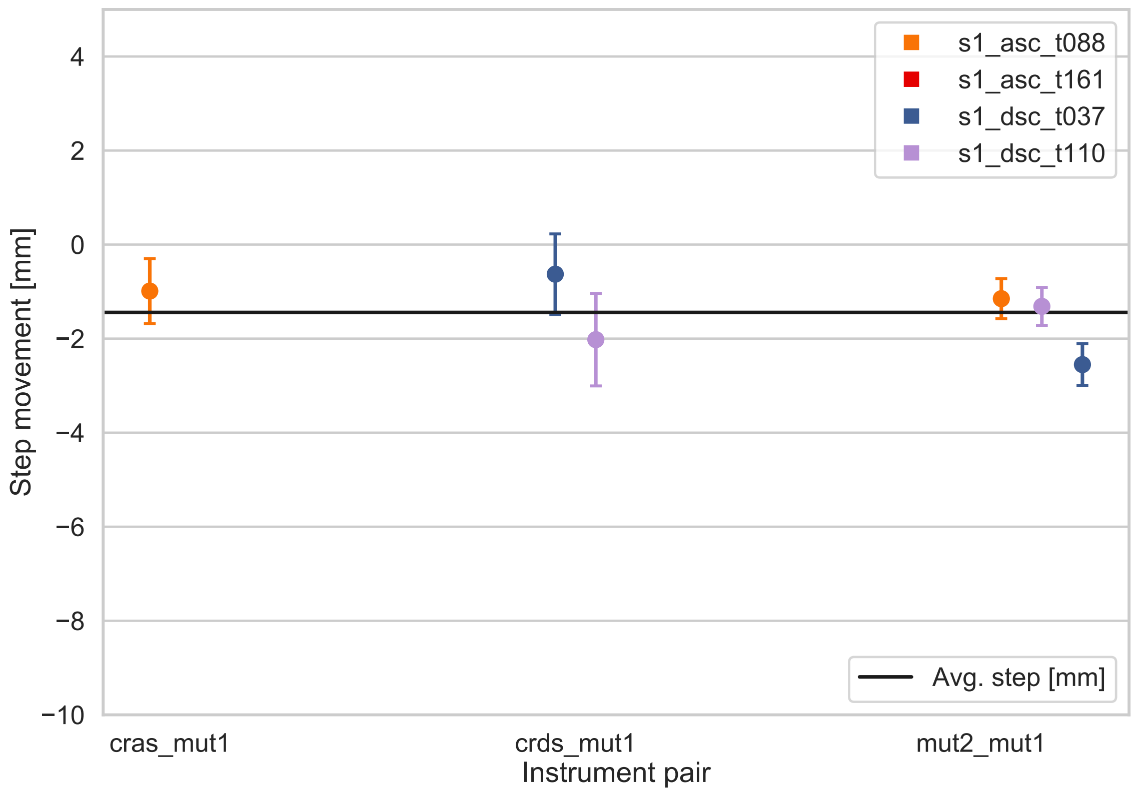

Figure 5.3: Step in the vertical displacement time series encountered between 12th June 2017 and 15th June 2017 for different device pairs containing MUTE-1. The estimates are provided for all tracks except Sentinel-1's ascending track t161, since no observation is available from that track during the epoch of step change. Error bar represents the standard errors of the parameter estimate. The black line represents the average step movement of -1.44 mm.

Device Pair	Track	Slope[mm/quarter]	Slope Error[mm/quarter]	DOF
mut2_mut1	s1_asc_t161	-2.411	0.731	14.0
crds_mut1	s1_dsc_t037	-1.593	0.621	20.0
mut2_mut1	s1_asc_t088	-1.406	0.27	41.0
cras_mut1	s1_asc_t088	-1.29	0.531	24.0
mut2_mut1	s1_dsc_t110	-1.054	0.277	35.0
mut2_mut1	s1_dsc_t037	-0.502	0.269	35.0
crds_mut1	s1_dsc_t110	-0.081	0.802	22.0
cras_mut1	*s1_asc_t161*	*0.666*	*3.109*	*4.0*

Table 5.2: Slope estimate along with its uncertainty obtained for vertical displacement InSAR data for device pairs involving MUTE-1. The table is sorted by slope magnitude. The estimate for pair CRAS-MUTE1 from track t161 is based on very few observations as shown by its degree of freedom. Thus, the estimate is erroneous in this case and is rejected. As for other pairs, the vertical displacement time series for pairs involving MUTE-1 show a linear trend of significant magnitude. The slope units are obtained in mm/quarter where 1 quarter is equivalent to 90 days.

Once, this trend along with the step in the time series is modelled and removed, then an excellent agreement within one standard deviation error bounds is obtained between the vertical displacement results from InSAR and ground survey results for all device pairs, including the ones involving MUTE-1 as well (Figure 5.6 shows this improvement in agreement relative to Figure 5.5). The question that emerges from this result is what causes linear trend in the time series and whether it can be justified to remove it. Because if this model adjustment step can be justified, then a complete agreement within one standard deviation error bounds is obtained between the InSAR and ground survey results for all device pairs observed from all four tracks of Sentinel-1.

For pairs involving MUTE-1, the ground survey results are stable. A significant vertical movement of several millimeters is not expected from MUTE-1. Thus ground-subsidence can be ruled out as a cause for this linear trend. Since the strength of the trend in the time series vary in descending and ascending tracks, it is possible that this trend is introduced due to the presence of a horizontal motion whose influence can vary across ascending and descending tracks due to differing satellite geometry. This motion could have resulted from actual ground motion or it might have resulted from the loose bolt which left MUTE-1 device with a capacity to turn horizontally under the influence of winds. In Section 5.2.2, we try to determine whether horizontal movements are responsible for the observed trend. It is also possible that the trend is introduced in the phase result due to influence of temperature on the functioning of the RT. Section 5.2.3 deals with this in more detail.

RT MUTE-2 in comparison shows a stable phase behavior, the displacement obtained for pair involving MUTE-2 show a good agreement with the ground survey results within error bounds. The behavior of this second generation MUTE RT device as a PS is identical to a CR, while the first generation MUTE-1 shows erratic behavior. Like step movement, the presence of linear trend in the phase results of pairs involving MUTE-1 device isn't expected. Although, the detection of the deliberate vertical movement for this device is excellent.

Comparison of LOS component

The comparison between InSAR and ground survey measurement has been carried out by converting InSAR measurements from satellite-geometry reference frame to ground survey reference frame. This comparison can also be carried out in the satellite reference frame by converting the ground survey measurements from vertical to LOS direction. This type of comparison has been carried out as well. However, the conversion of ground survey results from vertical direction to LOS, does not change the disparity between InSAR and ground survey results observed for pairs containing MUTE1 estimate. Hence, the conclusions drawn from such comparisons are identical to the one drawn from the former comparison in the ground survey reference frame, as reported in this section.

5.2.2. Comparison of results from multi-geometry estimate

In the previous sections, the vertical component for InSAR results is obtained as a projection of LOS assuming there is no horizontal movement. However, when such an assumption is not valid, it can

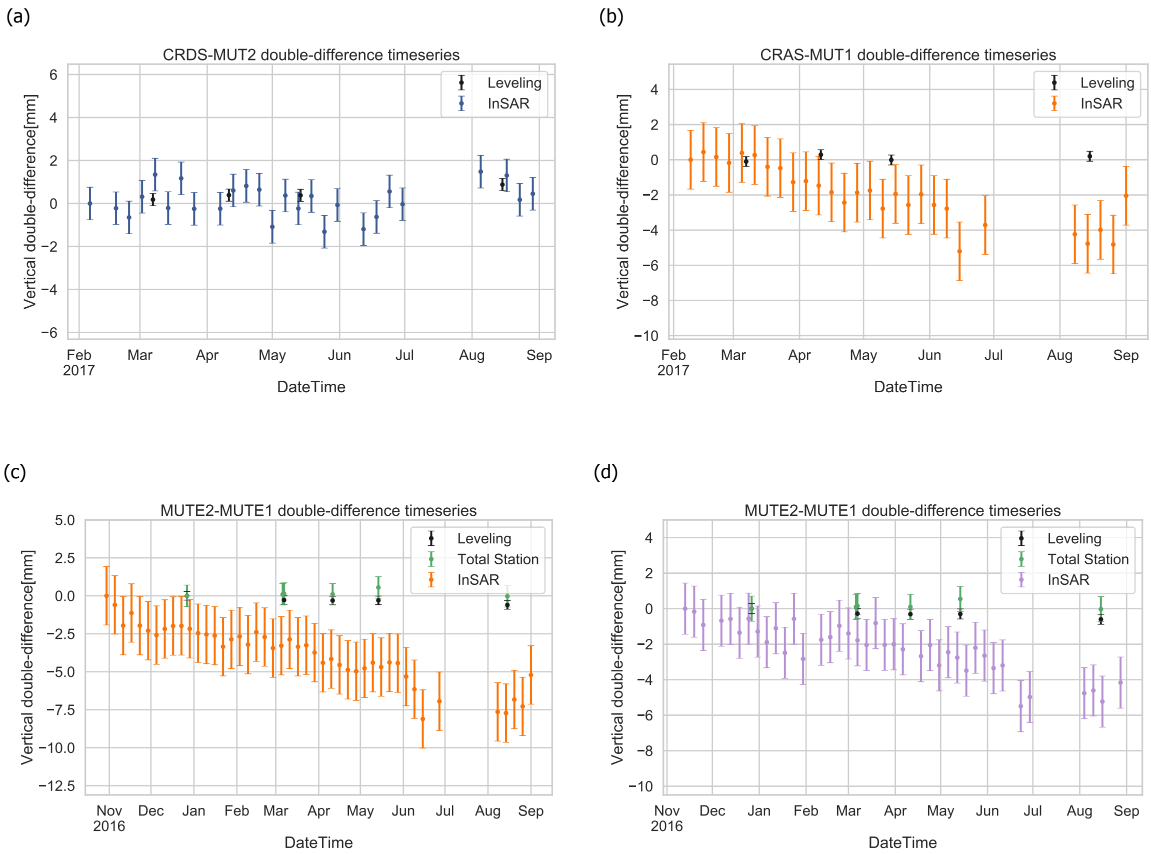

Figure 5.5: Comparison of vertical displacement time series observed from InSAR and ground survey techniques. The LOS measurement from InSAR are projected in the vertical direction (assuming no horizontal movements) to obtain vertical displacement. InSAR results are colored based on their track according to the color code shown in Figure 5.2 and Figure 5.3. Ground survey error bars represents the precision of the technique propagated to displacement and the InSAR error bars represents one standard deviation of values. The sub-figures show vertical displacement time series for (a) pair CRDS-MUTE2 as observed from descending track t037, (b) pair CRAS-MUTE1 observed from ascending track t088, (c) pair MUTE2-MUTE1 as observed from ascending track t088 and (d) pair MUTE2-MUTE1 as observed from descending track t110. Sub-figure (a) shows that a good agreement is obtained between InSAR and levelling techniques for CR-MUTE2 pairs. For device pairs containing MUTE-1 (Figure 5.5b, Figure 5.5c and Figure 5.5d), the two results quickly diverge because of the trend and the step present in the InSAR results. This trend is stronger for measurements observed from ascending tracks (Figure 5.5c) as compared to the trend observed in descending track (Figure 5.5d).

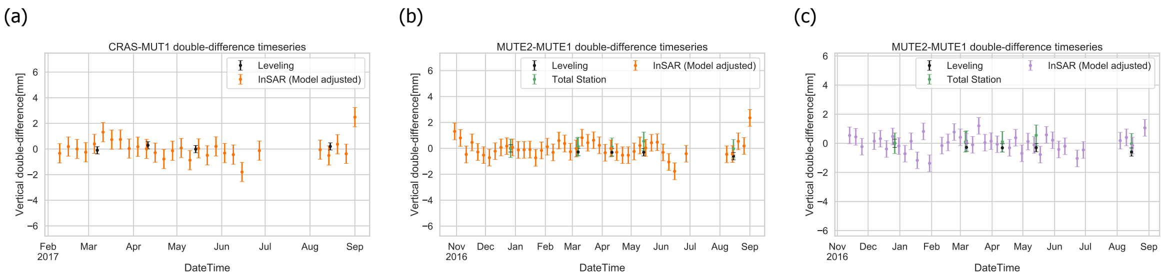

Figure 5.6: Comparison of vertical displacement time series between model-adjusted InSAR result and ground survey measurements. The trend and step from the vertical displacement time series is modelled and removed. Ground survey error bars represents the precision of the displacement and the InSAR error bars represents one standard deviation of values. The sub-figures show model-adjusted vertical displacement time series for (a) pair CRAS-MUTE1 observed from ascending track t088, (b) pair MUTE2-MUTE1 as observed from ascending track t088 and (c) pair MUTE2-MUTE1 as observed from descending track t110. Figure 5.6a, Figure 5.6b and Figure 5.6c correspond to the Figure 5.5b, Figure 5.5c and Figure 5.5d respectively after removing trend and step from the time series. The agreement between the two technique is improved once the InSAR results are model-adjusted.

lead to errors in the vertical measurements depending on the magnitude of horizontal movement and the incidence angle involved [69]. In this section, InSAR results are obtained as 3-D components by utilizing data from ascending and descending tracks. The time series used for this computation contains the trend and step behavior and is not corrected for temperature effects yet. The vertical component obtained from such multi-geometry fusion is then obtained by accounting for the horizontal motion. This approach is utilized to determine if by accounting for horizontal motion, the trend in the vertical displacement time series can be explained.

Comparison of vertical component from 3 component estimation

The InSAR data utilized in this study is obtained regularly form four Sentinel-1 tracks, except for a period from October 2016 till March 2017, when data from ascending track t161 is not available. Hence, over this time period the estimation is carried out with the other three remaining tracks. In addition, this estimation does not cover the period between July and August 2017, when the MUTE RTs were turned off, but it does cover the period from 3rd August 2017 to 4th September 2017 when MUTEs are operational again.

To estimate 3-D components from different viewing geometries requires data from same point in space and time. Thus, the time series from different tracks are resampled using linear interpolation to obtain daily observations assuming steady-state motion. The relation between interpolated LOS observations and its three directional components can be expressed using the model [69, 70]:

$$\begin{bmatrix} d_{LOS}^{ASC1} \\ d_{LOS}^{ASC2} \\ d_{LOS}^{DSC1} \\ d_{LOS}^{DSC2} \end{bmatrix} = \begin{bmatrix} \cos\theta^{ASC1} & \sin\alpha^{ASC1}\sin\theta^{ASC1} & -\cos\alpha^{ASC1}\sin\theta^{ASC1} \\ \cos\theta^{ASC2} & \sin\alpha^{ASC2}\sin\theta^{ASC2} & -\cos\alpha^{ASC2}\sin\theta^{ASC2} \\ \cos\theta^{DSC1} & \sin\alpha^{DSC1}\sin\theta^{DSC1} & -\cos\alpha^{DSC1}\sin\theta^{DSC1} \\ \cos\theta^{DSC2} & \sin\alpha^{DSC2}\sin\theta^{DSC2} & -\cos\alpha^{DSC2}\sin\theta^{DSC2} \end{bmatrix} \begin{bmatrix} D_U \\ D_N \\ D_E \end{bmatrix}, \tag{5.1}$$

where d_{LOS} denotes the LOS observations observed from four different track geometries, where θ and α represent the incidence and heading angle of the satellite in each track respectively while D_U, D_N D_E are the unknown vertical, east-west and north-south parameters estimated using the method of least squares. The degree to which a SAR sensor can pick up movements in each directional component depends on its inclination and heading towards the target. Study by [71] shows how polar orbiting satellite such as Sentinel-1 are most sensitive to movements in vertical direction (80%) followed by sensitivity in the east-west (60%) and north-south direction (11%).

This result is obtained for CR and MUTE RT pairs where ground survey results are also available, and a comparison can be carried out with its vertical component estimate. It should be noted that to carry out multi-geometry fusion for CR-MUTE pairs, data from CRAS is utilized for ascending pairs and CRDS for descending pairs. Although they are separate PSs in the field, it is assumed that their phase results can be combined due to their location vicinity.

Figure 5.8 shows such comparison for CR-MUTE2 and MUTE2-MUTE1 pair. The vertical displacement estimated from multiple tracks of Sentinel-1 is represented as a time series with a shaded stripe covering standard errors of this parameter estimate. The ground survey results are shown here as error bars representing the displacement precision. A significantly lower precision of InSAR estimate renders them relatively tiny in this figure. Results obtained from these two approaches agree with each other within error bounds when the estimates are obtained from all four tracks. For the period between the end of May 2017 and early August 2017, the unavailability of data from ascending track t161 leads to the estimation of three parameters based on observations from three tracks. Such an estimate obtained from zero degrees of freedom is unreliable and does not agree with the ground survey results. Subsequent results show this unreliability from 3 track estimate for other components. For CR-MUTE pairs, this covers a significant part of the time series (see Figure 5.8a). A jump of around 2.5 mm is encountered in the MUTE2-MUTE1 vertical displacement estimate at the beginning of the time series (see Figure 5.8b). No ground motion is expected corresponding to this epoch. In addition, this jump is only observed in MUTE2-MUTE1 pair results but not for CR-MUTE1 pair results. Thus, this jump is assigned to an error in the estimation procedure that falsely attributes a motion to the vertical component rather than any actual ground movement.

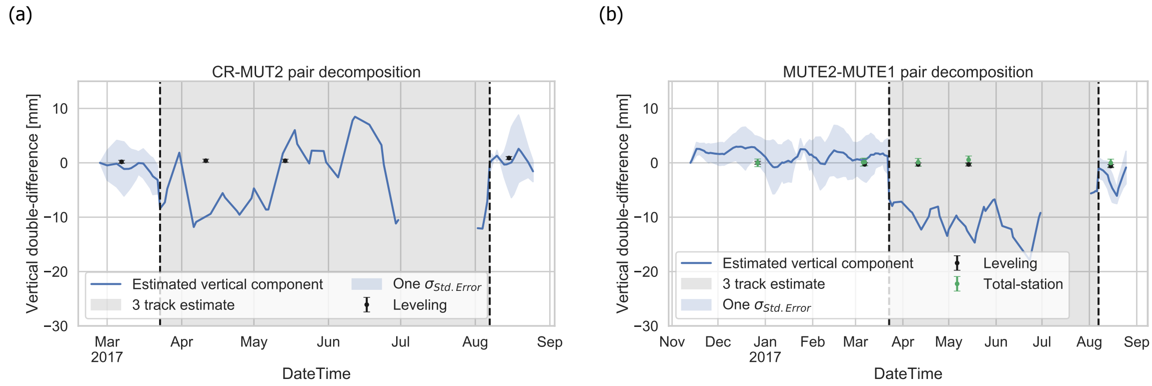

Figure 5.8: Comparison of vertical displacement time series observed from combination of multi-geometry InSAR and ground survey techniques. The vertical Up-Down component estimate along with its standard error is represented here as the blue time series with its shaded stripe. Gray shaded region marks the period during which this estimation has been carried out with only 3 tracks. Ground survey error bars represents the displacement precision. The sub-figures show vertical displacement time series for (a) pair CR-MUTE2 and (b) MUTE2-MUTE1. The estimate obtained from just 3 tracks seems unreliable. During this period a good agreement between InSAR and ground survey results is not obtained. However, over the remaining period, the results from the techniques are in mutual agreement within error bounds. An unexpected jump of about 2.5 mm is observed in the MUTE2-MUTE1 pair's vertical estimate. It is likely that this corresponds to an error in the estimation rather than any actual ground motion.

Comparison of horizontal components from 3 component estimation

Ground survey carried out with total station device measures 3D movements of MUTE devices. Levelling survey provides measurements in the horizontal direction in terms of the tilt of the MUTE concrete pads. Thus, in addition to the comparison of the vertical component, a comparison of the horizontal component is also carried out between the ground survey measurements and multi-geometry InSAR estimate for MUTE2-MUTE1 pair. It must be noted that the total station measurements are converted so that eastward movement is positive. This convention is followed by the InSAR and levelling results shown here.

Figure 5.9 shows this comparison of the horizontal displacement for MUTE RT pairs in the East-West direction. The time series with its shaded stripe represents the East-West component estimate and the standard error of this estimate as obtained from combination of multiple tracks of Sentinel-1. The error bars of ground survey results are obtained after propagating the precision of the technique to displacements. Like the previous result, the estimate obtained in the gray shaded region from three track estimate isn't reliable. Hence, the disagreement between InSAR and ground survey results over this period. However, when the estimates are obtained from four tracks, results from all the techniques are in good mutual agreement within error bounds. A small positive trend in present in the InSAR displacement estimate for this component with a magnitude of about 2 mm near the end of the operational period (that is also observed in the ground survey displacement results). A positive MUTE2-MUTE1 East-West displacement suggests that relative to MUTE-1, MUTE-2 has moved in the east direction. This result supports the interpretation drawn from ground survey results for individual devices as discussed in Chapter 3, where an eastward motion of in MUTE-2 is reported due to the tilt in the concrete pad and a westward motion is detected in MUTE-1.

Obtaining vertical component of InSAR result from multi-geometry estimation rather than as a projection from LOS diminishes the linear trend observed in displacement time series involving MUTE-1 and leads to a better agreement with ground survey results. This can be observed for MUTE2-MUTE1 pair by comparing Figure 5.5b and Figure 5.5c with Figure 5.8b.

This is also true for the East-West component obtained from such an estimation that also exhibits a good agreement with the ground survey measurements. However, the vertical signal obtained from

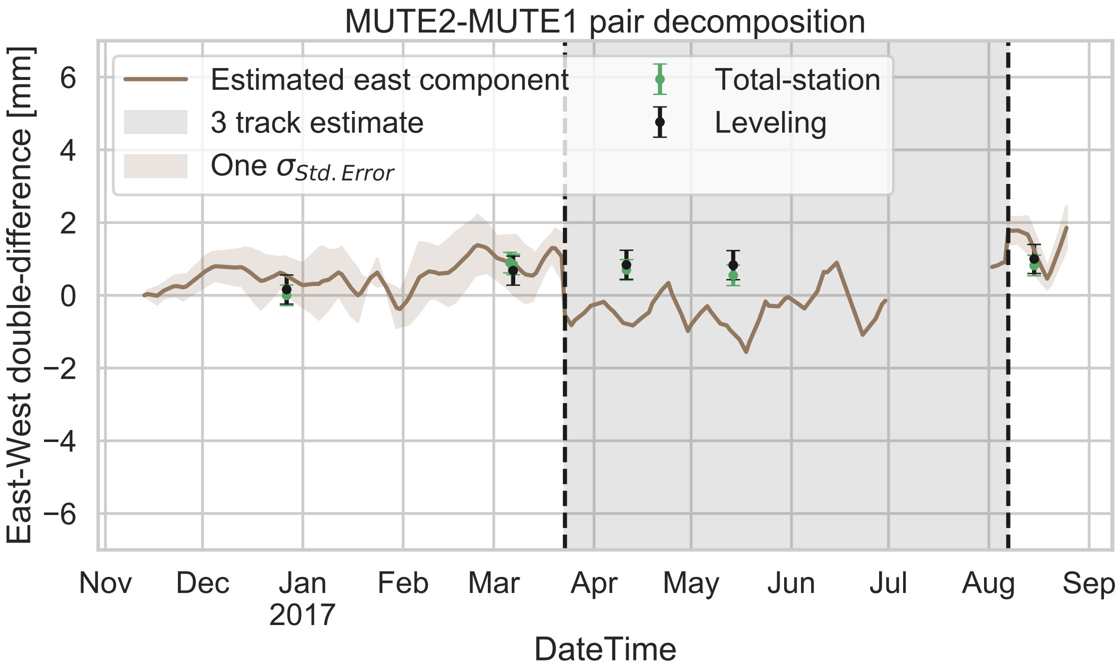

Figure 5.9: Comparison of horizontal displacement time series (East-West component) observed from combination of multi-geometry InSAR and ground survey techniques. The horizontal East-West component estimate along with its standard error is represented here as a brown time series with its shaded stripe. Gray shaded region marks the period during which this estimation has been carried out with only 3 tracks. Ground survey error bars represents the precision of its displacement. The figure shows this horizontal displacement time series for MUTE2-MUTE1 pair. Similar to previous result, the estimate from 3 tracks seems unreliable where ground survey and InSAR techniques do not agree. However, over the rest of the period, the results from different techniques are in good agreement with each other. This InSAR result supports the interpretation from ground survey measurements that RT MUTE2 is gradually moving eastwards.

such multi-geometry estimation attributes an unrealistically high magnitude to the North-South component. This can be observed from Figure 5.10 which shows the different estimated components for the device pairs involved. The North-South component estimate is significantly higher than other components across all the different device pairs.

As mentioned previously, sensitivity of S1 measurements for North-South displacement is much weaker because of the satellite geometry formed by polar-orbiting SAR sensors. From such a geometry, a good variation of satellite position in the East-West direction is obtained from different tracks, however the variation of positions in the North-South direction is very small. Thus, displacements in the North-South directions are poorly constrained even with multiple-geometry dataset [69].

Thus, a less reliable estimate can be expected for the North-South component. However, in our case, this component is an order of magnitude higher than the estimates of other components. This signal is unrealistic and does not correspond to any actual horizontal ground motion in this direction. Thus, the result of vertical component estimates that attributes such an unusual signal to the North-South component cannot be used reliably to conclude that the horizontal movement is responsible for the trend observed in the displacement results for pairs involving MUTE-1. Since the estimate of North-South component does not aid the interpretation of ground movement, a modified multi-geometry fusion is considered that neglects this component.

Recent studies regarding multi-geometry fusion recommend ignoring North-South component from linear system of equations [69, 71]. Additionally, removing the North-South component will increase the degree of freedom which will be valuable for time period covering the three-track estimate since two parameter estimation can now be obtained reliably from three observations. Ignoring the North-South component from parameter estimation also improves the conditionality of the linear system of equations [69]. The subsequent section discusses the result from this modified multi-geometry estimation. These results are also compared with the ground survey results and used as a basis to test if the horizontal movements are responsible for the trend observed in the vertical displacement time series in device pairs containing MUTE-1.

Comparison of horizontal and vertical component from 2 component estimation

This section concerns the results obtained from modified multi-geometry combination of InSAR. Data from ascending and descending tracks is combined by utilizing the satellite geometry to estimate vertical and East-West component, deliberately ignoring the North-South component. For this section, displacement in the North-South directional component are assumed negligible. The estimates of other components are compared with the ground survey results.

Figure 5.12 shows a comparison between the results from modified multi-geometry InSAR and ground survey technique. For the East-West component, an excellent agreement within error bounds is obtained between InSAR and ground survey results throughout the entire period. Unlike the results from 3-component estimate, this approach is able to provide reliable results even for estimation that carried by only 3 tracks, shown in the figure by the gray shaded region (see Figure 5.9 and Figure 5.12a). Like the results from 3-component estimation, these results support the interpretation derived independently from ground survey results in Chapter 3 that MUTE-2 exhibits a movement towards the east and MUTE-1 towards the west. On the other hand, the vertical component displacement result obtained using this approach is very similar to the vertical component result obtained by projecting LOS in the vertical direction (see Figure 5.5c, Figure 5.5d and Figure 5.12b).

In both approaches, presence of a strong linear trend in the InSAR results for pairs involving MUTE-1 leads to a disagreement between InSAR and ground survey techniques. Likewise, this trend is not observed for vertical CR-MUTE2 displacement results for both approaches. This can be observed from Table 5.3 which reports the magnitude of the linear trend obtained for the vertical estimate using the modified multi-geometry combination.

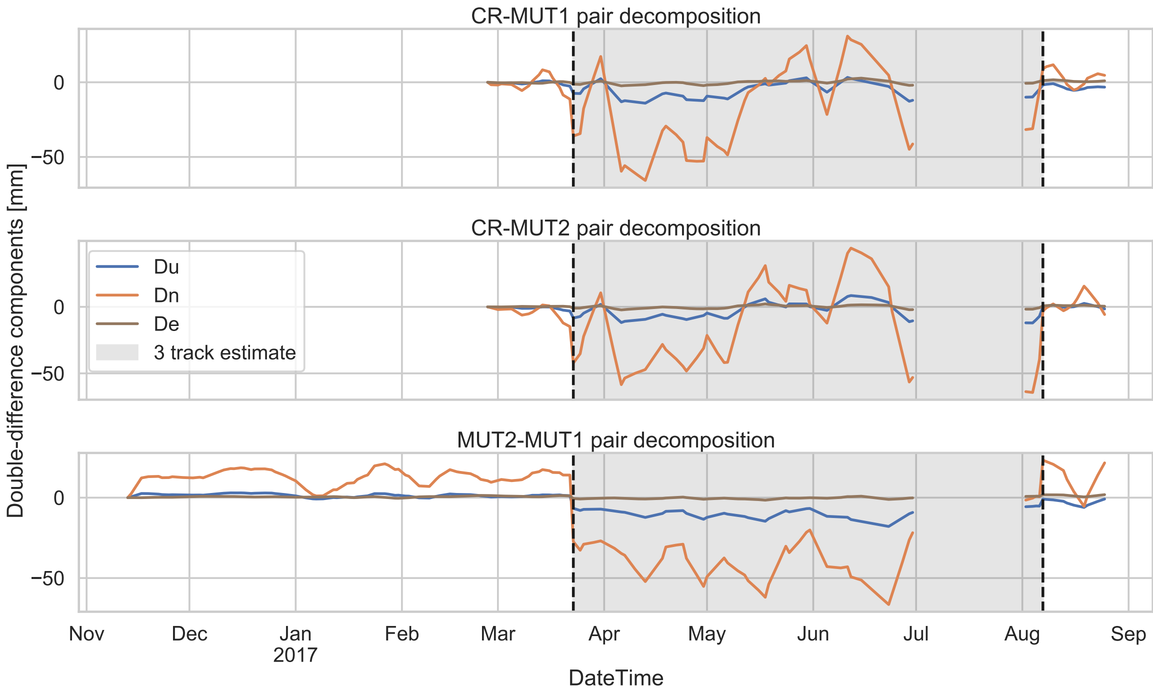

Figure 5.10: Comparison of North-South component displacement estimate with other components across different device pairs. The least squares estimation of components is carried out by combining multi-geometry InSAR using satellite geometry. The three subfigures show the estimation result for different device pairs. Gray shaded region marks the period during which this estimation has been carried out with only 3 tracks. The North-South component estimate (Dn) is an order of magnitude higher than vertical (Du) and East-West component (De). Such high magnitude is unrealistic and results from a poor constraint in the North-South direction which is a consequence of satellite geometry.

This approach of modified multi-geometry estimate accurately estimates displacement in the East-West direction throughout the observation period. However, accounting for this horizontal movement is not able to explain the trend in the vertical displacement time series observed for results of device pairs involving MUTE-1. Based on this result, the role of horizontal movement can be rejected as a cause for the trend observed in the vertical MUTE-1 time series.

Similar to the approach where vertical component result is obtained as a projection of LOS, the agreement between the InSAR results and ground survey measurement is obtained for all device pairs involving MUTE-1 once this trend in the time series is removed. This can be observed from Figure 5.14 which shows results after the trend in the estimated vertical component displacement time series is modelled linearly and removed. To clarify, this is a single trend obtained for results after fusing data from multiple tracks. Although, applying model-adjustment (or removing the linear trend) only makes sense for the vertical component. For the East-West displacement results, modelling and removing the trend in the signal deteriorates the agreement between the InSAR and ground survey techniques (compare Figure 5.12a and Figure 5.14a). Removing linear trend is unnecessary in this case.

Based on the results obtained from this section, accounting for horizontal movement is not able to explain the trend in the displacement component. This trend is only observed for device pairs involving MUTE-1 and it only affects the measurement of vertical component.

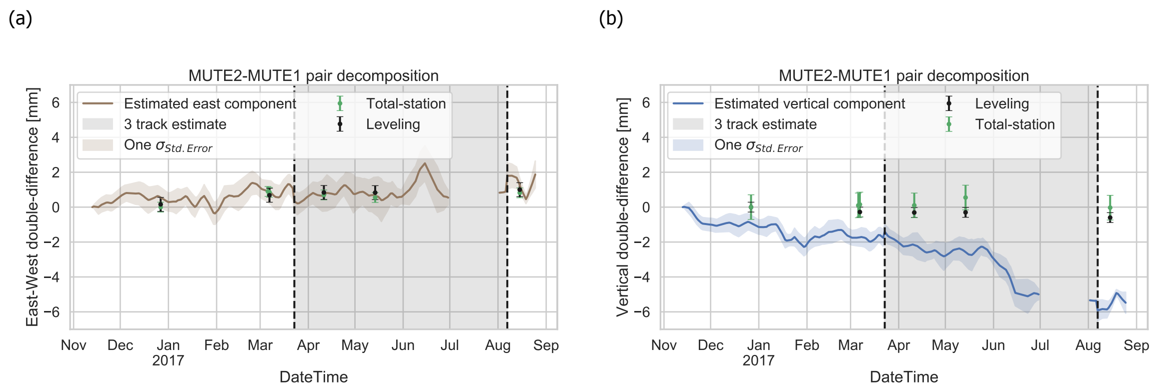

Figure 5.12: Comparison of vertical and horizontal (East-West) displacement time series obtained from modified multi-geometry InSAR and ground survey results. Observations from multiple tracks of InSAR are utilized along with satellite geometry to estimate two components using least-squares by ignoring the North-South component. The gray shaded region marks the period during which the estimation has been carried out with only three tracks. The sub-figures show displacement time series for (a) East-West component for MUTE2-MUTE1 pair depicted here with the brown time series with its shaded stripe representing the standard error and (b) vertical component for MUTE2-MUTE1 pair shown here as a blue time series with its shaded stripe representing the standard error of this parameter estimate. Ground survey results are represented by error bars in both sub-figures which represents the double-difference result with its precision. Excellent agreement within error bounds is obtained between the InSAR and ground survey techniques for East-West components, even for estimates that are based on three tracks (fewer observations). This shows that unlike the results from 3 component estimate, these results are reliable for three track estimates. The vertical component estimate result is similar to the measurements obtained by projection of LOS to vertical; i.e. for device pairs containing MUTE1, presence of a strong linear trend leads to a disagreement with ground survey results.

5.2.3. Comparison of results after temperature correction

The operation of MUTE RTs covers the period from November 2016 to late-August 2017. During this time period, the temperature sampled for SAR acquisition epochs increases with time. Laboratory experiments carried out by SPENG demonstrate that the performance of the RTs can be sensitive to the temperature of the environment they operate in. However, no sudden temperature changes are observed between 12th-15th June 2017 and thus influence of temperature on performance does not explain the abrupt step observed in the RCS and phase response of MUTE-1. This step in phase results is not removed for the analysis of time series carried out here. This section explores whether the linear

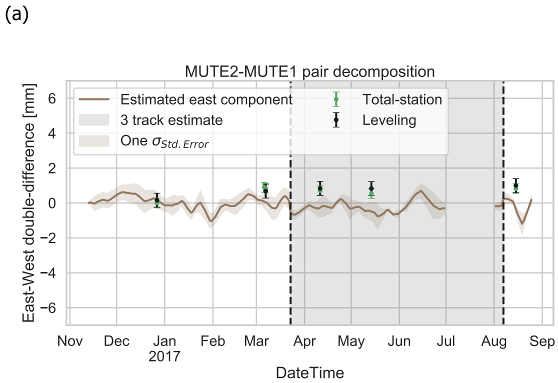

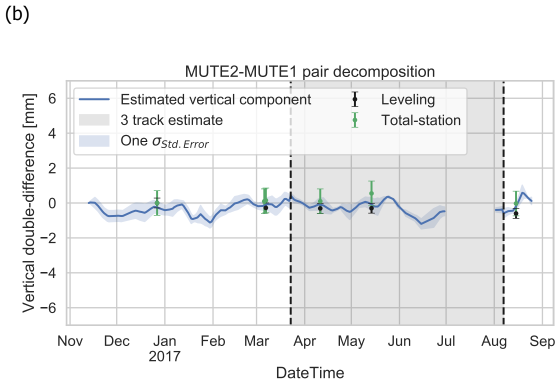

Figure 5.14: Comparison of vertical and horizontal (East-West) displacement time series obtained from model-adjusted modified multi-geometry InSAR and ground survey results. The trends in the vertical and horizontal displacement time series shown in Figure 5.12 are modelled linearly and removed. The gray shaded region marks the period during which the estimation has been carried out with only three tracks. The sub-figures show displacement time series for (a) model-adjusted East-West component for MUTE2-MUTE1 pair depicted here with the brown time series with its shaded stripe representing the standard error and (b) model-adjusted vertical component for MUTE2-MUTE1 pair shown here as a blue time series with its shaded stripe representing the standard error of this parameter estimate. Ground survey results are represented by error bars in both sub-figures which represents the double-difference result with its precision. Removing the linear trend from the vertical component of the displacement time series leads to an agreement within error bounds between the result obtained by InSAR and ground survey techniques. However, model-adjustment worsens the agreement obtained between these techniques for East-West displacement component. Thus, removal of the linear trend only makes sense for the vertical component.

Device Pair	**Slope[mm/quarter]**	**Slope Error[mm/quarter]**	**DOF**
CR-MUT1	-2.303	0.055	179.0
MUTE2-MUTE1	-1.698	0.038	284.0
CR-MUT2	0.139	0.04	179.0

Table 5.3: Linear slope estimate along with its uncertainty as obtained for vertical displacement component estimated using modified multi-geometry InSAR. The table is sorted by slope magnitude. Since the time series for pair CR-MUTE2 is stable, the slope magnitude is negligible in this case. For device pairs involving MUTE-1, the magnitude of slope estimate is significant and comparable to the slope results reported in Table 5.2. Thus, accounting for horizontal movement by combining the data from ascending and descending track does not remove the trend from the time series that is observed for pairs involving MUTE-1. The slope units are obtained in mm/quarter where 1 quarter is equivalent to 90 days.

trend observed in the vertical displacement component for pairs involving MUTE-1 is caused due to the influence of linearly increasing temperature on phase response of first generation MUTE device.

In Chapter 4, the laboratory results are reported that show the observed relation of the changing RCS under wide range of temperature values. Figure 5.15 shows this relation for phase responses in millimeters. As mentioned in Section 4.4.5, this relation is used to interpolate correction factors to account for the influence of temperature.

To account for this effect, temperature correction is applied by subtracting the correction factors obtained for phase (based on the temperature value for that epoch) from the observed phase values. The decision of subtracting the phase correction factors rather than adding them to the observations is based on the operation which improves the RMSE of the curve-fitting procedure. Phase temperature correction is carried out for only MUTE RTs and the performance of CRs is independent of the temperature conditions. The displacement results reported for pairs involving MUTE RTs in this section are based on such temperature corrected phase values.

The effect of applying the temperature correction to phase has a negligible effect on the displacement results. This change is not significant enough to account for the trend observed in the results for devices pairs containing MUTE-1 RT. This is observed universally irrespective of the method used to obtain the vertical displacement, be it through projection of LOS, multi-geometry fusion or modified multi-geometry fusion ignoring the North-South component.

It is possible that the temperature correction provided for MUTE-1 is not able to account for the higher sensitivity of this first generation device to temperature. Perhaps, phase results for this RT depend more significantly on the seasonal temperature variation than as determined from the laboratory by SPENG. If this assumption is true, then the model correction involving the removal of trend from vertical displacement time series for pairs involving MUTE-1 acts as a temperature correction step and can be justified to demonstrate the agreement between InSAR and ground survey results. Although, it is a potential possibility, it should be noted that there is no evidence to support this statement.

The disagreement between the InSAR and ground survey results observed for pairs involving MUTE-1 is quantified by taking the difference between the results obtained by the two techniques. Since temperature rises steadily as the InSAR vertical displacement deviates linearly over the course of the experiment, the correlation between the disagreement of two the techniques and the temperature is high for MUTE2-MUTE1 pair results observed from ascending tracks. This can be observed from Table 5.4 which reports these correlations. For device pairs involving MUTE RTs this correlation is obtained for both levelling and total station measurements. The correlation between temperature and disagreement in techniques for CR-MUTE-1 from track t161 is rejected since this is obtained from fewer data points. The correlation coefficients are reported here not to imply a causation between temperature and the disagreement, but rather to point out that the potential cause of disagreement between the techniques is complicated by temperature and time. The linear trend and the step in the displacement time series involving MUTE-1 could also be an indication of a device malfunction. Perhaps, the electrical performance of the MUTE-1 radar transponder degrades with time in a linear fashion. This would lead to a high correlation value of the disagreement between the two techniques with time. And since the temperature, generally speaking, increases steadily with time (for the MUTE operational time period), it would also lead a high correlation value with temperature as well. Thus, because of the time period of the experiment covers the period from winter to summer, it is difficult to disentangle the potential influence of temperature and device malfunction.

The fact that MUTE-2 does not show this trend/step behavior points to a device defect specific to the first generation MUTE RT. Based on the results shown in this Chapter and the last, the linear trend and the step result in the time series is observed for both the vertical displacement and the RCS signal for MUTE-1. Therefore, it is argued here that for RTs RCS acts as a marker or an index that provides a measure for the electrical performance of the device. When the signal of the device transmitted to satellite is affected by an external factor then it affects both the magnitude and phase of the signal.

For instance, the introduction of this Chapter begins by describing the corruption of the transmitted signal to the satellite due to the accumulation of snow in the apex of the CR. This change in the signal was identified in both the phase (displacement time series) and the magnitude (RCS time series) of the result (see Figure 5.1a and Figure 4.10b). Therefore analysis of RCS for CRs helps interpretation of phase anomalies caused by accumulation of excess rainwater or snow.

The conclusion drawn from the results in this section is that displacement results obtained from InSAR and ground survey results for RTs and CRs agree with each other. For device pairs involving MUTE-1, this agreement is obtained after applying a model correction that accounts for the linear trend and the step in the time series. This model adjustment is justified by the argument that the trend and step behavior correspond to a potential device malfunction in the functioning of this first generation MUTE RT. Alternatively, it is also possible that this behavior results from an influence of the temperature on the functioning of this device. However, for this argument to be true, it must be assumed that the laboratory tests conducted are not able to adequately capture the sensitivity of the first generation MUTE to temperature changes.

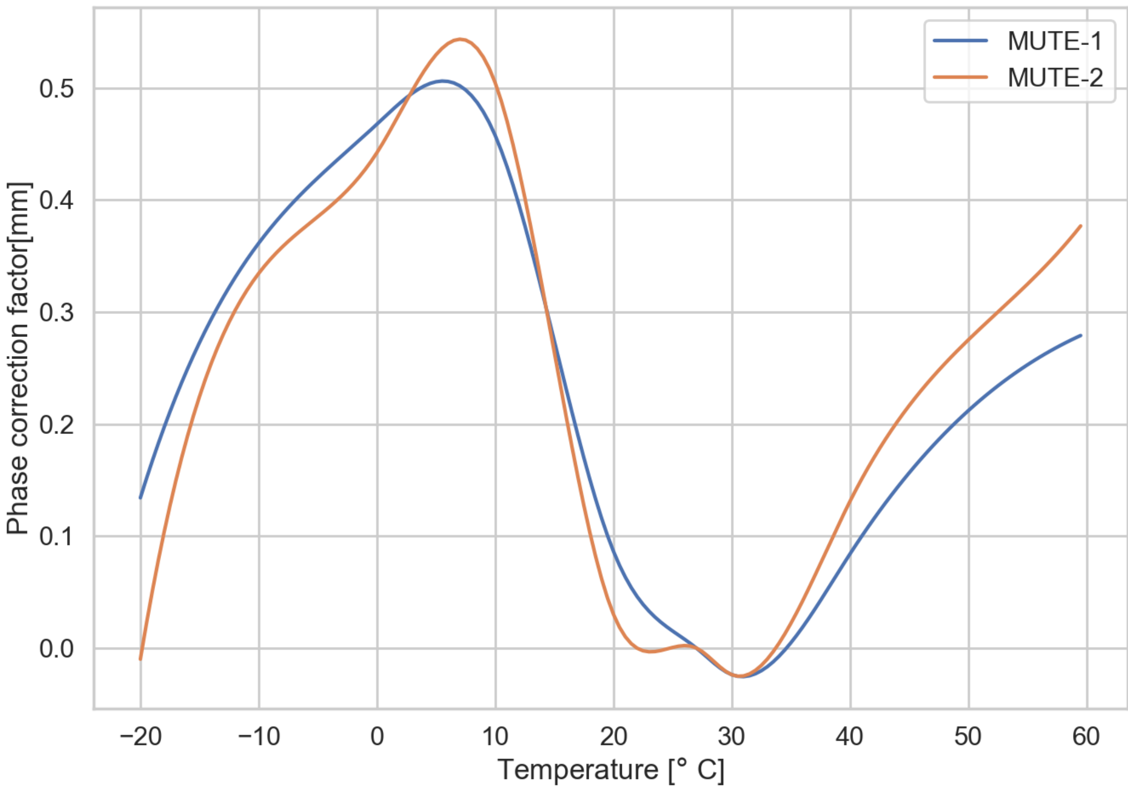

Figure 5.15: Temperature correction factors provided as delta millimeters over a range of temperature values. The curves in the figures are obtained for MUTEs after linearly interpolating a set of correction factors recorded against temperature for phase (from a laboratory experiment carried out by SPENG). The units of these correction factors are changed from degrees to millimeters. The magnitude of these correction factors are not significant enough for temperature correction step to account for the trend in the displacement results for device pairs involving MUTE-1.

5.3. Estimation of tilt movement in DBFm

Wassenaar site is under use for several other InSAR experiments. The device family of DBF and ECR as used for these purposes. An experiment conducted for another project at the same test site involved introducing a deliberate tilt (planned:$6.5°$, realized:$6.4°$) in the CR DBFm. This device is referred to as a "mockup" of double backflip CRs in [9]. Other changes have also been introduced in the DBFm mockup but this section centers around the discussion of the deliberate tilt introduced on 19th August

Device Pair	Track	CC (Lvl-InSAR)	CC (Tst-InSAR)
cras-mut1	*s1_asc_t161*	*0.99*	-
mut2-mut1	s1_asc_t161	0.82	0.83
mut2-mut1	s1_asc_t088	0.72	0.77
cras-mut1	s1_asc_t088	0.66	-
cras-mut2	s1_asc_t161	0.64	-
crds-mut1	s1_dsc_t037	0.63	-
mut2-mut1	s1_dsc_t110	0.54	0.62
mut2-mut1	s1_dsc_t037	0.44	0.57
crds-mut2	s1_dsc_t037	0.42	-
crds-mut1	s1_dsc_t110	0.27	-
cras-mut2	s1_asc_t088	0.11	-
crds-mut2	s1_dsc_t110	-0.31	-

Table 5.4: Correlation coefficient between temperature measured at the acquisition epoch and the disagreement between the results obtained from InSAR and ground survey techniques. This disagreement is quantified as a difference in the vertical displacement signal obtained from the two techniques. For device pairs involving MUTE RTs, this vertical signal is obtained from both levelling and total station (abbreviated here as 'Lvl' and 'Tst' respectively). Thus, the correlation is obtained for both levelling-InSAR difference and total station-InSAR difference, unlike pairs involving CRs, where only levelling measurements are available. The correlation coefficient obtained for pair CRAS-MUTE1 from track t161 is obtained from only three data-points. This result is therefore rejected. For device pairs involving MUTE-1, a significant correlation is obtained for observations in ascending pairs. There is no significant correlation with temperature for CR-MUTE2 pairs.

2017. See Appendix A for a detailed description of the change in the geometry of the device after applying this change and how the magnitude of this deliberate tilt is determined.

Although this experiment is outside the scope of this study, the introduction of the deliberate tilt influences the results mentioned in the current report and subsequently the interpretation of these results for ground-movement. For instance, a movement of 5 mm is expected to be observed from ascending track t088 for DBFm while observations from track t161 are expected to move by 0.8 mm in LOS direction[63]. Thus, changes in results observed because of introducing such deliberate tilt are pointed out in this study. For a more detailed discussion of these experiments related to the design of the Integrated Geodetic Reference Station, the reader is referred to [9].

DBFm is double backflip corner reflector with a novel design [8] that has two distinct orthogonal internal-reflection surfaces. These separate but co-located pair of phase center provide freedom to align them independently towards both the ascending and descending pass of satellite using a single device. As described in Section 4.4.6, the orthogonal reflection-surface that is pointed towards the average ascending pass is deliberately tilted towards the direction of track t161 to reduce its misalignment. This increases the misalignment for track t088 as boresight is now aligned farther away from its ideal direction than before (by about $8°$). Thus, the impact of this effect is observed as a change in InSAR measurements from ascending tracks while the results from descending tracks remain unaffected because the boresight of the descending half of the device is aligned correctly in the intended direction. This misalignment in ascending track is confirmed with the dampening of the RCS for the corresponding epochs (see Figure 4.14).

The LOS displacement measurements CRAS-DBFm obtained from ascending tracks, as depicted in Figure 5.17 shows a distinct movement corresponding to the specified epoch of deliberate tilt. This movement is much more subtle for track t161 observation for the same pair, relatively speaking. A least squares estimation based on LOS displacements is carried out to estimate this movement by modelling the time series as linearly changing with time with an abrupt jump corresponding to the change discussed here. The movement estimated for track t088 is -4.53 ± 0.82 mm. With actual theoretical movement expected to be 5 mm, the difference between the observations and actual movement is 0.47 mm. For track t161, this shift in the time series is estimated at 0.87 ± 0.76 mm, which gives a difference of 0.07 mm from actual movement. The difference between the estimate of this change in orientation from SAR system and the actual change realized at the site is in sub-millimeter range.

The ability to tilt the double backflip CR using a slider-and-rod mechanism [9] provides an additional degree of freedom for movement in space. This tilt is dictated by the position of the apex-slider attached on either a curved or (in our case) a tilted but straight rod. This characteristic is one of the fundamental ways in which the design of this CR differs from the conventional CRs that have been used until now. Further development in such novel designs might lead to alternative mechanisms that allow for an even greater degree of control over the tilt that can be imparted to such devices with greater ease. The results shown here describes the effect that can be expected in the phase results when such a mechanism is employed at some point during a SAR acquisition to change the orientation of the device towards the satellite. Such a change in alignment can be imparted deliberately to reflection surfaces, as in this case to reduce the misalignment for track t161 (but increase misalignment for track t088) or it could result due to a tilt in the foundation on which the device is fixed. For an Integrated Geodetic Reference Station (IGRS) [8] that couples InSAR, GNSS and levelling, tilt in the device foundation would also influence the results from GNSS due to a tilt in its antenna.

In the following section, when results are computed by assigning the anomalous points as outliers and removing them, the acquisitions from epochs before this deliberate tilt are also removed. The effect of this realignment is addressed in two ways and their effect on the stability of the results is explored in the following section which is dedicated to the discussion of device stability in general.

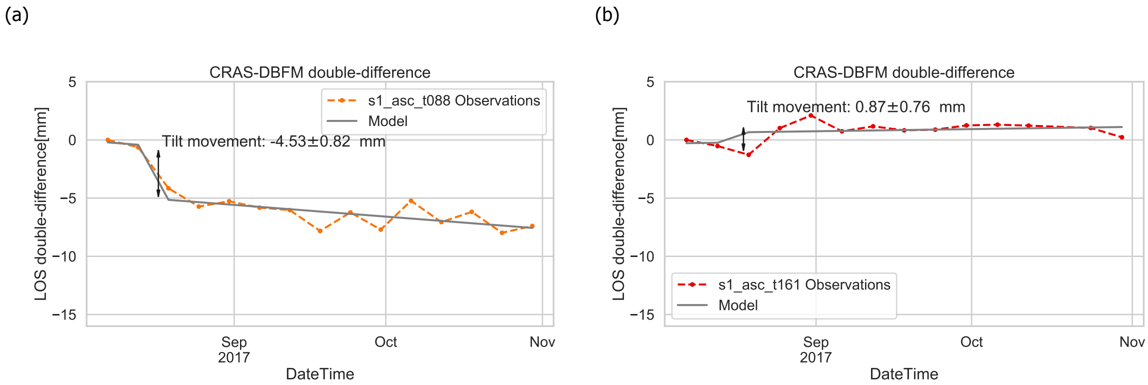

Figure 5.17: LOS displacement time series for device pair CRAS-DBFm as observed from the ascending tracks of Sentinel-1, i.e. track a) t088 and b) t161. The observation time series are modelled as linearly changing with time along with an abrupt jump corresponding to the epoch of 19th August 2017 when a deliberate tilt is introduced in the ascending part of CR DBFm as part of the realignment operation. The grey line represents this model. Movement in LOS direction in the time series is observed from both sub-figures and are estimated as -4.53 ± 0.82 mm for track t088 and 2.12 ± 0.42 mm for track t161 using least squares estimation. The actual movement in the LOS direction from tilt is expected to be 5 mm for track t088 and 0.8 mm for track t161 [63]. These estimates therefore differ from actual movement by 0.47 mm and 1.32 mm respectively.

5.4. Device stability

One of the conclusions drawn from the ground survey results in Chapter 3 is that CRs are observed to be stable at the test site and can thus be used as reference points. Therefore, stability of the device on the test site can be determined by the stability of its vertical displacement time series obtained with respect to CRs.

The stability of such a time series is quantified as a measure of strength of the linear trend present in it. Under ideal conditions, stable devices at the test site shall exhibit no trend in their phase displacement with CR. In practice, small deviations from perfect stability (zero slope estimate) is encountered that stems from variability in phase due to residual topographic height corrections, length of baselines and small swelling-shrinkage movement of soil beneath the foundation. It is assumed here that the slope estimate of double-difference time series for a stable device with respect to CR will be within ± 0.5 mm/quarter. Threshold of this magnitude is selected on the basis of the trends in the double-difference signal of this test site as determined from current and prior levelling campaigns [7] in absence of any significant ground motion except for swelling and shrinkage of soil. However, this assumption can be problematic for shorter time series. In this section, the stability of different devices is compared to each other by analyzing the magnitude of the linear trend in this manner. Similarly, RT MUTE-2 is also observed to be stable at the site from both InSAR and ground-survey techniques (as shown in Section 5.2.1). Thus, the vertical displacement time series for MUTE2-MUTE1 pair are also included here. Figure 5.18 shows the magnitude of linear trend in the vertical displacement time series of different devices obtained relative to CRs estimated using least squares approach. The results are provided for each device pair and are color coded by tracks as shown in the legend. Error bars represent the standard errors of the parameter estimate.

The black rectangle in the figure is used to annotate the device pairs whose vertical measurements exhibit negligible trend. The slope estimates of this group of devices are within the range ± 0.5 mm/quarter. Device pairs involved in this group – DBFT, DBFX and MUTE-2 are therefore considered to be stable at the site. Stability in many of the remaining devices is observed once appropriate corrections are provided. A more detailed discussion focusing specifically on these devices and the effect of corrections is provided in the subsequent paragraphs.

The results annotated in the figure by the gray rectangle depict results from CR-MUTE-1 pairs. The error bars marked by the circles report the linear trend estimated from the original vertical displacement measurements. As mentioned in the previous sections, a significant decline is observed in the vertical displacement time series of MUTE-1 which results in the strong negative linear trend. The trends obtained after carrying out the model-adjustment are quite stable (slope estimates are within the range ± 0.25 mm/quarter) as shown by the triangle error bars in the gray box. The previous sections of this report provide arguments to justify this operation. Once RT MUTE-1 is removed from the test site, device DBFT is installed at the same location. Unlike MUTE-1's displacement results, the vertical displacement results of DBFT are stable (slope estimates are within range ± 0.5 mm/quarter). One of the conclusions drawn from ground survey measurements is that no significant movement is observed at MUTE-1 device location (levelling height differences are within measurement noise of ± 0.2 mm). These measurements spanned the period during which the MUTE devices were operational on the site. The InSAR measurements at the same location obtained through a different PS – DBFT, immediately following this time period support the same conclusion that this location is stable. This increases the confidence in the argument that the trend observed in the MUTE-1's displacement observations do not correspond to any actual ground movement. For if the trend was associated to a ground movement that continued over the course of the year, then this trend would have been observed in DBFT's displacement results.

Devices DBFT and MUTE-1 share the same location but operate at different points in time. On the other hand, the devices ECR-1 and ECR-2 share the same location while working simultaneously, with ECR-1 operating exclusively in descending tracks and ECR-2 in ascending tracks. Thus, their displacement phase results show similar trend behavior. Both RTs exhibit a small positive trend in the vertical displacement time series relative to CRs (average trend of both devices is 1.47 ± 0.53 mm/quarter). A positive trend in vertical displacement result shows that relative to CR the position of RT ECR has lowered over time, indicating that there is a small ground subsidence at this location. Since ground survey measurements are not available for ECR RTs, this motion measured cannot be validated through a different deformation monitoring technique. A notable exception to the agreement in the trend results for ECR-1 and ECR-2 is the result for pair CRAS-ECR-2 in track t088 which exhibits an unrealistically high slope magnitude (5.97 ± 1.225 mm/quarter). This is expected to be an influence of error in addition to the ground subsidence. ECR1, ECR2 and ECR3 were prototype devices that were under development and experienced some hardware issues. This may have affected the results. It is likely that an additional increase in the slope magnitude for CRAS-ECR-2 under track t088 (more than that which can be attributed to ground motion) is due to an error that affects the final three measurement points which leads to a significant increase in an already positively increasing slope result.

The trend results for device pairs involving DBFm are provided for signal before and after applying corrections due to the contribution of deliberate tilt movement. The change in alignment of the ascending half of the device DBFm after the first few observation epochs, on 19th August 2017, results in a strong trend estimates for CRAS-DBFm pair under tracks t088 and t161 (as shown my solid circle markers in Figure 5.18). This effect is corrected using the theoretical movement imparted in the vertical direction (projected from change in LOS) due to the deliberate tilt realignment. Trend estimate obtained after applying this tilt-correction (diamond markers) is significantly reduced for track t088. The tilt-corrected trend estimate for this track resembles the value estimated from track t110 which belongs to descending half of the device and is not affected by misalignment. The effect of misalignment results in a positive trend estimate for observations from track t161. Accounting for this effect by applying the known correction value decreases the magnitude of the slope estimate but not significantly enough to bring it in line with the estimates from track t088 and t110.

Alternatively, this effect is also accounted for by removing data points that correspond to RCS outliers. A data-point is classed as an outlier if the difference of the device RCS for a specific epoch with its mean exceeds by more than three standard deviations. Under this definition, misaligned values of DBFm from track t161 are automatically detected as outliers due to a significant dampening of RCS. For track t088, this effect in RCS isn't observed to be strong enough to classify them as outlier and they are classed as such based on their known realignment condition at the site. For this track, the trend estimate obtained after removing these misaligned values classed as outliers (square markers) is similar to the one obtained after tilt-correction. Removing misaligned data-points as outliers brings the trend estimate for track t161 much closer to the result observed from track t037.

Based on the specified definition of outliers, data points in the vertical displacement time series CRAS-DBFT and CRAS-DBFX as observed from track t161 get classed as outlier as well. The dampening RCS observed at these epochs correspond to a heavy snowfall event in both cases.

Over the course of this experiment, snowfall events are observed to corrupt the reflected signal from both the conventional corner reflector (CRDS) and the new generation corner reflectors (DBFT and DBFX) on the test site. Outliers in phase results observed here corresponds to the same heavy snow event (11th December 2017) as described in the previous chapter. Thus, the heavy snow event that is observed to dampen the RCS also corrupts the phase response of DBFT and DBFX devices. This behavior is not surprising since some amount of snow and debris is expected to stick to the reflection surface of downward-pointing DBF CRs. Although, every instance of phase outliers coincides with snow event, not every snow event causes an accumulation significant enough to result in phase outliers.

Negative trend in the vertical displacement observed for CR-DBFm device pairs (after accounting for the tilt effect) from different tracks suggests an uplift of the device with respect to CRs. While, the trend in vertical displacement obtained from track t037 and t161 shows a more stable behavior which does not agree with the estimates from other tracks. Device DBFX which replaces DBFm at the test site and shares the same location (see Figure 3.2a from Chapter 3) is observed to be stable (slope estimate is within ± 0.5 mm/quarter). This suggests either that ground movement associated with device DBFm is short term or that the trend observed from three tracks can be attributed to measurement noise for this device. The argument that the observed trend in the device DBFm can potentially be attributed to measurement noise is made based on the observations reported in [9] which suggests that the production quality of devices DBFT and DBFX is better in comparison. Device DBFm is part of the initial design cycle (mock-up) with an aim of providing insights for improving the prototypes involved in the next design cycle - DBFT and DBFX. The mock-up design of DBFm is found to be inadequate in stiffness and prone to vibrations. Based on these lessons, the device design was modified for devices DBFT and DBFX (for instance a frame is introduced in the new devices to lift the weight of the reflection-surfaces and maintain their orthogonality). Eventually the design of device DBFT is selected for Integrated Geodetic Reference Station (IGRS) and about 30 stations are installed in the Netherlands for deformation monitoring applications [68]. There is a possibility that under strong wind conditions, the lack of adequate stiffness in device DBFm results in a relative motion between the device and its foundation pad under stable ground conditions which is responsible for the trends. However, this possibility cannot be put to test as the ground survey measurements are not available for this device and thus there is no evidence to support this argument. In the following subsection, multi-geometry estimate is utilized to combine the observations from different tracks for this device pair to test whether the trends observed are caused by an error in projecting the LOS measurements into vertical direction to obtain vertical component. Perhaps a strong horizontal movement present in the device might result in the trends in the vertical components if they are erroneously assumed to be negligible. It must be noted also that the time period of operation for this device is short, spanning only three months from August to November 2017. Thus, the interpretation of a short-term trend to actual ground motion must be carried out with caution.

This kind of conflicting phase behavior across two different tracks is also observed for device ECR-3. The vertical displacement for this RT paired with CRAS leads to a similar time series from tracks t161 and t088, however, the result from track t088 exhibits a higher magnitude of trend (1.191 ± 0.282 mm/quarter) while the time series from track t161 is more stable (0.009 ± 0.455 mm/quarter). One possibility for the higher trend estimate in the ascending track t088 is that the phase results for this device as observed from this track happen to have a higher noise level. As mentioned before, the ECR family of devices are experimental in nature and the performance of these devices can have anomalies.

To summarize, this section compares the magnitude of linear trend estimated in the vertical displacement time series result for different device pairs to analyze its stability at the test site. From this result, devices DBFT, DBFX and RT MUTE-2 are determined to be stable. For device MUTE-1, this stability is achieved after applying the model-adjustment which involves removal the trend and the step in the time series.

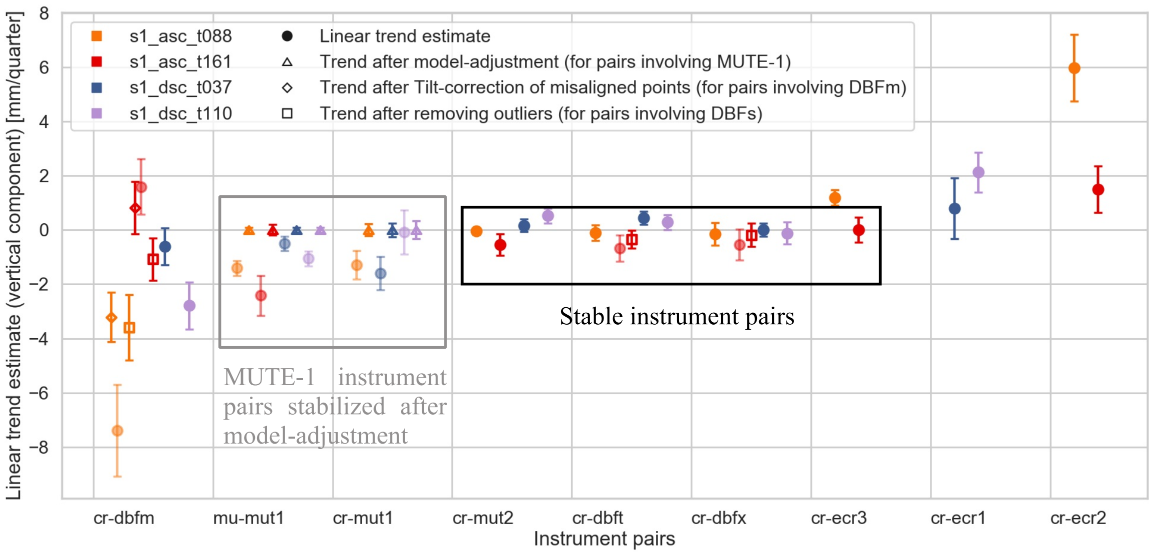

Figure 5.18: Comparison of device stability relative to CR reference point represented as the magnitude of linear trend observed in the vertical displacement time series (obtained as a projection from LOS direction). Error bar represents the standard errors of the parameter estimate. Stable device pairs are identified as ones having slope magnitudes within ± 0.5 mm/quarter range and are annotated in the figure using a black rectangle. The gray rectangle covers the results for pairs involving MUTE-1 where the time series is stabilized after model-adjustment (trends obtained after model-adjustment are represented by triangle markers). Strong trends for device pairs involving DBFm are observed from ascending tracks t088 and t161 since the device is subjected to deliberate tilt. Tilt-correction applied to account for these misaligned values reduces the trend estimate (diamond markers) for track t088 which agrees with the trend estimate from descending track t110 (not effected by misalignment) and for track t161 where this correction is not significant enough for this estimate to match the results from other tracks. As an alternative, the effect of misalignment is also accounted for by removing outliers from displacement results. Trend estimate after removing outliers (square markers) for track t161 is comparable to the estimate from track t037. The differences in trend estimate before and after removing outliers for CRAS-DBFT and CRAS-DBFX under track t161 are not statistically significant.

5.4.1. Comparison of estimates from multi-geometry estimate for DBF CRs

This section presents the results after combining measurements from multiple tracks of Sentinel-1 for DBF family of devices similar to the results provided in Section 5.2.2 for MUTEs. This combination allows for estimation of the horizontal and vertical motion by utilizing multiple geometries. Thus, the horizontal and vertical stability of the DBF class of devices can be checked here. Their stability is quantified here in terms of the magnitude of trend obtained for displacements with spatial reference points (CRs – CRAS and CRDS). Using this approach also provides an opportunity to test whether accounting for horizontal motion explains the trend observed in the vertical displacement for CR DBFm.

Comparison of vertical components from 2 component estimation

The modified multi-geometry combination carried out for CR-DBF displacements to estimate its components is accomplished in the same manner as described for CR-MUTE pairs in Section 5.2.2, using the conventional three component estimation and a modified method that assumes that there is no contribution from the North-South component. This section reports the result from the modified approach which provides relatively better precision.

The standard deviation of vertical components estimated using this approach for DBFT is 0.238 mm and for DBFX is 0.315 mm. This precision of estimated vertical component of displacement time series obtained from four different Sentinel-1 tracks is well within the error-budget of 0.65 mm in the vertical direction (mean of set of four values ranging from 0.59 mm to 0.70 mm for four difference tracks given the error-budget is 0.5 mm in LOS [9]). As stated earlier, the stability of the devices is gauged here based on the trend of vertical displacement time series obtained with respect to points assumed stable at the site. A linear trend of 0.082 ± 0.055 mm/quarter is estimated for DBFT's estimated vertical displacement and for DBFX this value is obtained as -0.134 ± 0.072 mm/quarter. This trend estimate for DBFX would reduce quiet significantly even further if the outlier definition is made stricter to exclude values more than 2.5 standard deviations away instead of 3 standard deviations away. Thus, devices DBFT and DBFX are estimated to be stable at the test site when observations across different Sentinel-1 tracks are combined.

By contrast, trend obtained for device DBFm is significantly negative with a value of -2.038 ± 0.222 mm/quarter, as shown in Figure 5.19 which shows the estimated vertical component as a blue time series with a shaded stripe representing the standard error of parameter estimate. As mentioned before, this points to either a severe measurement error arising from its relatively lower production quality or an actual ground movement that spans for a period short enough not to be detected by device DBFX which shares the same location afterwards. Another possibility is that the detected motion occurs between the device and its foundation pad while the ground movements are stable. To test the presence of horizontal motion for DBFm and other DBF devices, the following subsection compares the horizontal components estimated by combining observations from multiple geometries.

Comparison of horizontal components from 2 component estimation

The horizontal component obtained here concerns motion in the East-West direction. Unlike its estimated vertical component, the horizontal East-West component obtained for DBFm using the modified multi-geometry approach is stable. Trend of magnitude -0.091 ± 0.269 mm/quarter is obtained by a linear model fit to the data in least squares sense.

Accounting for the horizontal movement using the modified multi-geometry approach shows that for device DBFm, horizontal movements are negligible. There is still a significant trend in the vertical displacement time series even when the vertical component is obtained by accounting for a potential motion in the horizontal direction using data from multiple satellite geometries. Thus, the trends observed in the vertical component results of DBFm obtained by projection from LOS are not caused by erroneously ignoring the motion in the horizontal direction and this argument as a potential explanation of the trends in the vertical component result can be rejected. Figure 5.21a depicts the East-West component (as a brown time series) along with its trend (grey line) for device DBFm. This stability in the estimated East-West component is also observed for DBFX which has the slope estimate of 0.079 ± 0.070 mm/quarter.

By contrast, there is a small positive trend in the East-West component estimated for device DBFT. This trend is shown by the grey line in Figure 5.21b fit to the signal in a least-squares sense depicted by the brown time series. A positive trend in the CR-DBFT East-West displacements suggests that relative to CR, device DBFT is moving in the western direction. This westward rate of movement is estimated at 0.361 ± 0.061 mm/quarter.

As mentioned in Section 3.3 and shown in Figure 3.2a, device DBFT replaces the RT MUTE-1 at the test site and thus the two devices share the same location. Interestingly, device MUTE-1 also demonstrates a westward motion which is observed from InSAR results (East-West component estimated from MUTE2-MUTE1 and CR-MUTE1 using modified multi-geometry estimation procedure) and validated by ground survey results (levelling and total station East-West displacements). For instance, see Figure 5.12a and Figure 3.9. Thus, westward motion observed in device DBFT can be attributed to the continual westward movement of this location that is also observed before this period with the results of device MUTE-1. The result presented here confirms the westward motion in DBFT that is identified in [9].

The concrete pad deployed at this location WASS01 shared by DBFT and MUTE-1 is of the larger dimension 2 m by 2 m by 0.15 m. Table 5.5 summarizes the westward tilt in these two devices obtained from their displacement measurements in the East-West direction with MUTE2 and CRs from different techniques. The table is sorted by degrees of freedom which gives a measure of number of measurement points in the period of operation and the InSAR results are reported in the final three rows. Three measures of the tilt detected in the western direction are reported: a) maximum motion observed in the western direction with respect to the position of the first operational epoch during the entire time period that the device is operational, b) the motion measured in the western direction at the end of the device operation with respect to the position of the first epoch and c) rate of movement estimated in the western direction as a trend in the East-West displacement time series obtained using least squares. While the tilt recorded on the final epoch is close to 1 mm, the reported maximum tilt for InSAR results suggests that over the course of the experiment tilt movement has exceeded more than a millimeter. The standard error of the estimated trend is also reported along with RMSE of the fit of this linear model. These measures of westward tilt obtained for DBFT and MUTE-1 from different measurement techniques are comparable to each other. Small disagreements that are observed between these results can be attributed to the fact that the signals obtained from DBFT and MUTE-1 correspond to different time periods. For pairs involving MUTE-1 although the difference in time periods is small and the operational periods overlap with each other, the signal has been sampled at different rates. InSAR measurements are available from satellite acquisition every six days while the high precision ground survey measurements are carried out less frequently.

Similarly, tilt in the concrete pad foundation is also observed for RT MUTE-2 in the eastwards direction from InSAR observations (East-West component estimated from modified multi-geometry estimate as shown in Figure 5.12a) which are validated by ground survey results (levelling and total station East-West displacements as shown in Figure 3.9). This accounts for the particularly severe tilt observed for MUTE2-MUTE1 pair from InSAR technique in Table 5.5 as both devices tilt in opposite direction. Location WASS01 is equipped with a larger concrete pad installed in the vicinity of a water canal while the location of RT MUTE-2 (WASS02) is furnished with a pad of smaller dimension (1.5 m by 1.5 m by 1.5 m) installed farther away from canal. Therefore the changing water levels in canals does not explain the tilt at both locations and the source of this error must lie in the design of concrete foundation itself. Incidents of foundations tilting at multiple locations, designed with different dimensions, calls into question the design of concrete pads employed to act as stable foundation especially for an IGRS station where the integration of the multiple datasets relies on a sound connection of the foundation to the ground such that all measurements can be reliably attributed to ground motion. Ideally the foundation of the system would only reflect changes in the ground motion and would not be subject to tilts related to small scale motions in the topsoil.

In summary, results obtained after combining observations from multiple tracks of Sentinel-1 suggests a trend in the vertical component for device DBFm which is observed to be stable in horizontal direction. Device DBFX is found to be stable in both horizontal and vertical directions. Device DBFT on the other hand is stable vertically but exhibits a tilt in the western direction. This motion is associated with the tilt in the foundation that is also observed for device MUTE-1 and is quantified in multiple ways in this section. These tilts are observed to be of comparable magnitudes across different measurement techniques.

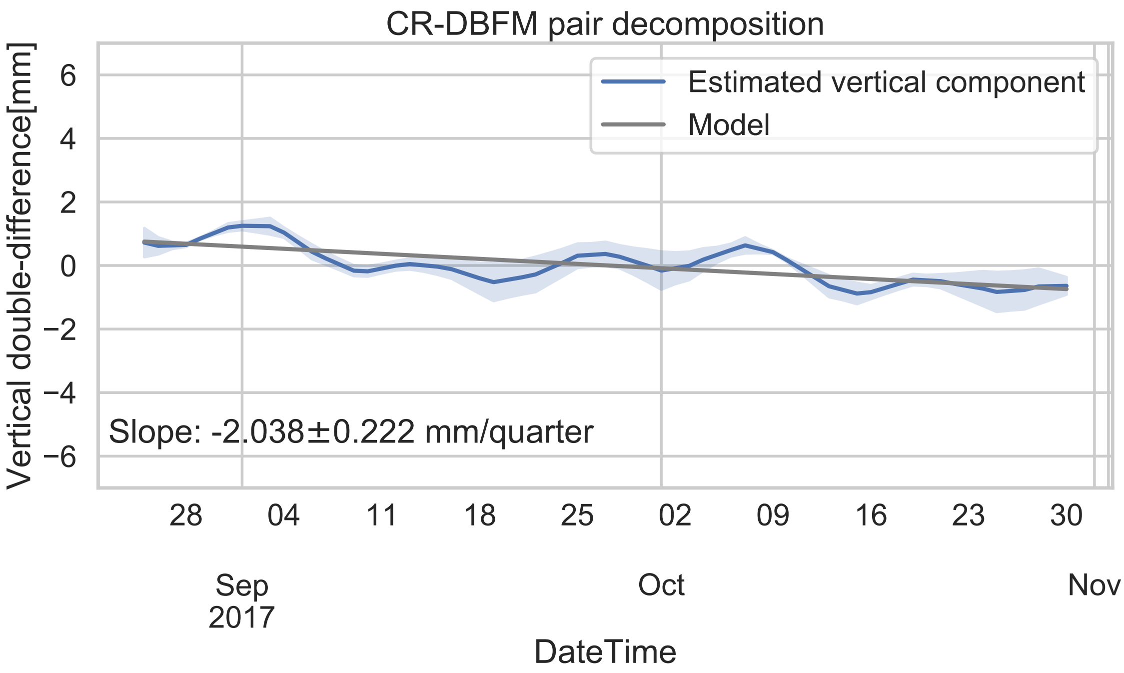

Figure 5.19: Estimated vertical displacement time series obtained from modified multi-geometry InSAR results for CR-DBFm pair. Observations from four Sentinel-1 tracks are utilized along with their geometry to obtain two components using least-squares approach (assuming no contribution from North-South component). The vertical component is shown here as a blue time series with its shaded stripe representing the standard error of this parameter estimate. The grey line represents the linear model fit to the time series in a least-squares sense. The trend of this vertical-component obtained from the linear model is reported in the figure.

5.5. Comparison of a-priori and posteriori precision

This section reports the precision of observations as one standard deviation value and compares this statistic to the one approximated a-priori in Section 4.4.8. Such a comparison allows us to test how accurately the precision of the result can be approximated by extracting the signal and clutter using the approach selected in this study. The a-priori approximation is obtained for LOS displacements and thus the comparison is provided for this component. It is derived from signal and clutter estimate value obtained for each device using MLE, which is then propagated to the difference between each device pair.

Posteriori standard deviation is obtained for corrected observations wherever applicable. Corrections are provided for observations from DBFT-DBFX, MUTE-1 and DBFm for removing data points affected by extreme meteorological events, for providing model adjustments and to account for the manual tilt imparted respectively. The type of correction applied to the observation to obtain this posteriori estimate is specified in the third column of Table 5.6 while the DOF specifies the measure of the number of observations used for this computation. The table is sorted in ascending order by the difference between the two approaches and these differences are reported in the final column. The agreement between the two approaches is excellent and within 0.911 mm. The result from CRAS-ECR2 from track t088 is ignored here since the high difference between the standard deviations in this case results from the problem encountered in the final three data points as mentioned in Section 5.4. For a few device pairs, the difference between approximation and observations is less than 0.1 mm while

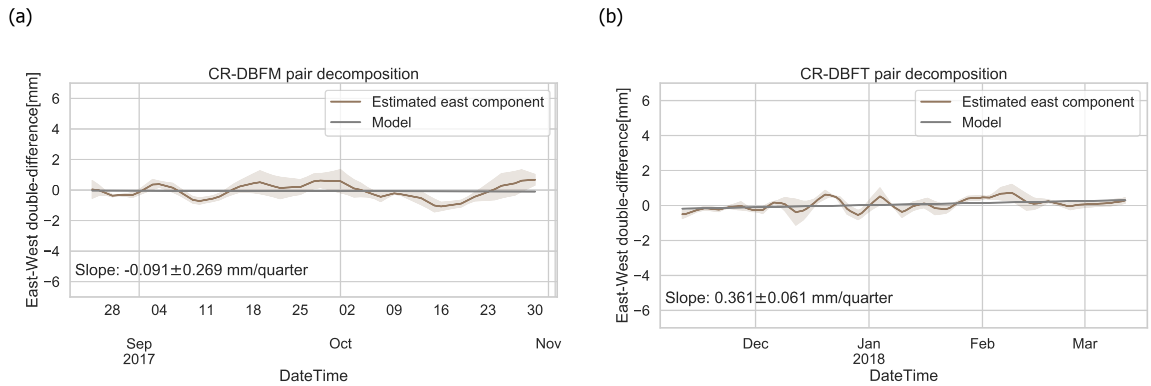

Figure 5.21: East-West displacement time series obtained from modified multi-geometry InSAR. Observations from multiple tracks of InSAR are utilized along with satellite geometry to estimate two components using least-squares by ignoring the North-South component. The sub-figures show displacement time series for (a) East-West component for CR-DBFm pair and (b) East-West component of CR-DBFT pair shown here as brown time series with its shaded stripe representing standard error of this parameter estimate. The time series are modelled linearly as shown here by the grey line and fit to the data using least-squares method. The trend for device DBFm is not significant and the device is considered stable in this direction. Device DBFT however has a small positive trend in its East-West displacement time series which suggests that relative to CR, device DBFT is moving in westwards direction. This motion is attributed to a tilt in the concrete pad.

Device Pair	Method	Component	Start of operation	End of operation	DOF	Rate of westward tilt [mm/quarter]	Rate Error [mm/quarter]	Deg1 RMSE [mm]	Max. westward tilt detected during operation [mm]	Westward tilt detected at the final epoch of operation [mm]
MUT2 - MUT1	Levelling	East-West	2016-09-21	2017-08-15	4.0	0.307	0.05	0.115	1.0	1.0
MUT2 - MUT1	Total station	East-West	2016-12-27	2017-08-15	4.0	0.207	0.164	0.259	0.9	0.82
CR-DBFT	Modified multi-geometry estimation	East-West	2017-11-11	2018-03-12	120.0	0.361	0.061	0.26	1.229	0.79
CR-MUT1	Modified multi-geometry estimation	East-West	2017-02-26	2017-08-25	179.0	0.289	0.075	0.582	1.95	0.953
MUT2-MUT1	Modified multi-geometry estimation	East-West	2016-11-13	2017-08-25	284.0	0.227	0.027	0.418	2.513	1.873

Table 5.5: Westward tilt estimates at location WASS01 that corresponds to the location of RT MUTE-1 and subsequently the location of device DBFT. The results are reported here for East-West displacements obtained for different device pairs. InSAR results are reported here for East-West component estimated by combining observations from multiple Sentinel-1 track geometries (assuming no contribution from the North-South component). For MUTE pairs, East-West components are also reported from ground survey results (levelling and total station). Measure of westward tilt is provided as 1) the maximum westward motion (with respect to first epoch) that is detected in the signal through out the span of operation, 2) the tilt observed on the final epoch at the end of the operation period (with respect to the first epoch) and 3) the rate of movement estimated as a trend using least squares in the time series along with the standard error of the estimate and the RMSE of the linear model fit. The table is sorted in ascending order of DOF which is a measure of the total number of data points. These measures of westward tilt in DBFT and MUTE-1 are comparable to each other. Small disagreements between these values can be attributed to the different sampling rates of the signal and to the fact that the time series correspond to different time periods. The maximum detected tilt and the tilt detected at the end of operation with respect to the first epoch for device pair MUTE2-MUTE1 are particularly severe as the foundation of MUTE2 is estimated to be tilting towards the east while that of MUTE-1 is tilting towards the west.

Device pair	Track	Time series type	DOF	a-priori displacement std.dev[mm]	a-posteriori displacement std.dev[mm]	Δ displacement std.dev[mm]
mut2_mut1	s1_dsc_t110	Model-adjusted	37	0.452	0.458	0.006
mut2_mut1	s1_dsc_t037	Model-adjusted	37	0.351	0.408	0.057
cras_dbfx	s1_asc_t161	Outliers-adjusted	19	0.549	0.61	0.06
cras_mut2	s1_asc_t088	Model-adjusted	26	0.277	0.372	0.096
cras_dbft	s1_asc_t088	Original	20	0.325	0.45	0.125
cras_dbfm	s1_asc_t161	Outliers-adjusted	9	0.33	0.459	0.129
mut2_mut1	s1_asc_t088	Model-adjusted	43	0.391	0.54	0.149
crds_dbft	s1_dsc_t037	Original	20	0.217	0.366	0.15
mut2_mut1	s1_asc_t161	Model-adjusted	16	0.509	0.666	0.156
cras_dbft	s1_asc_t161	Outliers-adjusted	19	0.306	0.481	0.174
cras_mut1	s1_asc_t161	Model-adjusted	6	0.512	0.309	0.203
crds_dbfx	s1_dsc_t037	Original	20	0.134	0.337	0.203
cras_mut1	s1_asc_t088	Model-adjusted	26	0.423	0.628	0.205
crds_dbft	s1_dsc_t110	Original	18	0.205	0.426	0.22
crds_mut1	s1_dsc_t037	Model-adjusted	22	0.3	0.559	0.259
crds_mut2	s1_dsc_t037	Model-adjusted	24	0.248	0.534	0.285
crds_ecr1	s1_dsc_t037	Original	6	0.618	0.923	0.305
crds_ecr1	s1_dsc_t110	Original	4	0.555	0.937	0.382
crds_dbfm	s1_dsc_t037	Original	14	0.207	0.593	0.386
cras_mut2	s1_asc_t161	Model-adjusted	6	0.298	0.687	0.388
cras_ecr3	s1_asc_t161	Original	17	0.341	0.761	0.42
cras_dbfx	s1_asc_t088	Original	20	0.245	0.679	0.434
crds_mut2	s1_dsc_t110	Model-adjusted	25	0.296	0.741	0.445
cras_ecr3	s1_asc_t088	Original	19	0.279	0.758	0.479
crds_mut1	s1_dsc_t110	Model-adjusted	24	0.358	0.847	0.489
crds_dbfx	s1_dsc_t110	Original	18	0.111	0.63	0.519
cras_ecr2	s1_asc_t161	Original	12	0.25	0.837	0.587
cras_dbfm	s1_asc_t088	Outliers-adjusted	11	0.291	1.166	0.875
crds_dbfm	s1_dsc_t110	Original	14	0.179	1.091	0.911
cras_ecr2	*s1_asc_t088*	*Original*	*13*	*0.302*	*1.941*	*1.639*

Table 5.6: Comparison between LOS displacement standard deviation approximated a-priori and obtained posteriori from InSAR observations. The table is sorted by the difference between the two which is reported in the final column. The a-priori values are approximated using ML estimates of signal and clutter. Posteriori statistics are obtained for time series after applying appropriate corrections. The type of time series used for such a computation is specified in the third column. The number of observations used to compute this precision measure are specified by the DOF. The agreement between the a-priori and posteriori standard deviation is within 0.911 mm (result from CRAS-ECR2 for t088 is rejected because of the issue with the final three data points as mentioned in the previous section). For several device pairs this difference is less than 0.1 mm and for MUTE2-MUTE1 time series observed from track t110 this difference is as low as 0.006 mm. Note: The mock-up device 'DBFm' is marked as 'DBF_' here.

for MUTE2-MUTE1 time series this difference comes down to 0.006 mm.

The results provided in this section show a good agreement between the a-priori approximation and the standard deviation obtained from observations, which means that the precision of result can be approximated with a good accuracy by extracting signal and clutter using the approach provided in this study. The precision of the LOS phase displacement observations analyzed in this Chapter is within 1.166 mm. The standard deviation of CR-ECRs observations tend to be higher than for other devices pairs. However, for the remaining device pairs- CR-DBFs, CR-MUTEs and MUTE2-MUTE1, the precision measure are similar to each other.

The results reported in this and the preceding chapter presents the phase and amplitude characteristics of different AR devices. The following chapter presents the conclusions drawn from these results regarding the performance characteristics of these devices by answering the research questions proposed in this study.

6
Conclusions and Recommendations

The preceding chapters of this report cover the amplitude and phase analysis of different ARs. The stability of amplitude and phase across different types of devices is presented along with the factors affecting this stability. This chapter presents the conclusions drawn from these results to answer the research question proposed in this study followed by some recommendations for future studies on this topic. The conclusions are presented for all artificial reflectors except the ECR family since their devices installed on the test site are experimental prototypes and the measurement time series of these devices are relatively short.

6.1. Conclusions

The main research question is divided into sub-questions to cover the findings regarding the assessment of PS device response (amplitude and phase), comparison of results with ground truth (phase) and influence of external factors (amplitude and phase).

1. How can the response of installed PS devices be defined and estimated from the satellite images?

   (a) Which methods can be used to extract signal and clutter radar cross section (RCS) from satellite images?, and

   (b) How do the different methods perform in estimating reflectance response?

   The amplitude signal and clutter response of PS devices are expressed as RCS in the dB scale. The signal is extracted from SAR images as the peak of the impulse response function (from mean and instantaneous positions) and as a scaled-integrated response of the main lobe of the impulse response function. However, the signal RCS derived from all three methods are almost equivalent to each other and the method adopted to extract it will not significantly affect the analysis.

   The dominant nature of the signal overshadows the clutter in the resolution cell making it difficult to extract clutter from the same cell at the same time. Thus clutter from SAR images is extracted from the same location in space (as that of the PS device) but at a different point in time and from the same temporal instants when the device is operational but at a different spatial location than the resolution cell that the device occupies (obtained as peak and the integrated value of the impulse response function). Of all the methods, no single approach to extract clutter proves to be better than others across all devices. To approximate a-priori phase variance, a single representative signal and clutter value is utilized which is obtained directly from amplitude time series (for device operational epochs) using ML estimation. Simulations show that MLE is better at approximating true values of Rician Distributed signal and clutter than a sample or population statistic.

(c) Do the different devices at the test site show stability in its RCS and phase response?

The stability of the device response at the test site is determined using the slope of the linear model fit to the time series in the least-squares sense. Devices with RCS trend estimate within ± 0.5 dBm^2/quarter are considered to have stable amplitude response, while the phase response of a device is considered stable if the slope of the vertical displacement time series obtained relative to CRs is within ± 0.5 mm/quarter. Displacement time series is obtained using conventional CRs as reference points because the ground survey campaign establishes them to be vertically stable at the test site throughout the experiment. Conventional CRs (CRAS, CRDS), two DBF CRs - DBFT, DBFX and RT MUTE-2 are phase stable. These devices also show amplitude stability once appropriate corrections are applied. The lack of amplitude and phase stability in MUTE-1 and DBFm is explained by the influence of external factors which is discussed in subsequent paragraphs.

2. How do the results from ground survey compare with those from InSAR across different platforms?

   (a) Are the "artificial" deformations that are introduced deliberately, detected in the result? What is the error associated with this value?

   The deliberate vertical movement of 7 ± 0.05 mm imparted to the device MUTE-1 on 7th March 2017 as part of the detection experiment is estimated using InSAR displacement time series to a deviation of 0.69 ± 0.01 mm with a one sigma precision of 0.91 mm. Thus, InSAR observations can account for changes in vertical motion over a vegetation area with low backscattering characteristics using RT devices as PS points in the field with sub-millimeter precision.

   The ascending half of device DBFm is imparted an additional tilt of $6.4°$ to reduce the misalignment for track t161. The resulting change in RCS and phase response in the ascending half of this device as estimated from InSAR observations are in line with the changes expected from theory (RCS levels observed are within 1.7 dBm^2 of theoretical levels and LOS displacements are estimated within 0.47 mm). These results demonstrate the effect such an additional tilt provided to the device (either deliberately or otherwise) has on the amplitude and phase.

   (b) Is there an agreement between displacements observed from satellite techniques and ground level surveys carried out at the test site?

   The InSAR vertical displacement time series for MUTE-1 device pairs diverges from the ground survey results. This is due to the presence of a strong linear trend and step jump (between epochs 12th June and 15th June 2017) in the time series. The presence of the linear trend is not caused due to unresolved horizontal movements (for instance by a potential loose connection of one of the bolts). Once the trend and step behavior are modelled and removed ('model adjustment step'), then the measurement time series from both techniques are in agreement within one standard deviation error bounds. The vertical displacement observations obtained for device pairs involving MUTE-2 agree with the levelling measurements within the error bounds without carrying out any adjustment/correction step. The behavior of MUTE-2 RT, which is a second-generation device of this class, on the test site is similar to the conventional CR. This demonstrates that although MUTE-1's performance seems to be affected by external factors, it is possible to use RTs of second-generation type to act as reliable PS points.

   InSAR results derived for the East-West projection by fusing data from multiple geometries for MUTE devices agree with ground survey measurements within the error bounds. The interpretation of horizontal movement from InSAR's East-West projection is in line with the conclusion derived independently from ground survey measurement that the location WASS01, housing devices MUTE-1 and DBFT, tilts in the western direction (estimates of maximum tilt vary from 0.9 to 1.95 mm) while the concrete pad of location WASS02 on which MUTE-2 is installed exhibits a tilt towards the east (about 2 mm in magnitude). The rate of westward tilt of WASS01 detected from different techniques varies from 0.207 ± 0.16 mm/quarter to 0.361 ± 0.06 mm/quarter. Such tilt motions in the two slabs aren't caused by changing water levels in the nearby canal but results from the susceptibility of concrete foundation design to swelling and shrinkage of soil. Therefore, the two types of concrete pads used and installed as device foundations in a manner described in this study prove to be inadequate especially for an IGRS station.

3. What is the relation between the RCS and phase errors and different factors that influence the device response?

   (a) What is the influence of meteorological factors, device malfunctioning and temperature on the RCS and phase results of PS points?

   Certain heavy snow and rainfall events result in the accumulation of excess snow/water in the apex and on the reflection surfaces of the CRs. Precipitation instances are identified as heavy snow or significant rainfall events when the cumulative sum of snow and rain measurements in the last twenty-four hours before acquisition as measured from weather station exceeds 2 magnitude value (where 1 magnitude value suggests a single snow occurrence detected each hour or at the time of observation) and 10 mm respectively. Such accumulation of excess snow and water dampens the amplitude and corrupts the phase of the signal resulting in outliers in RCS and displacement time series. This assertion has been validated for CRDS, whose RCS and displacement time series outlier identified on 12$^{\text{th}}$ February 2017 has been confirmed by a chance visit to the site. The heavy snow events affect the amplitude and phase results of both conventional and double backflip CRs, while the impact of heavy rain remains limited to the conventional reflector type. This suggests that the downward-pointing design of DBF CRs drains the water preventing its accumulation in the apex. The susceptibility of DBF devices to snow is not surprising since some amount of snow and debris is expected to stick to its reflection surface and affect the results.

   The amplitude and phase response of MUTE RT devices is sensitive to temperature. Applying temperature correction to MUTE amplitude response lowers the RCS levels by 0.5-2 dBm^2 and stabilizes the amplitude time series (lowering the severity and RMSE of the linear trend) however its effect on phase results is negligible. Therefore, according to the phase-temperature relationship obtained from the laboratory experiment, temperature correction accounts for neither the step nor the linear trend in MUTE-1 phase results. The laboratory experiment carried out may have failed to capture the increased sensitivity of this device to temperature. Another possibility is that a device malfunction in the electrical component of the device ('aging' of RT sensors for instance) linearly degrades the phase and amplitude response transmitted by the device and is responsible for the sudden drop in response between 12$^{\text{th}}$ and 15$^{\text{th}}$ June 2017. The fact that amplitude and phase response of MUTE-2 (which is a second-generation MUTE RT) does not exhibit this trend and step behavior points to a flaw in the performance of electric components specific to the first-generation MUTE RT device.

   (b) How do the phase variances obtained from RCS compare with those obtained from measurements?

   Anomalies in phase observations not resulting from any actual ground movements correspond to the anomalies in RCS. For RT devices, RCS acts as a measure of the electrical performance of the device. Its analysis helps identify the anomalies in the phase resulting from factors affecting the electrical performance of the device like temperature influence and device malfunction. For CRs, anomalies in the RCS time series help identify phase corrupted by precipitation events due to the accumulation of excess rainwater/snow in the apex.

Phase standard deviation approximated from SCR is in agreement with the standard deviation obtained from observations. The difference between the statistic approximated and observed for different device pairs is within 0.91 mm (for some pairs this difference is lower than 0.1 mm). Therefore, the precision of the results can be approximated by extracting signal and clutter using the approach provided in this report.

The main research question of this thesis is answered as follows:

How can the environmental and instrumental factors that affect the performance of radar transponders and double backflip corner reflectors as artificial point scatterers be quantified?

The performance of the different ARs is affected by factors depending on the type and nature of the device. Outliers in CR phase response resulting from the influence of significant precipitation events can be identified and removed using corresponding outliers in amplitude. The influence of temperature on the performance of MUTE RTs quantified using laboratory correction factors accounts for the dependence of RCS and phase on temperature (the correction for phase is insignificant relative to the noise in the time series). The amplitude and phase response of first-generation MUTE RT devices shows a trend and step that is quantified and accounted for using a model ('model adjustment'). This correction is justified based on the argument that it accounts for either an instrument malfunction specific to the first-generation RT device or for a temperature influence on the performance of the device. Once the model adjustment step is carried out, InSAR measurements are validated by ground survey observations for all CR-MUTE pairs from all Sentinel-1 tracks. InSAR measurements using the new class of (unconventional) devices can quantify deliberate movements imparted to them within sub-millimeter range (deliberate vertical movement in MUTE-1 within 0.69 mm and deliberate tilt in DBFm within 0.47 mm).

The main finding of this study is that of all the devices installed at the test site, conventional CRs, double backflip CRs (of higher production quality than mockup) and the second-generation MUTE RTs show a phase stable performance during the experiment making them suitable for InSAR ground monitoring applications and as an IGRS station. Better quality of instrument foundation can be provided for their use as an IGRS station since both the large and small concrete pads utilized here are susceptible to tilt. The DBFm mockup device lacks adequate structural stiffness while the first-generation MUTE RT shows an erratic trend and step in its response. Such behavior from a RT introduces an ambiguity in the interpretation of phase results where such a trend would superimpose on the displacement signal. And while the analysis of RCS may help *identify* such behavior, it cannot be utilized to account for this effect. The introduction of such behavior is akin to the unknown phase error introduced by bulky CRs due to settlement under self-weight.

Second generation MUTE RT and DBF CRs have emerged as the two successful alternatives in this study. MUTE-2 requires only a single setup for ascending and descending pass while being lightweight and inconspicuous. Also, as demonstrated in this study, collocating levelling and total station techniques with InSAR is feasible along with GPS (which is demonstrated in [7]). The location constraint of this device to be in the vicinity of a power source is no longer an issue if adequate sun exposure is available as shown here by the seamless switch to solar panels with no effect on its performance. Its drawbacks include the higher costs involved in using electronic sensors and the temperature sensitivity of these sensors that can affect its performance. The other alternative in the form of DBF CR, provides "best of both world" features. Like a conventional CR, the reflection surfaces of this device are metallic making them inexpensive, relative to their electronic counterpart. Like a RT, only one setup is necessary for its operation in ascending-descending tracks and it allows the collocation of reference points from several other deformation monitoring techniques. But with device leg-length of 0.9 m (for the devices used here), they are still bulky in size and inconspicuousness of a RT is absent. Although their downward-pointing design provides a drainage solution to the problem of accumulation of water in its apex, these devices are susceptible to heavy snow events. Therefore, the decision of employing either one of these devices in a future study depends on the further advances in sensor technology of RTs, budget constraints of the project, availability of other deformation monitoring techniques, the nature of the test site and the need for protection of these devices once installed. The following section provides some of the recommendations for such future studies carried out with such ARs.

6.2. Recommendations

Based on the findings of this study, the following recommendations are proposed for future research in this field:

Foundation design footing

The concrete pads installed at the site at two different locations are observed to be tilting gradually introducing movement in the horizontal directional components. Other alternative designs of this device foundation can be explored in future studies to prevent such changes. Designing the device foundation as a footing is proposed as an alternative. The dimensions of such a footing can be determined using the load of the supporting device and the bearing capacity of the soil by ensuring that there is little to no settlement under self-weight. The presence of packed soil over the projected foot-pad can ensure that any settlement that occurs shall be uniform with minimal tilt. Although the lack of the exposed concrete pad surrounding the device and its replacement with grass would impact the clutter characteristics.

Virtual location

The virtual location capacity of the RT device can be tested by designing an experiment where a deliberate phase delay is introduced so that its location is registered at another region in the SAR image. Such an experiment can be used to test if the SCR of a PS point can be improved by virtually locating the device over a region where the clutter level is lower.

Extended time series

A longer time series of RCS and displacement should be generated from the devices that are still present on the test site. A longer time series will provide a better interpretation of the long term trends and cycles present in it. A longer deployment of MUTE devices on the test site will enable a distinction in the influence of temperature and device malfunction on the RCS and displacement performance of device MUTE-1. A sensor comparison can also be made using SAR data from TerraSAR-X and COSMOSkyMed that cover this test site. Such a comparison will provide a comparison of the performance of different devices across different satellites. This can provide valuable information that can aid the interpretation of the results.

A

Appendix A

This study describes the performance of new generation of reflector devices from the standpoint of their suitability for deformation monitoring applications. With an ability to tilt the reflector, the DBF family of device provides an additional degree of freedom for movement in space[8]. The first part of this appendix provides the geometrical description of DBF devices which explains how such a movement is constrained and what changes can be expected when the movement isn't constrained perfectly or when some additional errors are introduced (deliberately or otherwise) that imparts a further tilt in the device. The second half of this appendix provides the observations on the basis of which the ground survey results for MUTE RTs and CRs are presented in Chapter 3. These results play a crucial part in comparison and interpretation of the results presented in Chapter 5.

A.1. Geometry and orientation for DBF CRs

This section is based on the work of [8, 9] and provides a brief description of the geometry of the DBF family of devices and their orientation towards different satellite tracks.

Figure A.1 shows the geometry of a typical DBF phase center. The vector marked signal points towards the direction of the satellite incidence and thus the angle formed by this vector with respect to vertical gives the incidence angle. While, boresight denotes the vector of maximum RCS. Ideally this vector should be aligned towards the direction of the satellite in order to maximize the RCS response in satellite observations. However, it is possible that the boresight of the device does not point towards the satellite perfectly due to an error in orienting the device or as in this study, multiple tracks are available for ascending and descending passes and the device is pointed towards the average direction of the two tracks. Irrespective of the reason, there is possibility of an offset being introduced between the signal and boresight vectors, which is termed as misalignment.

The DBF family of devices exhibit a natural downward tilt with respect to vertical that may exhibit some self cleaning properties under windy conditions. This tilt is provided in such a way that the z axis points to the ground. It is defined by the angle formed by the reflector backplate and the vertical. Using the geometry described in Figure A.1:

$$\begin{aligned} \angle\text{Misalignment} + \angle\text{Incidence} + \theta - \angle\text{Tilt} &= 90°, \\ \angle\text{Tilt} &= \angle\text{Misalignment} + \angle\text{Incidence} + \theta - 90°. \end{aligned} \tag{A.1}$$

Ideally, the device's boresight under natural tilt will point towards the satellite with no misalignment. Therefore, to obtain the ideal tilt angle, we set ∠Misalignment to zero:

$$\angle\text{Tilt} = \angle\text{Incidence} + \theta - 90°. \tag{A.2}$$

Using the boresight definition for triangular reflector from [57], we obtain $\theta = 54.74°$, providing the expression:

$$\angle \text{Tilt} = \angle \text{Incidence} - 35.26. \tag{A.3}$$

Given a specific tilt, misalignment can be determined using the expression:

$$\angle \text{Misalignment} = 35.26 + \angle \text{Tilt} - \angle \text{Incidence}. \tag{A.4}$$

Keeping this geometry in mind, Table A.1 describes the orientation of CR devices in different tracks. First, the incidence and azimuth angle of different Sentinel-1 tracks are provided which specifies the direction of the satellite, followed by the planned and actual orientation of each CR device installed on the test site. By averaging the azimuth and incidence angles of tracks in ascending and descending pass, the direction towards which the devices are to be pointed are derived and reported in the table as "Azimuth planned" and "Incidence planned" respectively. For DBF devices, the orientation in incidence is expressed in terms of the tilt angle. Using the average incidence angle towards which the devices are to be pointed, the ideal tilt to be imparted to the ascending and descending half of DBF devices is obtained using the Equation (A.3) and reported as "Tilt planned" row in the table (in place of "Incidence planned"). Note that the planned tilt is same for all DBF devices and it is the angle of the backplate from the vertical that will point these devices in the average track direction. In fact since all CR devices are planned to point toward the average track direction for each pass, these planned values are identical for each device.

On actually installing these devices on the test site, some are oriented exactly towards planned direction while for others there is an offset between the orientation planned and actual orientation achieved. For instance, the orientation of the devices in the incidence has been realized exactly towards the planned average direction ($37.5°$ for ascending and $40.66°$ for descending pass) for conventional CR devices CRAS and CRDS. An offset is introduced in each individual track from pointing the conventional CR towards the average direction. This is obtained as a difference between the actual incidence attained at the test site and the incidence direction of each track and reported as "Incidence offset". On the other hand, a small offset (imperfection in orienting the instrument) of about $0.4°$ is introduced in providing planned tilt for device DBFm's ascending and descending half while devices DBFT and DBFX are aligned perfectly in the average track direction. Net misalignment in each satellite track as a result of orienting the device in the average track direction and additional offset in realizing this average direction is given by Equation (A.4) and reported in the table as "Alignment error". Using the actual tilt realized in this expression takes into account the small imperfections in orienting the device DBFm in addition to the misalignment caused by pointing the device in the average track direction. Small imperfections are also realized in orienting all CR devices in the azimuth towards the planned average direction of $10.35°$ for ascending and $9.73°$ for descending pass. Such small imperfections in azimuth (observed $0.6°$ in CRAS, $0.32°$ in CRDS, $0.65°$ for ascending DBF and $1.27°$ for descending DBF) on the order of a few degrees can be expected in orienting devices of such bulky size. The azimuth offset introduced in each track is equivalent to the difference between the direction of actual azimuth of the device at the test site and the azimuth direction of each individual satellite track. This is reported in the table as "Frame azimuth offset". Since the realized azimuths of all DBF devices are identical, their azimuth offsets are also identical.

As part of another experiment, the orientation of device DBFm is changed on 19th August 2017. The ascending half of the device that before this epoch was pointing towards the average track direction of t088 and t161 is reoriented to point in the direction of track t161. Such a change is carried out to set the misalignment in track t161 to zero. The amount of additional tilt required to set the misalignment in track t161 to zero is obtained using:

$$\begin{aligned} \angle \text{Misalignment} &= 35.26 + \angle \text{Additional tilt} - \angle \text{t161 Incidence}, \\ \angle \text{Additional tilt} &= \angle \text{t161 Incidence} - 35.26 = 6.5. \end{aligned} \tag{A.5}$$

Therefore, a tilt of $6.5°$ is planned to be introduced to the devices DBFm in the ascending tracks on 19th August 2017. In practice an actual tilt of $6.4°$ is realized. This results in a high alignment error of $8.4°$ for track t088 while for track t161 the misalignment drops down to $-0.1°$. Increase in the misalignment for track t088 is to be expected as moving the device boresight towards track t161 means moving it farther away from track t088.

Maximum RCS is achieved when the boresight is pointed towards the satellite. Small misalignments in different tracks means that the theoretical values observed from each track will be lower than that of boresight. Using the misalignment of the boresight reported here and the relation between theoretical RCS to different angles of incidence provided in [57], the theoretical values of RCS are updated and denoted for CR and DBF devices. It must be noted here that the theoretical RCS level is much more sensitive to the misalignment in the incidence/tilt of the CR device than to the misalignment in azimuth direction although the level reported here is obtained after accounting for both misalignments. The corresponding lowering of RCS due to misalignment is reported in Figure 4.15 for device DBFm. Likewise comparison of theoretical RCS with observations for CRs and DBFs shown in Figure 4.2 across different tracks takes this effect into account, although, this change turns out to have a negligible effect on the interpretation of result in this case. As shown in this figure and Table A.1, theoretical RCS for DBFm track t161 increases to the value of maximum boresight RCS when the misalignment for track t161 is set to zero by applying additional deliberate tilt on 19th August 2017. The effect of tilt change for a DBF device in phase results is an abrupt jump in the displacement time series. Discussion on this effect is provided in more detail in Section 5.3.

The following section describes the results obtained from [58] for levelling and total station results. The results are updated with the measurements carried out on 15th August 2017 for both levelling and total station.

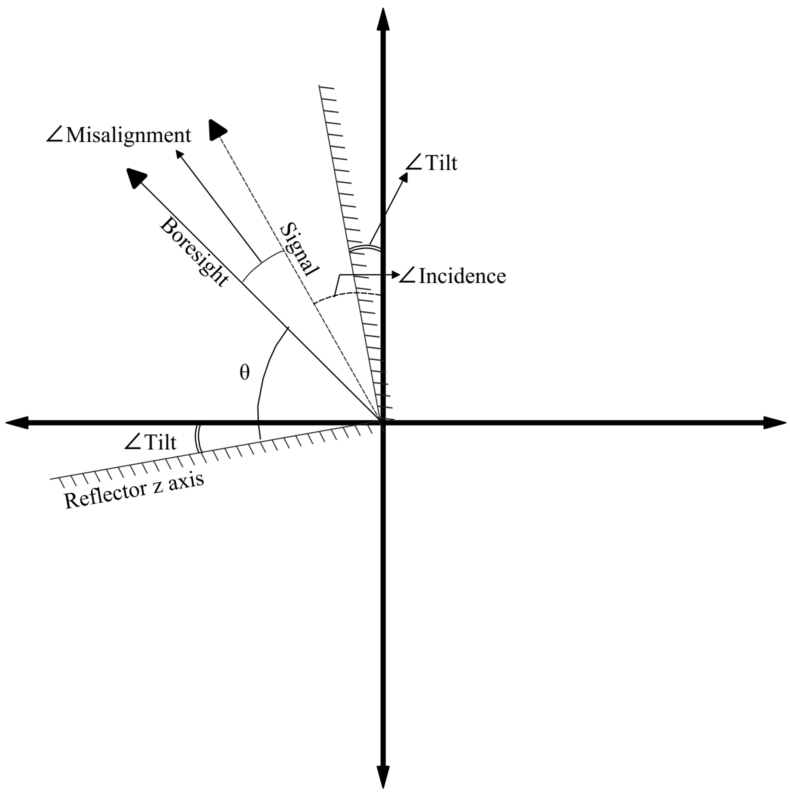

Figure A.1: Geometrical description of a typical DBF CR utilized in this study.

<table>
<tr><th rowspan="3">Sensor/ Device</th><th rowspan="3">Parameter</th><th rowspan="3">Parameter definition/ expression</th><th colspan="4">Track</th></tr>
<tr><th colspan="2">Ascending</th><th colspan="2">Descending</th></tr>
<tr><th>t088</th><th>t161</th><th>t037</th><th>t110</th></tr>
<tr><td rowspan="2">Sentinel-1</td><td>Incidence angle</td><td></td><td>33.24</td><td>41.76</td><td>44.65</td><td>36.68</td></tr>
<tr><td>Azimuth</td><td></td><td>11.16</td><td>9.54</td><td>8.92</td><td>10.54</td></tr>
<tr><td rowspan="7">CRAS/CRDS</td><td>Azimuth planned</td><td>Average azimuth direction for each asc./dsc. pass</td><td colspan="2">10.35</td><td colspan="2">9.73</td></tr>
<tr><td>Azimuth realized</td><td>Actual azimuth attained in practice</td><td colspan="2">10.95</td><td colspan="2">10.05</td></tr>
<tr><td>Frame azimuth offset</td><td>= Azimuth realized - Satellite azimuth</td><td>-0.21</td><td>1.41</td><td>1.13</td><td>-0.49</td></tr>
<tr><td>Incidence planned</td><td>Average incidence direction for each asc./dsc. pass</td><td colspan="2">37.50</td><td colspan="2">40.665</td></tr>
<tr><td>Incidence realized</td><td>Actual incidence attained in practice</td><td colspan="2">37.50</td><td colspan="2">40.66</td></tr>
<tr><td>Incidence offset</td><td>= Incidence realized - Satellite incidence</td><td>4.26</td><td>-4.26</td><td>-3.99</td><td>3.98</td></tr>
<tr><td>Theoretical RCS [dBm^2]</td><td>Lower than boresight value due to misalignment</td><td>40.42</td><td>40.40</td><td>40.43</td><td>40.45</td></tr>
<tr><td rowspan="7">DBFm (prior to Aug 19 2017)</td><td>Azimuth planned</td><td>Average azimuth direction for each asc./dsc. pass</td><td colspan="2">10.35</td><td colspan="2">9.73</td></tr>
<tr><td>Azimuth realized</td><td>Actual azimuth attained in practice</td><td colspan="2">11.00</td><td colspan="2">11.00</td></tr>
<tr><td>Frame azimuth offset</td><td>= Azimuth realized - Satellite azimuth</td><td>-0.16</td><td>1.46</td><td>2.08</td><td>0.46</td></tr>
<tr><td>Tilt planned</td><td>= Avg. satellite incidence - 35.26</td><td colspan="2">2.24</td><td colspan="2">5.405</td></tr>
<tr><td>Tilt realized</td><td>= Tilt planned +imperfection in orientation</td><td colspan="2">2.60</td><td colspan="2">5.60</td></tr>
<tr><td>Alignment error</td><td>= 35.26 + Tilt realized - Satellite incidence</td><td>4.62</td><td>-3.90</td><td>-3.79</td><td>4.18</td></tr>
<tr><td>Theoretical RCS [dBm^2]</td><td>Lower than boresight value due to misalignment</td><td>29.37</td><td>29.40</td><td>29.37</td><td>29.41</td></tr>
<tr><td rowspan="4">DBFm (since Aug 19 2017)</td><td>Additional tilt planned</td><td>= Satellite incidence t161 - 35.26</td><td colspan="2">6.50</td><td></td><td></td></tr>
<tr><td>Additional tilt realized</td><td>= Additional tilt planned + imperfection in orientation</td><td colspan="2">6.40</td><td></td><td></td></tr>
<tr><td>Alignment error</td><td>= 35.26 + Additional tilt realized - Satellite incidence</td><td>8.42</td><td>-0.10</td><td></td><td></td></tr>
<tr><td>Theoretical RCS [dBm^2]</td><td>Lower than boresight value due to misalignment</td><td>29.03</td><td>29.50</td><td></td><td></td></tr>
<tr><td rowspan="7">DBFT</td><td>Azimuth planned</td><td>Average azimuth direction for each asc./dsc. pass</td><td colspan="2">10.35</td><td colspan="2">9.73</td></tr>
<tr><td>Azimuth realized</td><td>Acutal azimuth attained in practice</td><td colspan="2">11.00</td><td colspan="2">11.00</td></tr>
<tr><td>Frame azimuth offset</td><td>= Azimuth realized - Satellite azimuth</td><td>-0.16</td><td>1.46</td><td>2.08</td><td>0.46</td></tr>
<tr><td>Tilt planned</td><td>= Avg. satellite incidence - 35.26</td><td colspan="2">2.24</td><td colspan="2">5.405</td></tr>
<tr><td>Tilt realized</td><td>= Tilt planned + imperfection in orientation</td><td colspan="2">2.20</td><td colspan="2">5.40</td></tr>
<tr><td>Alignement error</td><td>= 35.26 + Tilt realized - Satellite incidence</td><td>4.22</td><td>-4.30</td><td>-3.99</td><td>3.98</td></tr>
<tr><td>Theoretical RCS [dBm^2]</td><td>Lower than boresight value due to misalignment</td><td>29.39</td><td>29.38</td><td>29.39</td><td>29.40</td></tr>
<tr><td rowspan="7">DBFX</td><td>Azimuth planned</td><td>Average azimuth direction for each asc./dsc. pass</td><td colspan="2">10.35</td><td colspan="2">9.73</td></tr>
<tr><td>Azimuth realized</td><td>Actual azimuth attained in practice</td><td colspan="2">11.00</td><td colspan="2">11.00</td></tr>
<tr><td>Frame azimuth offset</td><td>= Azimuth realized - Satellite azimuth</td><td>-0.16</td><td>1.46</td><td>2.08</td><td>0.46</td></tr>
<tr><td>Tilt planned</td><td>= Avg. satellite incidence - 35.26</td><td colspan="2">2.24</td><td colspan="2">5.405</td></tr>
<tr><td>Tilt realized</td><td>= Tilt planned + imperfection in orientation</td><td colspan="2">2.20</td><td colspan="2">5.40</td></tr>
<tr><td>Alignment error</td><td>= 35.26 + Tilt realized - Satellite incidence</td><td>4.22</td><td>-4.30</td><td>-3.99</td><td>3.98</td></tr>
<tr><td>Theoretical RCS [dBm^2]</td><td>Lower than boresight value due to misalignment</td><td>36.48</td><td>36.32</td><td>36.49</td><td>36.36</td></tr>
</table>

Table A.1: Description of the orientation of the CR device and the satellite sensor at the test site. The table describes the planned orientation of the device, direction attained in practice, the misalignment caused due to the offset between the sensor and the device in incidence, azimuth and tilt. The change in theoretical RCS due to these offsets are reported using the alignment errors in the relation provided by [57]. The azimuth angles for the ascending tracks are reported clockwise from East while for descending tracks the values represents the angles measured anticlockwise from West.

A.2. Local Survey results

This section shows the results from these levelling campaigns carried out between December 2016 and 15th August 2017. Table A.2 shows the height measurements of the markers obtained as a difference with the reference point. In order to analyze the evolution of height of these markers through time, table A.3 provides these measurements relative to the first epoch. The results include the measurements carried out over East and West markers for MUTE pads. While table A.4 and table A.5 reports the height difference and displacement values computed as an average between the east and west markers for the MUTEs to monitor the subsidence of the pad. Table A.6 reports the result obtained from the total station campaign carried out between December 2016 and November 2017. This table reports the displacement measured in three directions (East-West, North-South and Up-Down). The West, South and Up directions are considered positive.

MARKER	21-09-2016	27-12-2016	07-03-2017	11-04-2017	14-05-2017	15-08-2017
CRDS			295.48	295.49	295.57	295.73
WASS06	-2.01	-2.02	-1.99	-2.00	-2.09	-1.93
CRAS			273.67	273.89	273.67	273.84
WASS05	2.01	2.02	1.99	2.00	2.09	1.93
MUTE2E		5.72	5.31	5.07	5.14	4.75
MUTE2W		6.53	6.57	6.43	6.53	6.23
MUTE1E		-26.48	-26.35	-26.48	-26.42	-26.42
MUTE1W		-25.83	-25.77	-25.96	-25.86	-25.94

Table A.2: Height of the levelling markers measured relative to the reference (mean of levelling markers on WASS04 and WASS05).

MARKER	21-09-2016	27-12-2016	07-03-2017	11-04-2017	14-05-2017	15-08-2017
CRDS			0.00	0.01	0.09	0.25
WASS06	0.00	-0.01	0.02	0.02	-0.08	0.08
CRAS			0.00	0.22	0.00	0.17
WASS05	0.00	0.01	-0.02	-0.02	0.08	-0.08
MUTE2E		0.00	-0.41	-0.65	-0.58	-0.97
MUTE2W		0.00	0.04	-0.10	0.01	-0.29
MUTE1E		0.00	0.13	0.00	0.06	0.06
MUTE1W		0.00	0.06	-0.13	-0.04	-0.11

Table A.3: Evolution of height through time measured as double-difference of the height differences between levelling markers with respect to the mean of levelling markers on WASS04-WASS05 reference expressed relative to the first epoch.

MARKER	21-09-2016	27-12-2016	07-03-2017	11-04-2017	14-05-2017	15-08-2017
MUTE-2		6.12	5.94	5.75	5.84	5.49
MUTE-1		-26.16	-26.06	-26.22	-26.14	-26.18
CRDS			295.48	295.49	295.57	295.73
CRAS			273.67	273.89	273.67	273.84

Table A.4: Height of the levelling markers measured relative to the reference. An average of the east and west markers is taken to be the measurement point for the MUTEs.

MARKER	21-09-2016	27-12-2016	07-03-2017	11-04-2017	14-05-2017	15-08-2017
MUTE-2		0.00	-0.18	-0.38	-0.29	-0.63
MUTE-1		0.00	0.10	-0.07	0.01	-0.03
CRDS			0.00	0.01	0.09	0.25
CRAS			0.00	0.22	0.00	0.17

Table A.5: Evolution of height through time measured as double-difference of the height differences between levelling markers with respect to the reference expressed relative to the first epoch. An average of the east and west markers is taken to be the measurement point for the MUTEs.

MARKERS	27-12-2016	06-03-2017	07-03-2017	11-04-2017	14-05-2017	15-08-2017
MUTE-1 E-W[mm]	0.00	0.35	0.25	0.30	0.45	0.30
MUTE-2 E-W[mm]	0.00	-0.55	-0.60	-0.40	-0.10	-0.52
MUTE-1 N-S[mm]	0.00	0.95	0.60	0.60	1.30	0.20
MUTE-2 N-S[mm]	0.00	-0.15	-0.10	-0.35	-0.95	-0.27
MUTE-1 U-D[mm]	0.00	0.75	7.80	7.80	7.75	8.15
MUTE-2 U-D[mm]	0.00	0.85	0.95	0.90	1.30	1.12
MUTE-1 Corr. U-D[mm]	0.00	0.75	0.80	0.80	0.75	1.15
MUTE-2 Corr. U-D[mm]	0.00	0.85	0.95	0.90	1.30	1.12

Table A.6: Movements in E-W, N-S and U-D direction with respect to the basepole and with respect to the first epoch. The mean of east and west markers are reported.

B

Appendix B

As mentioned in Section 4.4.2, the representative values of signal and clutter needed for a-priori phase standard deviation approximation are obtained using MLE. This appendix briefly describes the simulation on the basis of which this choice is made. It involves comparison of expectation values obtained using different approaches for simulated signal and noise [63].

B.1. Simulation

The expectation values of signal from observation time series reported in this study can be derived in the following ways. They can be obtained by computing the empirical mean and standard deviation for samples. The amplitude values exhibit Rician distribution and the population mean and standard deviation can be obtained for such a distribution using the expressions provided in [67]. It is also possible to estimate signal and clutter directly from amplitudes using MLE estimates. The expectation values obtained from these approaches can be tested using simulation by comparing them with true simulated signal.

Such a true signal is defined as a time series of magnitude ranging from 0 to 10. An amplitude time series of a thousand values is generated from this signal and a random circular Gaussian noise is introduced by setting different noise standard deviation values in each simulation. This amplitude is expressed as intensity (square of amplitude) and power levels (intensity expressed in decibel scale). Mean and standard deviations are obtained for amplitude, intensity and power levels using the approaches described above.

Here the comparison of statistics from these approaches with true signal and clutter is shown in Figure B.1 for different signal magnitude on the primary x axis and for different SCR on the secondary x axis. Figure B.2a provides this comparison for amplitude values while Figure B.2b provides mean comparison for power levels. The comparison between the expected values of mean and true signal is expressed as difference between the two. Therefore, the closer the result is to zero, the more accurately it approximates the estimate of its true value. These differences are shown in the figure using solid line for sample estimate, dash line for approximated population estimate and the ring line for mean signal estimated using MLE. The standard deviation are reported directly and they follow the same convention of line styles.

Both mean and standard deviation depicted in Figure B.2a for sample and population estimate differ from the true signal and clutter. For large signal magnitude/SCR, estimates for different approaches converge closer to true values. This demonstrates that the sample mean and standard deviation are biased estimators of signal/clutter and MLE estimates are better suited for the approximation of these values. The estimation of a-priori phase variance is therefore based on the signal and clutter representative value obtained using MLE. For power levels on the other hand, sample mean estimate converges quickly to the true signal magnitude. Therefore, when amplitude is converted to power levels, sample mean turns to be a good estimator of the signal. In this study, the amplitude observations are expressed as RCS time series. RCS is a parameter similar to Power level that expresses the square of amplitude in decibel scale after applying calibration. Thus sample mean of RCS is expected to be close to the estimate obtained using MLE and the true signal.

(a) (b)

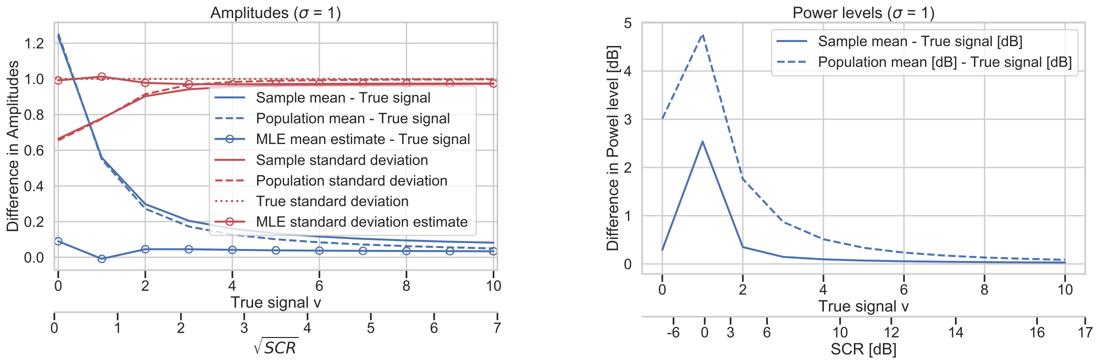

Figure B.1: Comparison of mean and standard deviation statistics derived for sample, for population and as estimated using MLE with true mean and standard deviation. These statistics are provided for (a)simulated amplitudes and (b)simulated power levels (square of amplitudes expressed in decibel scale) when the noise level (σ) is set to one. The mean statistics, shown here with blue lines, are expressed as their difference with true signal. The standard deviations are represented by red lines and compared against the true noise level. Sub-figure(a) shows that the sample and approximated population estimate differs from true mean and standard deviation except at high signal/SCR magnitudes. Sub-figure(b) shows that for power levels, however, sample mean acts as a good estimator of true signal except for very low SCR.

C

Appendix C

This appendix provides an overview for each device installed on the test site except for ECR (prototypes are experimental in nature) in a tabular format. The table covers device description, its setup on the test site and its performance characteristics such as stability and anomalies witnessed in its amplitude and phase response.

C.1. Device Overview

The first three columns of Table C.1 describes the nature of device along with its image. The fourth and fifth column covers its operational period on the test site (from Chapter 3) while the ”Alignment” column describes the realized orientation at the site, misalignment in orientation and theoretical RCS level (from Appendix A). The next two columns describes the performance characteristic of each device in terms of whether or not it shows the amplitude and phase stability (Chapters 4 and 5). A device is classified as RCS and phase stable if the slope of the model fit to the corresponding time series is within ± 0.5 dBm^2/quarter and ± 0.5 mm/quarter respectively. The next column describes the changes introduced deliberately to certain devices at the test site. The anomalies in amplitude and phase response as detected from analysis of SAR images are reported in the column ”Anomalies”. The final column reports the external factors found to be influencing the performance of each device which explains the corresponding anomalies in amplitude and phase results (Chapters 4 and 5).

Some of these anomalies can potentially be prevented in the future experiments. For instance, the deliberate movement that is imparted to devices MUTE-1 and DBFm as vertical movement and deliberate tilt respectively that causes an abrupt jump anomaly in the amplitude and phase results of these devices. This deliberate change is part of the experiment to determine the error in the SAR estimate. Likewise the gradually increasing westward motion detected for MUTE-1 and DBFT that share the same location as a result of their concrete pad tilting westwards can be averted by a better foundation design (a similar eastward tilt in the foundation of device MUTE-2 results in an eastward motion for this device as shown in the table). Lack of structural stiffness in DBFm that leads to high uncertainty in RCS and phase results is rectified by modifying the structural design and including additional elements that affords more stiffness in the subsequent design cycle for devices DBFT and DBFX [9] which are observed to be amplitude and phase stable.

In addition to devices DBFT and DBFX, corner reflectors CRAS and CRDS are also observed to be stable. But the phase and amplitude results of these devices do exhibit outliers corresponding to epochs of heavy precipitation that causes accumulation of excess snow and rain in the apex of the CR. Therefore the performance of these devices is susceptible to heavy precipitation. There is a significant trend and step in the amplitude and phase result of the first generation MUTE RT which is argued to have resulted from either device malfunction or temperature influence on performance. Once this trend and step is modelled and removed from the results, the InSAR measurements are in agreement with the levelling observations within error bounds and the phase results become stable.

Devices	Photo	Device type	Start date	End date	Alignment: Parameter	Value in tracks: t088		t161	t037		t110	RCS Stability	Phase Stability	Deliberate changes	Anomalies	Performance sensitive factors
CRAS, CRDS		Conventional square based CRs of leg length 1.425 m	4 Feb 2017	-	Incidence [deg] Incidence offset [deg] Azimuth [deg] Azimuth offset [deg] Theoretical RCS [dBm^2]	 4.26 -0.21 40.42	37.50 10.95	 -4.26 1.41 40.39	 -3.99 1.13 40.43	40.66 10.05	 3.98 -0.49 40.44	✓	✓	-	Outliers	Snow/rain
MUTE-1		First-generation MUTE RT device installed over a basepole of height 1.07 ± 0.002 m	25 Oct 2016	4 Sep 2017	-		-			-		×	×	Vertical movement: 7 ± 0.05 mm on 7th March 2017	a) Abrupt jump in phase results b) Trend and step in RCS and phase results c) Linearly increasing westward movement	a) Due to deliberate movement b) Malfunction/ temperature dependence c) Concrete pad tilts towards west
MUTE-2		Second-generation MUTE RT device installed over a basepole of height 1.07 ± 0.002 m	25 Oct 2016	4 Sep 2017	-		-			-		✓	✓	-	a) Linearly increasing eastward movement	a) Concrete pad tilts towards east b) Temperature dependence
DBFm		Double backflip CR mockup prototype with triangular reflection surfaces of leg length 0.9 m	3 Aug 2017	4 Nov 2017	Incidence [deg] Azimuth [deg] *(prior to Aug 19 2017)* Tilt [deg] Alignment error [deg] Theoretical RCS [dBm^2] *(since Aug 19 2017)* Additional tilt [deg] Alignment error [deg] Theoretical RCS [dBm^2]	 4.62 29.37 8.42 29.03	37.50 11.00 2.6 6.40	 -3.90 29.41 -0.1 29.51	 -3.79 29.39 - -	40.67 11.00 5.6 -	 4.18 29.41 - -	-	×	Additional tilt in ascending half: 6.4° on 19th August 2017	a) Abrupt jump in RCS and phase results b) Trend in phase results from certain tracks; Relatively higher uncertainty in amplitude and phase results	a) Due to deliberate tilt b) Vibrations from lack of adequate stiffness
DBFT		Double backflip CR of higher production quality with triangular reflection surfaces of leg length 0.9 m	5 Nov 2017	-	Incidence [deg] Azimuth [deg] Tilt [deg] Alignment error [deg] Theoretical RCS [dBm^2]	 4.22 29.38	37.50 11.00 2.20	 -4.30 29.38	 -3.99 29.40	40.67 11.00 5.40	 3.98 29.40	✓	✓	-	a) Outliers b) Linearly increasing westward movement	a) Snow b) Concrete pad tilts towards west
DBFX		Double backflip CR of higher production quality (with additional polycarbonate plates) that uses 0.9 m triangular reflection surfaces with truncated tips	5 Nov 2017	-	Incidence [deg] Azimuth [deg] Tilt [deg] Alignment error [deg] Theoretical RCS [dBm^2]	 4.22 36.48	37.50 11.00 2.20	 -4.30 36.32	 -3.99 36.49	40.67 11.00 5.40	 3.98 36.36	✓	✓	-	Outliers	Snow

Table C.1: Overview of all the devices operational at the test site (except the ECR family of devices) describing the type of device employed, their period of operation, their orientation and their performance characteristics. The alignment reported in this table is the orientation realized at the site (see Appendix A for a detailed description of the parameters), the offset in orientation for each satellite track and theoretical RCS level under such orientation. Alignment of device DBFm is reported before and after the additional tilt is introduced. Such deliberate changes imparted to the devices are reported in a separate column. Devices are classified as RCS or phase stable if the slope of the model fit to the corresponding time series is within ± 0.5 dBm^2/quarter and ± 0.5 mm/quarter respectively. The anomalies in RCS and phase results of the device is reported along with the corresponding influence of external factors responsible for them in the final two columns.

References

[1] H. Lyons, *Ancient surveying instruments,* The Geographical Journal **69**, 132 (1927).

[2] R. F. Hanssen, *Subsidence monitoring using contiguous and ps-insar: Quality assessment based on precision and reliability,* Proc. 11th FIG Sym. Def. Measur., Santorini, Grecia (2003).

[3] H. A. Zebker and R. M. Goldstein, *Topographic mapping from interferometric synthetic aperture radar observations,* Journal of Geophysical Research: Solid Earth **91**, 4993 (1986).

[4] D. Massonnet and F. Adragna, *A full-scale validation of radar interferometry with ers-1: the landers earthquake,* Earth Observation Quarterly **41**, 1 (1993).

[5] H. A. Zebker, P. A. Rosen, R. M. Goldstein, A. Gabriel, and C. L. Werner, *On the derivation of coseismic displacement fields using differential radar interferometry: The landers earthquake,* Journal of Geophysical Research: Solid Earth **99**, 19617 (1994).

[6] A. Ferretti, C. Prati, and F. Rocca, *Permanent scatterers in sar interferometry,* IEEE Transactions on geoscience and remote sensing **39**, 8 (2001).

[7] P. S. Mahapatra, *Geodetic network design for insar: application to ground deformation monitoring,* (2015).

[8] R. F. Hanssen, *A radar retroreflector device and a method of preparing a radar retroreflector device,* (2017), patent WO 2018/236215 Al.

[9] J. Kamphuis, *Co-locating geodetic reference points: On the design and performance of an integrated geodetic reference station,* (2019).

[10] R. F. Hanssen, *Radar interferometry: data interpretation and error analysis*, Vol. 2 (Springer Science Business Media, 2001).

[11] R. K. Raney, H. Runge, R. Bamler, I. G. Cumming, and F. H. Wong, *Precision sar processing using chirp scaling,* IEEE Transactions on geoscience and remote sensing **32**, 786 (1994).

[12] C. Wu, *A digital approach to produce imagery from sar data,* the AIAA Syst. Design Driven by Sensor (1976).

[13] C. Cafforio, C. Prati, and F. Rocca, *Sar data focusing using seismic migration techniques,* IEEE transactions on aerospace and electronic systems **27**, 194 (1991).

[14] R. Bamler, *A comparison of range-doppler and wavenumber domain sar focusing algorithms,* IEEE Transactions on Geoscience and Remote Sensing **30**, 706 (1992).

[15] A. L. Gray, P. W. Vachon, C. E. Livingstone, and T. I. Lukowski, *Synthetic aperture radar calibration using reference reflectors,* IEEE Transactions on Geoscience and Remote Sensing **28**, 374 (1990).

[16] A. Freeman, *Sar calibration: An overview,* IEEE Transactions on Geoscience and Remote Sensing **30**, 1107 (1992).

[17] F. J. Van Leijen, *Persistent scatterer interferometry based on geodetic estimation theory,* (2014).

[18] S. Samiei Esfahany, *Exploitation of distributed scatterers in synthetic aperture radar interferometry,* (2017).

[19] J. Foster, B. Brooks, T. Cherubini, C. Shacat, S. Businger, and C. Werner, *Mitigating atmospheric noise for insar using a high resolution weather model,* Geophysical Research Letters **33** (2006).

[20] X.-l. Ding, Z.-w. Li, J.-j. Zhu, G.-c. Feng, and J.-p. Long, *Atmospheric effects on insar measurements and their mitigation,* Sensors **8**, 5426 (2008).

[21] S. Liu, *Satellite radar interferometry: estimation of atmospheric delay*, Thesis (2012).

[22] F. Gatelli, A. M. Guamieri, F. Parizzi, P. Pasquali, C. Prati, and F. Rocca, *The wavenumber shift in sar interferometry,* IEEE Transactions on Geoscience and Remote Sensing **32**, 855 (1994).

[23] L. G. Brown, *A survey of image registration techniques,* ACM computing surveys (CSUR) **24**, 325 (1992).

[24] J. Samson, *Coregistration in SAR interferometry*, Thesis (1996).

[25] P. Marinkovic and R. Hanssen, *Advanced insar coregistration using point clusters,* in *Geoscience and Remote Sensing Symposium, 2004. IGARSS'04. Proceedings. 2004 IEEE International*, Vol. 1 (IEEE) pp. 489–492.

[26] L. T. Swart, *Spectral filtering and oversampling for radar interferometry,* (2000).

[27] O. Hellwich and H. Ebner, *Geocoding sar interferograms by least squares adjustment,* ISPRS Journal of Photogrammetry and Remote Sensing **55**, 277 (2000).

[28] D. Geudtner and M. Schwäbisch, *An algorithm for precise reconstruction of insar imaging geometry: Application to "flat earth" phase removal, phase-to-height conversion, and geocoding of insar-derived dems,",* in *Proc. EUSAR*, Vol. 96, pp. 249–252.

[29] H. Baehr, *Orbital effects in spaceborne synthetic aperture radar interferometry* (KIT Scientific Publishing, 2013).

[30] J.-S. Lee, K. W. Hoppel, S. A. Mango, and A. R. Miller, *Intensity and phase statistics of multilook polarimetric and interferometric sar imagery,* IEEE Transactions on Geoscience and Remote Sensing **32**, 1017 (1994).

[31] R. M. Goldstein, H. A. Zebker, and C. L. Werner, *Satellite radar interferometry: Two□dimensional phase unwrapping,* Radio science **23**, 713 (1988).

[32] B. M. Kampes, *Displacement parameter estimation using permanent scatterer interferometry,* (2005).

[33] P. Marinkovic, G. Ketelaar, F. van Leijen, and R. Hanssen, *Insar quality control: Analysis of five years of corner reflector time series,* in *Proceedings of Fringe 2007 Workshop (ESA SP-649), Frascati, Italy*, Vol. 26, p. 30.

[34] A. H.-M. Ng, L. Ge, X. Li, and K. Zhang, *Monitoring ground deformation in beijing, china with persistent scatterer sar interferometry,* Journal of Geodesy **86**, 375 (2012).

[35] G. Liu, S. M. Buckley, X. Ding, Q. Chen, and X. Luo, *Estimating spatiotemporal ground deformation with improved persistent-scatterer radar interferometry *,* IEEE Transactions on Geoscience and Remote Sensing **47**, 3209 (2009).

[36] J. J. Sousa, A. J. Hooper, R. F. Hanssen, L. C. Bastos, and A. M. Ruiz, *Persistent scatterer insar: A comparison of methodologies based on a model of temporal deformation vs. spatial correlation selection criteria,* Remote Sensing of Environment **115**, 2652 (2011).

[37] J. Hu, Z. Li, X. Ding, J. Zhu, L. Zhang, and Q. Sun, *Resolving three-dimensional surface displacements from insar measurements: A review,* Earth-Science Reviews **133**, 1 (2014).

[38] M. Riedmann and M. Haynes, *Developments in synthetic aperture radar interferometry for monitoring geohazards,* Geological Society, London, Special Publications **283**, 45 (2007).

[39] Y. Xia, H. Kaufmann, and X. Guo, *Differential sar interferometry using corner reflectors,* in *Geoscience and Remote Sensing Symposium, 2002. IGARSS'02. 2002 IEEE International*, Vol. 2 (IEEE) pp. 1243–1246.

[40] A. Ferretti, G. Savio, R. Barzaghi, A. Borghi, S. Musazzi, F. Novali, C. Prati, and F. Rocca, *Submillimeter accuracy of insar time series: Experimental validation,* IEEE Transactions on Geoscience and Remote Sensing **45**, 1142 (2007).

[41] F. Bovenga, R. Nutricato, A. Refice, and J. Wasowski, *Application of multi-temporal differential interferometry to slope instability detection in urban/peri-urban areas,* Engineering Geology **88**, 218 (2006).

[42] S. Gernhardt, N. Adam, M. Eineder, and R. Bamler, *Potential of very high resolution sar for persistent scatterer interferometry in urban areas,* Annals of GIS **16**, 103 (2010).

[43] D. Perissin and T. Wang, *Time-series insar applications over urban areas in china,* IEEE Journal of Selected Topics in Applied Earth Observations and Remote Sensing **4**, 92 (2011).

[44] P. S. Mahapatra, S. Samiei-Esfahany, H. van der Marel, and R. F. Hanssen, *On the use of transponders as coherent radar targets for sar interferometry,* IEEE Transactions on Geoscience and Remote Sensing **52**, 1869 (2014).

[45] M. C. Garthwaite, *On the design of radar corner reflectors for deformation monitoring in multi-frequency insar,* Remote Sensing **9**, 648 (2017).

[46] G. Savio, A. Ferretti, F. Novali, S. Musazzi, C. Prati, and F. Rocca, *Psinsar validation by means of a blind experiment using dihedral reflectors,* in *FRINGE 2005 workshop*, Vol. 610.

[47] X. Ye, H. Kaufmann, and X. Guo, *Landslide monitoring in the three gorges area using d-insar and corner reflectors,* Photogrammetric Engineering Remote Sensing **70**, 1167 (2004).

[48] C. R. Froese, V. Poncos, R. Skirrow, M. Mansour, and D. Martin, *Characterizing complex deep seated landslide deformation using corner reflector insar (cr-insar): Little smoky landslide, alberta,* in *Proc. 4th Can. Conf. Geohazards*, pp. 1–4.

[49] M. Garthwaite, S. Nancarrow, A. Hislop, M. Thankappan, J. Dawson, and S. Lawrie, *Design of radar corner reflectors for the australian geophysical observing system,* Geoscience Australia **3** (2015).

[50] D. Hounam, H. Zwick, and B. Rabus, *A permanent response sar transponder for monitoring ground targets and features,* in *Synthetic Aperture Radar (EUSAR), 2008 7th European Conference on* (VDE) pp. 1–4.

[51] D. J. Park, K. W. Yeom, S. I. Ahn, and H. S. Lim, *Validation of an active transponder for kompsat-5 sar image calibration,* Advances in Space Research **54**, 1552 (2014).

[52] J. Hole, R. Holley, G. Giunta, G. De Lorenzo, and A. M. Thomas, *Insar assessment of pipeline stability using compact active transponders,* in *Proceedings of FRINGE2011, 8th International Workshop on "Advances in the Science and Applications of SAR Interferometry ". European Space Agency, Frascati, Italy*, Vol. 201, pp. 19–23.

[53] P. Mahapatra, H. van der Marel, F. van Leijen, S. Samiei-Esfahany, R. Klees, and R. Hanssen, *Insar datum connection using gnss-augmented radar transponders,* Journal of Geodesy **92**, 21 (2018).

[54] L. P. Louwe Kooijmans, *An early/middle bronze age multiple burial at wassenaar,* (1993).

[55] M. Van der Meulen, F. de Lang, and D. Maljers, *Cw dubelaar en we westerhoff,* Grondstoffen en delfstoffen bij naam. Delft, Dienst Weg-en Waterbouw (2003).

[56] T. E. S. Agency, *Satellite constellation,* .

[57] J. Groot, *Cross section computation of trihedral corner reflectors with the geometrical optics approximation,* European Transactions on Telecommunications **3**, 637 (1992).

[58] H. van der Marel, F. J. Van Leijen, and R. Hanssen, *Multiple Frequency Radar Compact Transponder (MUTE)*, Report (TU Delft, 2017).

[59] G. Ketelaar, P. Marinkovic, and R. Hanssen, *Validation of point scatterer phase statistics in multi-pass insar,* in *Envisat ERS Symposium*, Vol. 572.

[60] N. Adam, B. Kampes, and M. Eineder, *Development of a scientific permanent scatterer system: Modifications for mixed ers/envisat time series,* in *Envisat ERS Symposium*, Vol. 572.

[61] M. I. Skolnik, *Radar handbook,* (1970).

[62] K. El-Darymli, P. McGuire, E. Gill, D. Power, and C. Moloney, *Understanding the significance of radiometric calibration for synthetic aperture radar imagery,* in *Electrical and Computer Engineering (CCECE), 2014 IEEE 27th Canadian Conference on* (IEEE) pp. 1–6.

[63] H. van der Marel, *Personal communication,* (2017).

[64] ESA, *S-1A TOPS Radiometric Calibration Refinement1.*, Report Technical Note ESA-EOPG-CSCOP-TN-0012. (ESA, 2015).

[65] K. Schmidt, N. T. Ramon, M. J. I. J. o. M. Schwerdt, and W. Technologies, *Radiometric accuracy and stability of sentinel-1a determined using point targets,* **10**, 538 (2018).

[66] M. Schwerdt, K. Schmidt, N. Tous Ramon, P. Klenk, N. Yague-Martinez, P. Prats-Iraola, M. Zink, and D. J. R. S. Geudtner, *Independent system calibration of sentinel-1b,* **9**, 511 (2017).

[67] A. Foi, *Noise estimation and removal in mr imaging: The variance-stabilization approach,* in *2011 IEEE International symposium on biomedical imaging: from nano to macro* (IEEE) pp. 1809–1814.

[68] T. Delft, *Integrated geodetic reference stations (igrs) - groningen,* (2020).

[69] T. Fuhrmann and M. C. J. R. S. Garthwaite, *Resolving three-dimensional surface motion with insar: Constraints from multi-geometry data fusion,* **11**, 241 (2019).

[70] T. J. Wright, B. E. Parsons, and Z. J. G. R. L. Lu, *Toward mapping surface deformation in three dimensions using insar,* **31** (2004).

[71] M. Haghshenas Haghighi and G. u. L. Motagh, Mahdi für Geodäsie, *Sentinel-1 insar over germany: Large-scale interferometry, atmospheric effects, and ground deformation mapping,* **2017**, 245 (2017).